

UNIVERSITY OF RIJEKA  
FACULTY OF ENGINEERING

Andro Rak

**EXPERIMENTAL AND NUMERICAL  
ANALYSIS OF AERODYNAMICS AND  
AEROACOUSTICS OF PRIMARY AND  
SERRATED EDGE WING**

DOCTORAL DISSERTATION

Rijeka, 2025





UNIVERSITY OF RIJEKA  
FACULTY OF ENGINEERING

Andro Rak

**EXPERIMENTAL AND NUMERICAL  
ANALYSIS OF AERODYNAMICS AND  
AEROACOUSTICS OF PRIMARY AND  
SERRATED EDGE WING**

DOCTORAL DISSERTATION

Supervisor: Prof. Lado Kranjčević, PhD

Rijeka, 2025



SVEUČILIŠTE U RIJECI  
TEHNIČKI FAKULTET

Andro Rak

**EKSPERIMENTALNA I NUMERIČKA  
ANALIZA AERODINAMIKE I  
AEROAKUSTIKE PRIMARNOGA KRILA  
I KRILA NAZUBLJENA PRATEĆEGA  
RUBA**

DOKTORSKI RAD

Mentor: prof. dr. sc. Lado Kranjčević

Rijeka, 2025.



Doctoral dissertation supervisor: Prof. Lado Kranjčević, PhD

The doctoral dissertation was defended on \_\_\_\_\_ at the University of Rijeka, Faculty of Engineering, Croatia, in front of the following Evaluation Committee:

1. Prof. Siniša Družeta, PhD, University of Rijeka, Faculty of Engineering
2. Assoc. Prof. Stefan Ivić, PhD, University of Rijeka, Faculty of Engineering
3. Prof. Hrvoje Kozmar, PhD, University of Zagreb, Faculty of Mechanical Engineering and Naval Architecture



# ACKNOWLEDGEMENTS

I would like to express my sincere gratitude to my supervisor, Prof. Kranjčević, who provided me with all the necessary tools for research, as well as the belief and freedom to pursue it as I wished. I am also grateful to all my colleagues from the department for sharing ideas, problems, and coffee during those exhausting moments we went through together. Additionally, I would like to thank my colleagues from the University of Southampton, who made my time there productive and provided helpful suggestions.

I would like to thank my family and dearest Bruna, whose constant encouragement and belief in my abilities made the completion of this dissertation possible. Special appreciation goes to my parents, who have unselfishly supported me from my first steps in education to the present day, and to my grandfather, whose unwavering encouragement to pursue a PhD motivated me during the most challenging times.

# ABSTRACT

This dissertation presents a comprehensive computational investigation of primary and bio-inspired serrated trailing edge airfoils, employing multiple methodological and numerical approaches within computational fluid dynamics to evaluate their aerodynamic and aeroacoustic characteristics.

The experimental validation component conducted in a wind tunnel facility expands the NACA 0012 dataset for moderate Reynolds number flows ( $Re = 191,000$ ) and low Mach numbers ( $Ma = 0.057$ ), across angles of attack ranging from  $2^\circ$  to  $8^\circ$ . A novel hybrid Lattice Boltzmann Method (LBM) - Large Eddy Simulation (LES) approach, incorporating one-way coupling with the Generalized Wall Function, D3Q27 velocity set, and a modern cumulant collision operator, validates computational predictions against experimental measurements with pressure coefficient deviations below 0.076 based on RMSE statistics.

The research then focuses on the implementation of robust LES on an airfoil's serrations, which were performed at various Reynolds numbers from 100,000 to half a million and a highly incompressible Mach number of 0.25 at a  $5^\circ$  angle of attack. At a Reynolds number of 250,000, a detailed analysis revealed that adding serrations is advantageous for enhancing the airfoil's boundary layer stability and reducing noise with only a minor compromise in aerodynamic efficiency that improves over time and at higher Reynolds numbers. Analysis of the aerodynamic and aeroacoustic influences on the flow reveals that trailing edge sound waves trigger the breakdown of the laminar separation bubble on the primary trailing edge airfoil. On the other hand, the serrations promote an earlier transition of the turbulent boundary layer without forming a laminar separation bubble. Across higher Reynolds numbers, the benefits of the serrated trailing edge persisted, with earlier noise generation and boundary layer transition enhancing the non-dimensional force in the  $y$ -direction. Overall, adding serrations enhances boundary layer stability and reduces trailing edge noise during both the acceleration and post-acceleration phases. Likewise, it achieves consistent noise reductions of 3-8 dB across all examined Reynolds numbers while simultaneously maintaining acceptable aerodynamic performance.



Finally, an advanced two-way coupling approach is implemented, incorporating the Generalized Law of the Wall, to enable high-fidelity simulations that capture specific physical phenomena. The finite-span wing analysis reveals the wing tip vortex's influence on boundary layer transition, extending from the wing tip and affecting overall flow development patterns, in addition to shear layer instability and boundary layer transition mechanisms.

The integrated methodological framework successfully elucidates detailed aerodynamic and aeroacoustic interactions for both infinite and finite-span configurations with triangular and sinusoidal serrations across acceleration and post-acceleration phases, demonstrating consistent benefits of serration implementation through noise reduction and stability improvements for moderate Reynolds number applications.

**Keywords:** Lattice Boltzmann Method, Serrated Trailing Edge, Large Eddy Simulation, Computational Fluid Dynamics, Aerodynamics, Aeroacoustics, Boundary Layer Transition, Trailing Edge Noise

# PROŠIRENI SAŽETAK

Ova disertacija predstavlja sveobuhvatno računalno istraživanje primarnih i bioinspiriranih nazubljenih aeroprofila s pratećim rubom, koristeći više metodoloških i numeričkih pristupa unutar računalne dinamike fluida za procjenu njihovih aerodinamičkih i aeroakustičkih karakteristika.

Eksperimentalna komponenta validacije provedena u zračnom tunelu proširuje skup podataka NACA 0012 za umjerene tokove Reynoldsovog broja ( $Re = 191,000$ ) i niske Machove brojeve ( $Ma = 0.057$ ), preko upadnih kutova u rasponu od  $2^\circ$  do  $8^\circ$ . Novi hibridni pristup Lattice Boltzmannove metode (LBM) - simulacije velikih vrtloga (LES), koji uključuje jednosmjerno spajanje s generaliziranom zidnom funkcijom, skupom brzina D3Q27 i modernim operatorom kumulativnog sudara, potvrđuje računalna predviđanja u odnosu na eksperimentalna mjerenja s odstupanjima koeficijenta tlaka ispod 0.076 na temelju RMSE statistike.

Istraživanje se zatim usredotočuje na implementaciju robusnog LES-a na nazubljenjima krila, što je provedeno pri različitim Reynoldsovim brojevima od 100,000 do pola milijuna i visoko nestlačivom Machovom broju od 0.25 pod upadnim kutom od  $5^\circ$ . Pri Reynoldsovom broju od 250,000, detaljna analiza otkriva da je dodavanje nazubljenja korisno za poboljšanje stabilnosti graničnog sloja krila i smanjenje buke uz samo manji kompromis u aerodinamičkoj učinkovitosti koja se poboljšava s vremenom i pri višim Reynoldsovim brojevima. Analiza aerodinamičkih i aeroakustičkih utjecaja na strujanje otkriva da zvučni valovi sa pratećeg ruba pokreću raspad laminarnog separacijskog mjehura na krilu s primarnim pratećim rubom. S druge strane, nazubljenja potiču raniji prijelaz ka turbulentnom graničnom sloju bez stvaranja laminarnog separacijskog mjehura. Pri višim Reynoldsovim brojevima, prednosti nazubljenog pratećeg ruba su se zadržale, s ranijim generiranjem buke i prijelazom graničnog sloja koji pojačavaju bezdimenzionalnu silu u y-smjeru. Sveukupno, dodavanje nazubljenja poboljšava stabilnost graničnog sloja i smanjuje buku stražnjeg ruba tijekom faze ubrzanja i nakon ubrzanja. Isto tako, postiže konzistentno smanjenje buke od 3-8 dB za sve ispitivane Reynoldsove brojeve uz istovremeno održavanje prihvatljivih aerodinamičkih performansi.

Na kraju, implementiran je napredni pristup dvosmjernog spajanja, koji uključuje generalizirani zakon zida, kako bi se omogućile visokovjerne simulacije koje obuhvaćaju specifične

fizičke pojave. Analiza krila s konačno definiranim rasponom otkriva utjecaj rubnog vrtloga krila na prijelaz graničnog sloja, koji se proteže od ruba krila i utječe na ukupne obrasce razvoja strujanja, uz nestabilnost sloja smicanja i mehanizme prijelaza graničnog sloja.

Integrirani metodološki okvir uspješno objašnjava detaljne aerodinamičke i aeroakustičke interakcije za konfiguracije beskonačnog i konačnog raspona s trokutastim i sinusoidalnim nazubljenjima tijekom faza ubrzanja i nakon ubrzanja, demonstrirajući dosljedne prednosti implementacije nazubljenja kroz smanjenje buke i poboljšanja stabilnosti za uvjete strujanja s umjerenim Reynoldsovim brojem.

**Ključne riječi:** Lattice Boltzmann metoda, nazubljeni prateći rub krila, simulacije velikih vrtloga, računalna dinamika fluida, aerodinamika, aeroakustika, prijelaz graničnog sloja, buka pratećeg ruba krila

# CONTENTS

<b>1</b>	<b>Introduction</b>	<b>1</b>
1.1	Research motivation . . . . .	1
1.2	Hypothesis and Aims of the Dissertation . . . . .	3
1.3	Background and Literature Review . . . . .	3
1.3.1	Lattice Boltzmann Method Applications in Aerodynamic Simulations .	4
1.3.2	Serrated Trailing Edges in Aeroacoustic and Aerodynamic Applications	6
1.3.3	LBM Applications in Serrated Airfoil Analysis . . . . .	9
1.4	Scientific Contributions . . . . .	11
1.5	Structure of the Dissertation . . . . .	13
<b>2</b>	<b>Experimental Wind Tunnel and Lattice Boltzmann Method Analysis of Aerodynamics in the Primary Airfoil</b>	<b>16</b>
2.1	Experimental setup . . . . .	16
2.2	Lattice Boltzmann Method . . . . .	20
2.3	Numerical Setup and Computational Domain Configuration . . . . .	26
2.4	Mesh Sensitivity Assessment . . . . .	31
2.5	Experimental results . . . . .	36
2.6	LBM Validation Against Experimental Results . . . . .	41
<b>3</b>	<b>Large Eddy Simulation Analysis of Aerodynamics and Aeroacoustics in the Serrated Airfoil</b>	<b>48</b>
3.1	Computational Methodology and Numerical Framework . . . . .	48
3.2	Geometry and Mesh Generation . . . . .	52
3.3	Primary Trailing Edge (PTE) Airfoil Analysis . . . . .	56
3.3.1	Force Analysis and Starting Vortex Dynamics . . . . .	56
3.3.2	Coupled Aerodynamic-Aeroacoustic Analysis of Boundary Layer Transition . . . . .	62
3.4	Comparative Analysis at $Re = 250,000$ : PTE vs. STE Airfoils . . . . .	70

3.5	Multi-Reynolds Number Analysis: PTE vs. STE Performance Comparison . . .	78
3.5.1	Force Characteristics and Boundary Layer Transition Analysis . . . . .	78
3.5.2	Aeroacoustic Analysis and Noise Reduction Quantification . . . . .	84
<b>4</b>	<b>Primary and serrated edge wings comparison with LBM analysis</b>	<b>93</b>
4.1	Three-dimensional wing geometry definition . . . . .	93
4.2	Numerical setup and wall model changes . . . . .	96
4.3	Aerodynamic Performance Analysis of PTE and STE Wings . . . . .	98
4.3.1	PTE Analysis and Validation . . . . .	98
4.3.2	Comparative Analysis: PTE vs. STE Wings . . . . .	101
<b>5</b>	<b>Conclusion</b>	<b>110</b>
	<b>List of Figures</b>	<b>127</b>
	<b>List of Tables</b>	<b>136</b>
	<b>List of Abbreviations</b>	<b>137</b>
	<b>Curriculum Vitae</b>	<b>139</b>
	<b>List of Publications</b>	<b>140</b>



# 1 INTRODUCTION

Computational fluid dynamics (CFD) research faces ongoing challenges in achieving both accuracy and efficiency in flow simulations. Traditional CFD methods often require significant computational resources and time, particularly when analyzing complex geometries or unsteady flow phenomena. Meanwhile, bio-inspired designs have emerged as a promising approach to address aerodynamic and aeroacoustic challenges. Serrated trailing edges, inspired by the silent flight of owls, have shown remarkable potential for simultaneously improving aerodynamic performance and reducing noise generation. Modern high-performance computing has enabled the investigation of these complex bio-inspired configurations using advanced numerical methods.

This dissertation addresses two equally important research areas: validating advanced computational methods for efficient CFD simulations and investigating the aerodynamic benefits of serrated trailing edge airfoils. The research demonstrates how the Lattice Boltzmann Method (LBM) can achieve high-fidelity results while leveraging modern computational hardware, and explores the impact of serrated trailing edges on aerodynamic efficiency and control flow separation. These bio-inspired configurations exhibit complex flow physics that necessitate sophisticated numerical approaches to fully comprehend their mechanisms. By combining advanced computational tools with bio-inspired design analysis, this work provides insights into both the development of more efficient simulation methods and the understanding of the intricate flow phenomena that make serrated airfoils effective for aerodynamic applications.

## 1.1 Research motivation

While conventional CFD methods are widely used to solve a range of engineering problems, each method has its own limitations and drawbacks. Generally, more detailed analyses require significantly greater computational time and resources. The rapid growth of High Performance Computing (HPC) [1] has enabled the development of advanced turbulence models and CFD approaches, ranging from Reynolds-Averaged Navier–Stokes (RANS) to Large Eddy Simulation (LES), and ultimately to Direct Numerical Simulation (DNS). These macroscopic approaches

are not the only means of addressing physical problems. Figure 1.1 illustrates the spectrum of methods used to describe physical phenomena with CFD.

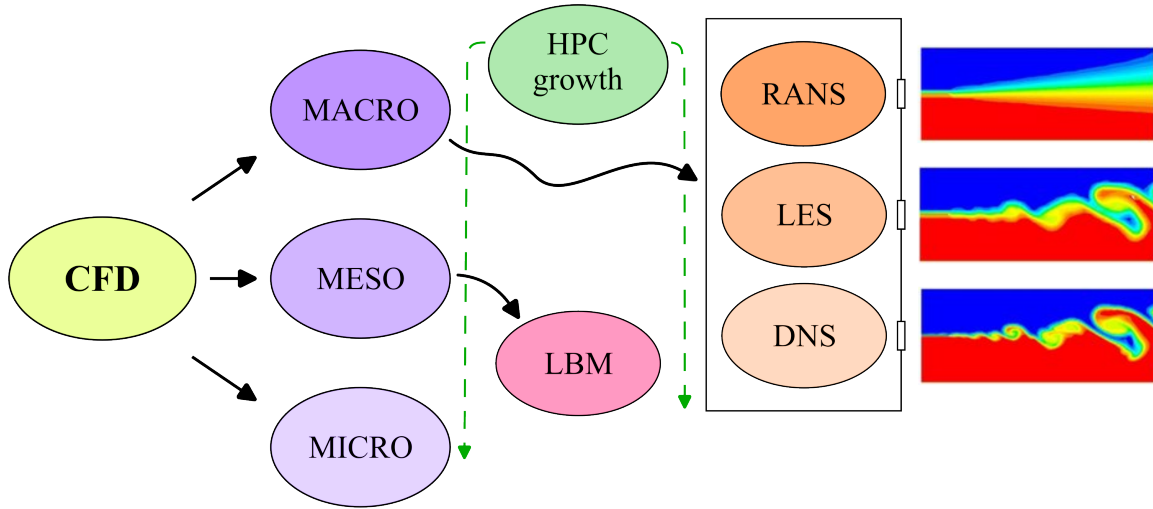


**Figure 1.1:** Classification of CFD methods across different scales, highlighting the mesoscopic position of the Lattice Boltzmann Method and the role of high-performance computing in enabling higher-fidelity turbulence modeling approaches.

This dissertation focuses primarily on the aerodynamic analysis of airfoils. Therefore, a microscopic approach would be unnecessarily detailed for the scope of this work. Instead, a mesoscopic approach offers a balanced perspective. Several recent studies, about which more details are revealed in Section 1.3, have identified the Lattice Boltzmann Method as a promising mesoscopic technique, especially for applications involving low Mach and Reynolds numbers. LBM’s ability to leverage advanced GPUs enables high-fidelity results with reduced computational time [2]. The current state of LBM and its supporting database motivates further exploration and enhancement of LBM for a wider range of applications, which will be investigated in this dissertation.

From a methodological standpoint, the study begins with classical airfoils, using aerodynamic analysis for validation against experimental data and benchmark cases from the literature. Beyond methodology, the focus extends to serrated trailing edge airfoils, which have garnered significant attention in recent years for their innovative design. Additionally, there has been considerable growth in bio-inspired airfoil analysis, which can be applied across various industries. This dissertation will emphasize its potential application to the aircraft industry. The primary interest in this field is centered on aeroacoustics and noise reduction. At the same time, other physical phenomena that have been underexplored in the literature have been explored in correlation with sound waves throughout this dissertation.



In summary, this research is driven by two primary motivations: (1) to implement advanced numerical methods for solving aerodynamic problems of airfoils, and (2) to analyze newly developed bio-inspired airfoils to assess their impact on aeroacoustic and aerodynamic performance.

## **1.2 Hypothesis and Aims of the Dissertation**

This dissertation is based on two main hypotheses: one from a methodological numerical perspective and the other from an aerodynamic design perspective. The hypotheses are as follows: (1) The application of advanced mesoscopic numerical methods, such as the Lattice Boltzmann Method (LBM), will provide accurate predictions of aerodynamic behavior for airfoil geometries at medium-range Reynolds numbers, as validated against experimental data; and (2) Serrated trailing edge (STE) airfoils will demonstrate a significant reduction in aeroacoustic noise compared to a primary straight-edge airfoil, with minimal compromise to aerodynamic efficiency at various medium-range Reynolds numbers and moderate angle of attack.

One of the primary aims of this dissertation is to validate the LBM against experimental data for incompressible flow around an airfoil at medium Reynolds numbers, a regime not extensively explored in the literature due to previous LBM limitations. These limitations will be addressed through methodological upgrades introduced in detail in Subsection 1.3. Furthermore, this work aims to investigate the physical phenomena associated with STE and primary trailing edge (PTE) airfoils, such as trailing edge noise, shear-layer noise, boundary layer instabilities (including laminar, transitional, and turbulent regions), laminar separation bubbles, and aerodynamic efficiency. The study will also consider the acceleration and post-acceleration phases of both airfoil types, with potential applications for aircraft take-off. Finally, this dissertation will provide a detailed analysis of the interdependence between aerodynamic and aeroacoustic performance.

## **1.3 Background and Literature Review**

This literature review examines the current state of research in the two primary areas addressed by this dissertation: advanced computational fluid dynamics methods and bio-inspired airfoil configurations. The review is organized into three complementary sections that progressively

build the theoretical foundation for this work. The first subsection examines the development and validation of the Lattice Boltzmann Method in aerodynamic applications, highlighting its advantages over traditional CFD approaches and recent advancements in collision operators and turbulence modeling. The second subsection reviews the growing body of research on serrated trailing edges, examining both their aerodynamic performance benefits and noise reduction mechanisms, with particular attention to the complex flow phenomena they generate. The final subsection synthesizes these areas by reviewing the emerging field of LBM applications in bio-inspired airfoil analysis, highlighting the unique capabilities of mesoscopic methods for capturing the intricate flow physics associated with serrated configurations. Together, these sections establish the scientific foundation for the methodological choices and research gaps addressed throughout this dissertation.

### **1.3.1 Lattice Boltzmann Method Applications in Aerodynamic Simulations**

Modeling complex physical phenomena in fluid dynamics has seen significant advancements with the introduction of the Lattice Boltzmann Method (LBM), which is increasingly favored by engineers and scientists for its computational efficiency and scalability, particularly on modern high-performance computing architectures such as GPUs [1–3]. Despite its growing popularity, one of the ongoing challenges remains the validation of numerical results, where a balance must be struck between computational simplicity, speed, and accuracy. While experimental analyses offer robust validation, they are often more costly and time-consuming than numerical simulations. Nevertheless, calibrating numerical models with experimental data is essential to ensure that simulations accurately represent real-world physical phenomena [2, 4]. Traditionally, CFD has relied on macroscopic approaches, such as the finite volume method (FVM), finite element method (FEM), and finite difference method (FDM), which directly solve the Navier-Stokes equations to obtain variables like pressure and velocity [5, 6]. However, with the rapid advancements in computational hardware, most notably general-purpose GPU computing, alternative methods such as LBM and Smoothed Particle Hydrodynamics (SPH) have gained traction due to their inherent parallelism and flexibility [2, 3, 7].

Unlike conventional CFD methods, LBM operates at the mesoscopic scale, solving a Boltzmann equation to model the statistical behavior of fluid particle populations [8, 9]. This approach enables LBM to efficiently handle complex boundary conditions and multiphase or multiscale flows. The foundational work of McNamara and Zanetti [10], as well as Higuera and Jiménez [11], established LBM as a viable CFD technique, and subsequent developments have expanded its theoretical and practical scope. The evolution of LBM from a theoretical curiosity to a practical engineering tool has been particularly pronounced in aerodynamic applications, where its natural ability to capture both flow dynamics and acoustic phenomena simultaneously has proven invaluable [2, 9].

Recent research has demonstrated the suitability of LBM for external aerodynamic applications, including the simulation of flow around airfoils and complex geometries across a range of Reynolds numbers [12–15]. For instance, Imamura *et al.* [12] applied a two-dimensional LBM with a D2Q9 velocity set to model flow around a NACA 0012 airfoil at Reynolds numbers up to 500,000, validating their results against both experimental data and traditional CFD codes. The integration of the Immersed Boundary method with LBM (IB-LBM) has further enhanced the method’s ability to model complex, moving boundaries, as shown in studies by Peng *et al.* [13], Wu and Shu [14], and Qiu *et al.* [15]. Furthermore, IB-LBM has been modified through the bounce-back method by Wang *et al.* [16]. These advancements have enabled accurate simulations of both incompressible and compressible flows over airfoils, with improvements in boundary condition enforcement and computational efficiency.

A key area of ongoing development in LBM is the selection of collision operators and turbulence modeling strategies. The single-relaxation-time Bhatnagar–Gross–Krook (BGK) operator remains widely used for its simplicity [17–19], but alternative formulations such as the Multiple Relaxation Time (MRT) operator [20, 21] and cascaded or cumulant-based operators [22, 23] have been introduced to enhance numerical stability and accuracy, particularly at higher Reynolds numbers and in turbulent regimes. Turbulence models such as Reynolds-Averaged Navier–Stokes (RANS) [24, 25], Large Eddy Simulation (LES) [26, 27], and hybrid approaches have also been successfully coupled with LBM to capture a wide spectrum of flow phenomena.

Validation studies confirm the reliability of LBM for simulating aerodynamic flows over airfoils at both low and high Reynolds numbers. For example, Reyes Barraza and Deiterding [28] extended LBM to non-uniform grids for various angles of attack and low Reynolds number

flows (up to 12,000), using the BGK collision operator and D2Q9 velocity set. In contrast, Zhuo *et al.* [29] and Hejranfar and Saadat [30] demonstrated LBM’s capability for high Reynolds number simulations using D2Q13 and D2Q9 velocity sets, respectively. Recent work has also emphasized the importance of three-dimensional simulations: Leveque *et al.* [31] used a D3Q19 lattice and BGK operator for low Reynolds number 3D flow predictions, while Degrieny *et al.* [32] and Wilhelm *et al.* [33] explored LBM-LES and LBM-RANS approaches for higher Reynolds number airfoil flows.

Overall, LBM has developed into a robust and versatile tool for aerodynamic simulations. Its ongoing advancements, particularly in collision operators, turbulence modeling, and boundary condition treatments, position LBM as a promising alternative to traditional CFD methods for both fundamental research and engineering applications [2, 7]. Notably, recent studies on high Reynolds number flows have predominantly employed the D3Q19 velocity set for three-dimensional simulations [31–33]. However, with the increasing availability of computational resources, especially general-purpose GPUs, it is now feasible to utilize the more computationally intensive D3Q27 velocity set, which offers improved isotropy and rotational invariance [34–36].

This opens new opportunities to explore the performance of more advanced collision operators, such as the MRT [37, 38] or cumulant-based schemes, the latter of which has demonstrated the best accuracy and performance among collision operators in cylinder benchmark cases [39]. Recent studies by Krenchiglova *et al.* [40] have investigated various collision operators (BGK, SRT, moment-based models) for NACA 0012 flows, though primarily focusing on low Reynolds number regimes (up to 1,000). Investigating these combinations could further enhance the accuracy and stability of LBM for aerodynamic applications, such as simulating fluid flow around airfoils at medium and high Reynolds numbers. Likewise, the continued development of these methodological advances provides a strong foundation for tackling increasingly complex aerodynamic challenges, including those posed by bio-inspired configurations with intricate geometric features.

### **1.3.2 Serrated Trailing Edges in Aeroacoustic and Aerodynamic Applications**

The aerodynamic and aeroacoustic performance of bio-inspired airfoil configurations has become a central topic in contemporary aerospace research, particularly due to the dual challenge

of optimizing aerodynamic efficiency and mitigating noise emissions during unsteady flow conditions. The complexity of fluid-structure interactions, stability, and noise generation in such scenarios has driven the development and analysis of various flow control devices. These devices are generally categorized into active controls, such as suction, blowing, and wall oscillations, and passive controls, which include vortex generators, shock control bumps [41, 42], and, most notably, trailing edge modifications like serrations.

Serrated trailing edges (STEs), often inspired by the silent flight of owls, represent a prominent passive modification that has garnered significant attention in the aeroacoustic community (Figure 1.2). The foundational analytical framework for STEs was established by Howe [43], who demonstrated that the effectiveness of noise reduction is closely linked to the serration length ( $2h$ ) and wavelength ( $\lambda$ ). Since then, a series of analytical and semi-analytical models, frequently building on Amiet’s theory [44], have been developed to predict noise reduction for a variety of leading [45] and trailing edge geometries [46, 47]. These theoretical advances are complemented by comprehensive reviews on noise reduction technologies for aircraft [48, 49], including airframe and landing gear noise [50], and the emerging field of acoustic metamaterials [51]. The integration of these theoretical frameworks with advanced computational methods has opened new avenues for understanding the complex physics underlying bio-inspired noise reduction mechanisms.

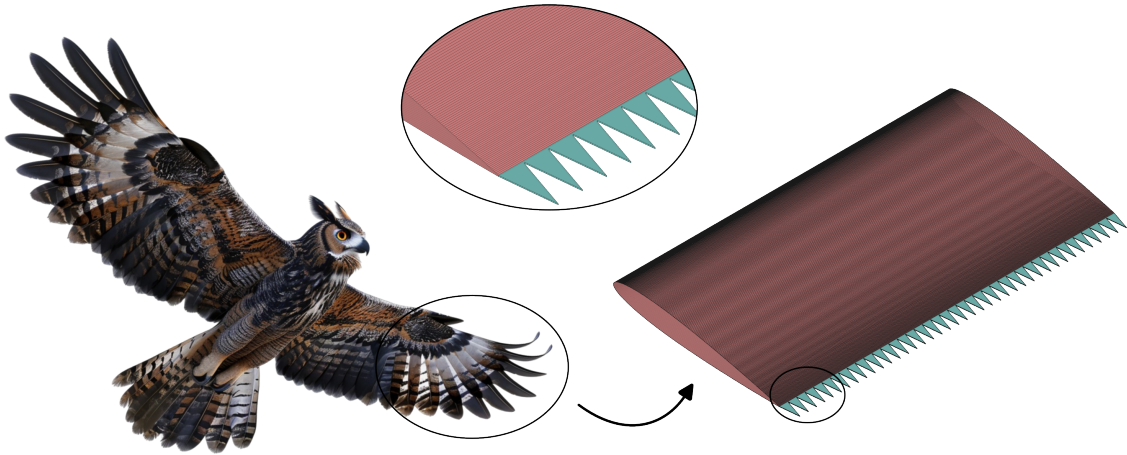


**Figure 1.2:** 3D model representation of the owl wing serrations.

A comprehensive review by Weger *et al.* [52] delves into the engineering insights derived from owl wing morphology, highlighting features that contribute to their renowned silent flight capabilities. Oerlemans *et al.* [53] conducted a notable study examining the acoustic effects of serrations on wind turbine blades, comparing conventional, serrated, and optimized airfoil

shapes, and reporting noise reductions of 0.5 dB and 3.2 dB for optimized and serrated configurations, respectively. To further investigate these phenomena, researchers have employed advanced computational and experimental techniques, such as transient compressible lattice Boltzmann methods [54, 55] and direct numerical simulation [56], alongside wind tunnel experiments for flat plate serrations [57] and airfoils equipped with STEs [58, 59]. The convergence of these diverse methodological approaches has been instrumental in advancing the overall science community’s understanding of the underlying flow physics and acoustic generation mechanisms.

In the past five years, a growing body of research has expanded understanding of STEs through both experimental measurements [60–66] and CFD simulations [67–73]. These studies have deepened insights into complex flow phenomena, refined noise modeling techniques, and advanced experimental methodologies, thereby narrowing the gap between numerical simulations and practical applications. For example, Wei *et al.* [74] combined experimental and CFD approaches to design a novel propeller that integrates owl feather serrations with cicada wing geometry; this 3D sinusoidal serration configuration achieved up to a 5.5 dB reduction in sound pressure and over 20% improvement in propulsive efficiency, offering a promising avenue for quieter, more efficient aerial vehicles. Such innovations demonstrate the potential for bio-inspired designs to address multiple performance objectives simultaneously.

The studies mentioned above have also explored a variety of airfoil and wing geometries. Celik *et al.* [62] provided experimental evidence of noise reduction using large-scale serrations on flat plates. Hasheminasab *et al.* [63] utilized time-resolved planar Particle Image Velocimetry (PIV) in the airfoil wake, both with and without serrations, to analyze noise and apply Proper Orthogonal Decomposition (POD) for assessing dominant wake structures. PIV was also central to noise-reduction investigations by Pereira *et al.* [65] and Sumesh *et al.* [66], while Pereira *et al.* [64] extended this by measuring steady aerodynamic performance with PIV and surface pressure taps, focusing on physical flow mechanisms influencing wall-pressure fluctuations over STEs rather than noise reduction alone. Zhao *et al.* [61] placed greater emphasis on the aerodynamic performance of STEs, reporting optimizations in lift-to-drag ratio and lift coefficient by 1.9% and 32.5%, respectively. Additionally, Zhou *et al.* [60] incorporated deformation measurements to further elucidate the interplay between aerodynamic forces and noise reduction mechanisms.

Notably, all recent CFD studies addressing STE flow analysis, aerodynamic performance,

and noise reduction have relied on LES to solve the Navier-Stokes equations. Several works have focused specifically on noise mitigation. For example, Wang *et al.* [70] demonstrated that innovative asymmetric serrations can yield an additional noise reduction of 3.68 dB. Cao *et al.* [67] introduced a novel modeling approach by parameterizing serration features and incorporating extra lift and drag sources directly into the momentum equation to simulate STE effects. Song *et al.* [71] developed a Multi-Flapped-Serration with Iron-Shaped Edges (MFS-Iron) to control turbulence-induced noise at the trailing edge of wind turbine airfoils.

Further innovations include the Insert-type Porous-Serrated (IPS) trailing edge with variable porosity designed by Hu *et al.* [73], which achieved a 5.21 dB noise reduction, albeit with an 8.0% increase in drag. Lai *et al.* [72] proposed the application of STE designs in high-speed, near-wall environments to reduce trailing edge noise for an aero-train, a novel ground effect vehicle. Gelot and Kim [68] also investigated noise reduction, but placed greater emphasis on flow phenomena such as the Laminar Separation Bubble (LSB), finding that STEs decrease the amplitude of acoustic source pressure in transitional regions and promote destructive phase interference in wall pressure fluctuations near the trailing edge, thereby weakening the acoustic feedback loop. Similarly, Hu *et al.* [69] examined the interplay between flow structures and acoustic sources using Dynamic Mode Decomposition (DMD), revealing how pressure structures change with serration length. Their study also underscored the need for further research to address the balance between aerodynamic performance and noise reduction.

Overall, comprehensive aerodynamic investigations that simultaneously incorporate noise reduction for STE configurations remain relatively scarce in the literature. This gap presents an opportunity to explore, in greater detail, both the aerodynamic and aeroacoustic perspectives and their interdependence for primary and serrated trailing edges. Furthermore, to the author's knowledge, no studies have examined the acceleration and post-acceleration phases for STE airfoils. It will therefore be of particular interest to determine whether some of the benefits and limitations identified in previous works can be translated to these transient phases.

### **1.3.3 LBM Applications in Serrated Airfoil Analysis**

The application of the Lattice Boltzmann Method to bio-inspired aeroacoustic configurations represents a rapidly evolving research area that bridges the computational advantages of LBM with the growing demand for quieter, more efficient aerodynamic systems. This convergence

has been driven by LBM's inherent suitability for aeroacoustic simulations, particularly its ability to capture both flow dynamics and acoustic wave propagation within a single computational framework, making it ideally suited for investigating the complex physics underlying bio-inspired noise reduction mechanisms.

Recent research has demonstrated the effectiveness of LBM in analyzing serrated configurations across multiple scales and applications. Buszyk *et al.* [75] conducted comprehensive investigations of turbofan aeroacoustics with serrated stators, achieving significant noise reductions of up to 3 dB from broadband intake radiation and 6 dB in the bypass duct, with an additional 4 dB reduction at the blade passing frequency. Their work exemplifies LBM's capability to handle industrial-scale aeroacoustic problems with complex geometries, providing validation against both experimental measurements and traditional CFD approaches.

The versatility of LBM in bio-inspired aeroacoustic applications extends beyond traditional turbomachinery to encompass a diverse range of configurations and operating conditions. Kim *et al.* [76] utilized LBM for aeroacoustic analysis of dual-type combined fans incorporating serrated trailing edges, demonstrating the method's effectiveness in capturing the complex flow phenomena associated with these bio-inspired modifications. Similarly, van der Velden *et al.* [77] employed LBM for full-scale serrated wind turbine trailing edge noise certification analysis, highlighting the method's scalability from laboratory configurations to industrial applications. These studies collectively demonstrate LBM's ability to maintain accuracy across different Reynolds number regimes and geometric complexities, establishing it as a robust tool for bio-inspired aeroacoustic design.

Buszyk *et al.* [78] demonstrated methodology in their assessment of rectilinear cascades with leading edge serrations, employing analytical models for initial design, Euler-based methods for preliminary validation, and high-fidelity LBM simulations for final verification. Their findings revealed that while fast design methods and mid-fidelity simulations provided satisfactory trends, only high-fidelity LBM simulations accurately matched experimental acoustic spectra and sound power level reductions.

Avallone *et al.* [55] provided crucial insights into the noise reduction mechanisms of sawtooth and combed-sawtooth trailing-edge serrations, revealing that sawtooth serrations reduce noise through destructive interference between sound waves generated at different spanwise locations, while combed-sawtooth configurations introduce additional complexity through their



three-dimensional geometry. Their work demonstrated that the effectiveness of these mechanisms depends critically on the serration geometry and the incoming turbulent flow characteristics, highlighting the importance of detailed flow field analysis that LBM can provide.

The geometric complexity studies have revealed the potential for innovative hybrid designs that leverage multiple noise reduction mechanisms simultaneously. The understanding of how different serration geometries influence the flow field and acoustic characteristics has been crucial for developing more effective bio-inspired solutions. The work by Avallone *et al.* [55] on combed-sawtooth configurations particularly exemplifies how LBM can capture the intricate three-dimensional flow phenomena that govern the effectiveness of complex bio-inspired geometries, providing insights that would be difficult to obtain through simplified analytical approaches or lower-fidelity computational methods.

Halimi *et al.* [79] addressed the challenges specific to small-scale applications through analytical prediction methods for mini-RPA propellers with serrated edges, while Sanjosé *et al.* [80] employed comprehensive multi-fidelity strategies combining analytical, numerical, and experimental approaches for trailing-edge noise reduction investigations. These complementary methodologies, spanning from Reynolds number effects and geometric scaling considerations to detailed experimental validation, ensure that benefits observed in simplified academic configurations can be reliably translated to more complex, industrially relevant geometries.

The current state of LBM applications in bio-inspired aeroacoustic design represents a mature but still evolving field. While significant progress has been made in demonstrating the method's effectiveness across various applications and scales, opportunities remain for expanding its application to more complex configurations and operating conditions. The gap between current capabilities and the full potential of bio-inspired aeroacoustic and exceptionally aerodynamic design, which is underrepresented in the literature, provides a compelling motivation for continued research in this area. The continued advancement of computational hardware, particularly GPU architectures, will further expand the feasibility of conducting comprehensive studies using high-fidelity LBM simulations.

## 1.4 Scientific Contributions

This dissertation makes three primary scientific contributions:

- Validation of the LBM for simulating fluid flow around an airfoil at medium Reynolds numbers and various angles of attack (AoA), utilizing advanced approaches such as the cumulant collision operator and the D3Q27 velocity set, which are currently underrepresented in the literature.
- Detailed analysis of aerodynamic and aeroacoustic interdependence, for both primary and serrated trailing edge airfoils during the initial acceleration and post-acceleration phases.
- Synthesis of insights from LBM simulations of the primary airfoil and LES results for both primary and serrated airfoils to investigate the performance of bio-inspired airfoil configurations with LBM.

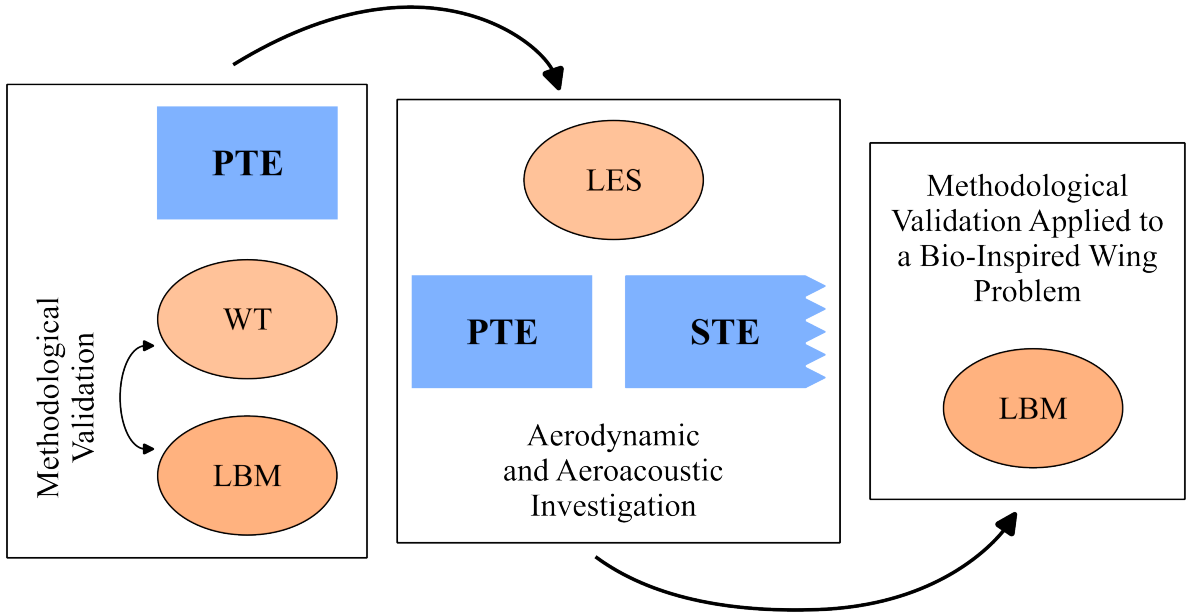


**Figure 1.3:** Visualized and simplified main scientific contributions that also correlate with the dissertation structure.

From these main contributions, several additional outcomes are derived:

- Expansion of the wind tunnel measurement dataset for the NACA 0012 airfoil at various angles of attack using an open-circuit wind tunnel.
- Provision of high-fidelity three-dimensional LBM analyses of airfoil flows, addressing a gap in the literature where two-dimensional studies are more prevalent.
- Extension of LES datasets for airfoil flows, with a focus on the initial acceleration phase, which remains unexplored for serrated trailing edges (STE).

- In-depth analysis of laminar, transitional, and turbulent boundary layer development.
- Investigation of trailing edge noise and its influence on the boundary layer, with particular emphasis on the laminar separation bubble (LSB).
- Assessment of aerodynamic efficiency during acceleration and post-acceleration phases.
- Insights into HPC hardware usage, including both CPUs and GPUs.
- Expansion of the NACA 0012 and Joukowski primary and serrated edge airfoil databases for various angles of attack, Mach numbers, and Reynolds numbers.
- Implementation of two-way coupling with the Generalized Law of the Wall for solving high-fidelity LBM-LES analysis of the serrated trailing edge wings.
- Investigation of infinite and finite span wings.

## 1.5 Structure of the Dissertation

This dissertation is organized into five main chapters. Chapter 1 introduces the research motivation, defines the hypotheses and aims, and presents a detailed literature review that highlights existing gaps in the field. The scientific contributions of this work are also outlined in this chapter.

Chapter 2 presents and validates a comprehensive numerical framework for analyzing fluid flow around airfoils using the Lattice Boltzmann Method (LBM). The chapter begins with experimental investigations conducted in an open-circuit wind tunnel for a NACA 0012 airfoil at a medium Reynolds number of 191,000, covering angles of attack of  $2^\circ$ ,  $4^\circ$ ,  $6^\circ$ , and  $8^\circ$ . Following a detailed exposition of LBM theory and its mesoscopic approach to fluid dynamics modeling, the chapter describes the numerical setup using Altair’s UltraFluidX solver with D3Q27 velocity sets and high-fidelity cumulant-based collision operators. A systematic mesh sensitivity analysis establishes grid independence using four different mesh configurations, while experimental uncertainty quantification provides statistical validation of the wind tunnel measurements. The chapter concludes with a comprehensive validation of LBM-LES predictions against experimental pressure coefficient distributions, demonstrating excellent agreement with Root Mean Square Errors below 0.1 and correlation coefficients exceeding 0.86 across all test cases. This validation establishes the reliability of the computational framework for subsequent analyses of

bio-inspired airfoil configurations and provides the foundation for the advanced investigations of flow phenomena presented in the following chapters.

Chapter 3 addresses the identified gap in the literature concerning the mutual aerodynamic and aeroacoustic influences in STE airfoil configurations. This chapter investigates and visualizes the acoustic-aerodynamic correlation for a symmetrical airfoil in accelerating flow, considering Reynolds numbers from 100,000 to 500,000 at Mach 0.25, with a focus on  $Re = 250,000$ . These parameters, along with the inclusion of an acceleration phase, are selected for their relevance to smaller aircraft and unmanned aerial vehicle (UAV) applications. The chapter details the methodology, including governing equations, computational setup, and grid validation. It provides a thorough analysis of both PTE and STE airfoils, examining their aerodynamic, aeroacoustic, and stability characteristics individually and comparatively. Additionally, the chapter explores STE behavior during both acceleration and post-acceleration phases, elucidating complex unsteady phenomena such as boundary layer instabilities, laminar separation bubble dynamics, and interactions between sound waves and streamwise fluid flow.

Chapter 4 integrates the validated LBM framework from Chapter 2 with the advanced flow physics understanding from Chapter 3 to conduct a 3D flow analysis of wing serrations under realistic finite-span conditions. This chapter illustrates the transition from two-dimensional idealized studies to practical finite-wing applications. Utilizing enhanced UltraFluidX version 2025 with advanced adaptive two-way coupling and Generalized Law of the Wall modeling, the analysis encompasses both primary trailing edge (PTE) and serrated trailing edge (STE) wings with triangular and sinusoidal variants across multiple angles of attack ( $2^\circ$ ,  $4^\circ$ ,  $6^\circ$ , and  $8^\circ$ ). It implements finite-span conditions of 0.3 m (200% chord length) to capture realistic three-dimensional effects, including tip vortices and induced drag. It reveals angle-dependent serration effectiveness with STE wings showing a 4.26% improved lift performance and enhanced stability at higher angles of attack. Advanced flow visualization, utilizing the  $Q$ -criterion and vorticity analysis, elaborates complex phenomena such as boundary layer transition, wake region development, Kelvin-Helmholtz instabilities, and wing tip vortex formation. Computational performance analysis reveals the enhanced fidelity achieved through sophisticated wall modeling approaches, albeit at a higher computational cost, with runtimes exceeding 33 hours and nearly doubling memory requirements compared to simpler modeling approaches from Chapter 2.

Finally, Chapter 5 summarizes the key findings and contributions of this study.

Several chapters of this dissertation have been published as research articles as part of the author's progress during the PhD. Chapter 2 includes elements from a research article published in the *International Journal of Numerical Methods for Heat & Fluid Flow* (Q1 exc.) [81]. Additionally, portions of Chapter 3 are based on an accepted manuscript in *Advances in Aerodynamics* (Q1).

## 2 EXPERIMENTAL WIND TUNNEL AND LATTICE BOLTZMANN METHOD ANALYSIS OF AERODYNAMICS IN THE PRIMARY AIRFOIL

This chapter presents an examination of fluid flow around a NACA0012 airfoil, with the aim of validating the numerical results obtained using the Lattice Boltzmann Method (LBM) against experimental results obtained in a wind tunnel at a medium Reynolds number ( $Re = 191,000$ ). The Reynolds number of 191,000 represents a transitional regime where the boundary layer exhibits characteristics of both low and high Reynolds number flows, making it particularly challenging for numerical methods and ideal for validation studies [82].

First, Section 2.1 presents the experimental setup of the NACA 0012 airfoil in an open-circuit wind tunnel. Section 2.2 provides a broader overview of the Lattice Boltzmann Method, while Section 2.3 offers detailed information about configuring Altair's UltraFLuidX 2021 LBM software with appropriate mesh analysis in Section 2.4. Finally, Section 2.5 presents experimental results, while Section 2.6 compares numerical results with experimental data.

### 2.1 Experimental setup

Wind tunnels are classified into two primary categories based on their flow circulation characteristics: open-circuit (also known as Eiffel-type) and closed-circuit (also known as Göttingen-type) wind tunnels. The fundamental distinction lies in the air flow path and circulation pattern employed in each design [83, 84].

Open-circuit wind tunnels draw air from the surrounding environment and discharge it back into the atmosphere after it has passed through the test section. This configuration offers several distinct advantages, including lower construction costs, superior performance for propulsion and smoke visualization studies due to the absence of exhaust product accumulation, and easier access to the test section for model installation and maintenance [83]. However, open-circuit

designs also present certain limitations, including higher power consumption requirements, potential for poor flow quality due to atmospheric influences, increased noise levels, and higher operating costs due to the continuous need to accelerate fresh air through the tunnel [85].

In contrast, closed-circuit wind tunnels recirculate air within a closed loop system, returning the air from the exit through a series of ducts and turning vanes back to the contraction section. This design philosophy yields several operational advantages: significantly lower power consumption for a given test section velocity (approximately one-third of open-circuit requirements), superior flow quality control through isolation from external atmospheric disturbances, reduced noise levels, and the ability to maintain controlled atmospheric conditions, including temperature and humidity regulation. The primary disadvantages of closed-circuit designs include substantially higher construction costs (typically three times that of equivalent open-circuit tunnels), larger facility space requirements, potential air heating issues during extended operation, and more complex maintenance procedures due to limited access to internal components [83].

For the present experimental investigation, an open-circuit wind tunnel was selected primarily due to cost considerations and the specific requirements of the validation study. The relatively moderate Reynolds number ( $Re = 191000$ ) and short-duration testing protocol make the higher power consumption acceptable, while accessibility of the wind tunnel's test section eases the experimental procedure of calibrating the tunnel, changing the Pitot tube position, and varying the angle of attacks.

The experiment was conducted using TecQuipment's ISO 9001 certified open-circuit suction AF1300 subsonic wind tunnel with a test section measuring 305 mm  $\times$  305 mm  $\times$  600 mm. The Open-circuit wind tunnel is designed to draw air from the atmosphere through an aerodynamically designed conical contraction section, which accelerates the air linearly due to the reduction in cross-sectional area. A honeycomb section is positioned at the inlet, which serves as a flow conditioning device that straightens the flow and reduces large-scale turbulent structures. An axial fan positioned after the diffuser section extracts air and returns it to the atmosphere. The complete wind tunnel assembly measures 3700 mm in length, 1065 mm in width, and 1900 mm in height.

Experimental data are obtained using several ISO 9001 certified TecQuipment sensors located within the test section. Figure 2.1 provides an overall overview of the open-circuit wind

tunnel used for the experiment, with emphasis on the main components and measurement instrumentation. Two Pitot-static tubes are connected to the AFA5 differential pressure unit with a measurement range of  $\pm 7$  kPa. Additionally, 20 static pressure tapings are connected to a manifold system that feeds into the AFA6 32-Way Pressure Display Unit, also with a range of  $\pm 7$  kPa. A protractor and model holder for precise angle adjustment are located at the rear of the test section.

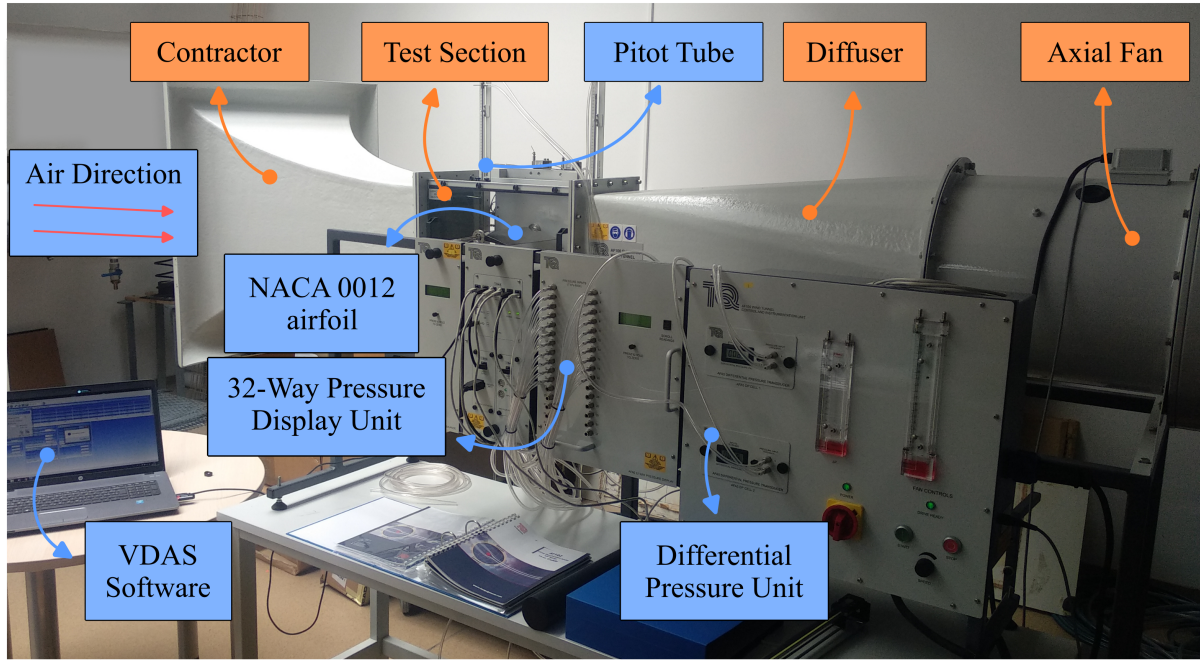


**Figure 2.1:** Subsonic open-circuit wind tunnel with four main flow path components highlighted in orange, while sensors, control panel, software, and airfoil are displayed in blue.

The experimental procedure begins with positioning the Pitot-static probe 30 mm from the top wall of the test section. Pitot-static tubes operate on Bernoulli's principle, measuring both total pressure (through the forward-facing pitot port) and static pressure (through side ports perpendicular to the flow). The dynamic pressure, calculated as the difference between total and static pressure, directly relates to velocity through  $q = \frac{1}{2}\rho V^2$ , enabling accurate velocity measurements in subsonic flows [82]. Initially, the optimal position of the Pitot-static tube is calibrated to minimize boundary layer effects in the stabilized flow field. This calibration procedure is essential because boundary layer thickness near the tunnel walls can significantly affect velocity measurements. The boundary layer displacement thickness typically grows along the tunnel walls, requiring careful probe positioning to ensure measurements in the free stream region [83]. Following the calibration procedure, the NACA 0012 airfoil is positioned within the test section and analyzed at a Reynolds number of 191,000.



The NACA 0012 airfoil dimensions are 150 mm chord length and 300 mm span length, resulting in an aspect ratio of 2.0. This aspect ratio places the wing in the finite-wing category where three-dimensional effects become significant. However, for validation purposes, the central portion of the wing experiences predominantly two-dimensional flow characteristics, making it suitable for comparison with 2D numerical simulations [82]. The airfoil incorporates 20 static pressure tappings distributed along the chord, with equal geometric distribution on the upper and lower surfaces. The geometric distribution of tapping positions is presented in Table 2.1, showing the exact distance from the leading edge for each measurement point.

**Table 2.1:** Pressure tapping positions for surface pressure measurement on the NACA 0012 airfoil.

Upper surface tapping	Distance from leading edge [mm]	Lower surface tapping	Distance from leading edge [mm]
1	0.76	2	1.52
3	3.81	4	7.62
5	11.43	6	15.24
7	19.05	8	22.86
9	38.00	10	41.15
11	62.00	12	59.44
13	80.77	14	77.73
15	101.35	16	96.02
17	121.92	18	114.30
19	137.16	20	129.54

The distribution of pressure tappings is designed to capture critical flow features, with a higher density near the leading edge, where pressure gradients are steepest, and a lower density afterwards, where pressure variations are more gradual. This distribution follows established practices in experimental aerodynamics for obtaining accurate pressure coefficient distributions [84].

To obtain reliable experimental results, several procedural steps are necessary. First, the airfoil's trailing edge is positioned at the same height as the centerline of the model holder to ensure proper flow alignment. Second, all tube connections are verified, and after the flow field stabilizes, sensors begin recording experimental values. TecQuipment's Versatile Data Acquisition System (VDAS) software is employed to record and export experimental data. Relevant experimental values are recorded every 0.5 seconds over a total duration of 300 seconds to ensure adequate statistical sampling. This sampling frequency and duration provide sufficient

data points for statistical analysis while avoiding aliasing effects and ensuring convergence of time-averaged quantities [85].

All recorded values are time-averaged, and for quantitative analysis, the pressure coefficient  $C_p$  (defined in Equation 2.1) serves as the primary benchmark for comparison and validation.  $C_p$  is a non-dimensional parameter that quantifies the ratio of local pressure difference to dynamic pressure of the fluid. It is fundamental in aerodynamics as it represents the normalized pressure field around the body. Values of  $C_p = 0$  indicate static pressure equal to free stream pressure,  $C_p = 1$  corresponds to stagnation conditions, and negative values indicate local pressure below free stream pressure, typically occurring in accelerated flow regions [82].

$$C_p = \frac{p - p_\infty}{\frac{1}{2}\rho_\infty v_\infty^2} \quad (2.1)$$

The subscript  $\infty$  denotes free stream conditions measured away from the airfoil's influence, specifically representing the undisturbed air passing through the test section. Therefore,  $p_\infty$  represents the wall static pressure, while  $p$  corresponds to the pressure at individual tapping points on the airfoil surface.  $v_\infty$  specifies the velocity at the test section inlet, and  $\rho_\infty$  defines the air density within the test section.

The wind tunnel test section operates under the following conditions: atmospheric temperature of 27°C, atmospheric pressure of 1015.2 mbar, ambient air density of 1.18 kg/m<sup>3</sup>, and inlet air velocity of 20 m/s. These operating conditions correspond to standard atmospheric conditions with slight temperature elevation. It ensures incompressible flow conditions with Mach numbers well below 0.3, specifically 0.0576, where compressibility effects are negligible. The experiment was conducted at four different angles of attack: 2°, 4°, 6°, and 8°, encompassing the linear lift region of the NACA 0012 airfoil.

## 2.2 Lattice Boltzmann Method

The Lattice Boltzmann Method (LBM) was developed as a solution to overcome the limitations of particle-based lattice gas automata models, which suffered from statistical noise and limited applicability to realistic fluid flow problems. While microscopic models track individual particles at the molecular level, their dynamics are too complex for practical computational fluid dynamics modeling. LBM operates at the mesoscopic scale, tracking particle distribution functions rather than individual particles. The mesoscopic approach bridges the gap between

the microscopic kinetic description of molecular motion and the macroscopic continuum equations of fluid mechanics. This intermediate scale captures the essential physics of fluid flow while avoiding the computational complexity associated with molecular dynamics simulations. All together, it provides an optimal balance between physical accuracy and computational efficiency [2, 9].

A microscopic description entails tracking particles at the molecular level; however, observing particles within a defined control volume allows for significant simplification. The left panel of Figure 2.2 illustrates this concept. Each particle within the observed volume possesses an individual velocity (yellow vectors). When all velocity vectors are summed and divided by the number of particles in the constrained volume, the average or bulk flow velocity (red vector) is obtained. Individual particles exhibit velocity deviations from the average velocity, representing thermal or chaotic motion (blue vectors). These velocity deviations sum to zero and can be neglected in the macroscopic description (closed light blue vector loop).

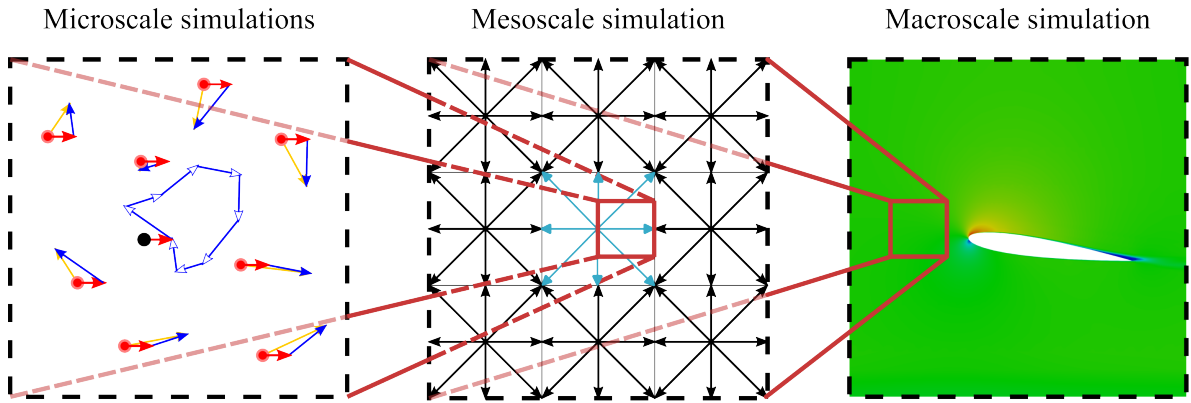


**Figure 2.2:** Scale hierarchy in CFD: microscale molecular dynamics (left) captures individual particle motion, mesoscale LBM (center) tracks particle distribution functions on a regular lattice, and macroscale continuum methods (right) solve macroscopic field variables.

The LBM approach tracks particle distribution functions instead of individual particles (center panel of Figure 2.2), providing computational advantages in terms of both efficiency and accuracy. This statistical mechanics foundation ensures that LBM naturally incorporates the molecular origins of fluid behavior while remaining computationally tractable for engineering applications. LBM is based on kinetic theory, where the fundamental variable is the particle distribution function  $f(\mathbf{x}, \boldsymbol{\xi}, t)$ . This function represents the probability density of finding particles with velocity  $\boldsymbol{\xi} = (\xi_x, \xi_y, \xi_z)$  at position  $\mathbf{x}$  and time  $t$ .

The temporal evolution of the particle distribution function follows from the total time derivative:

$$\frac{df}{dt} = \left( \frac{\partial f}{\partial t} \right) \frac{dt}{dt} + \left( \frac{\partial f}{\partial x_\beta} \right) \frac{dx_\beta}{dt} + \left( \frac{\partial f}{\partial \xi_\beta} \right) \frac{d\xi_\beta}{dt} \quad (2.2)$$

where subscript  $\beta$  represents spatial coordinate directions or components of vectors in the coordinate system.

From Equation 2.2, particle velocity should be written as  $dx_\beta/dt = \xi_\beta$ , while the specific body force from Newton's second law is  $d\xi_\beta/dt = F_\beta/\rho$ . Also, for changing the total differential with the collision operator as  $\Omega(f) = df/dt$ , the Boltzmann equation is obtained (2.3):

$$\frac{\partial f}{\partial t} + \xi_\beta \frac{\partial f}{\partial x_\beta} + \frac{F_\beta}{\rho} \frac{\partial f}{\partial \xi_\beta} = \Omega(f) \quad (2.3)$$

where  $F_\beta$  represents the  $\beta$ -component of the external body force acting on the particles.

The Boltzmann equation can be interpreted as a hyperbolic advection equation where the first two terms represent free streaming of the distribution function in phase space. The third term represents how external forces change the particle velocity distribution function. The collision operator on the right-hand side describes the redistribution of particles due to intermolecular collisions. The local nature of the collision operator, which depends only on  $f$  and not its gradients, is fundamental to LBM's computational efficiency and excellent parallelization properties [2].

The discrete-velocity distribution function  $f_i$ , commonly referred to as particle populations, forms the cornerstone of the LBM approach. The fundamental distinction between the continuous distribution function  $f$  and the discrete populations  $f_i$  lies in the discretization of velocity space. While  $f$  represents a continuous function in velocity space,  $f_i$  is defined only at specific discrete velocities. To derive the LBM equation, the Boltzmann equation must be discretized in velocity space, physical space, and time [2, 20].

Spatial discretization is achieved by dividing the computational domain into regular cubic elements called voxels, each with edge length  $\delta x$ . This approach parallels classical finite difference methodologies. Temporal discretization employs uniform time steps  $\delta t$ , ensuring that the distribution function is defined at voxel centroids at each discrete time level. The choice of spatial and temporal discretization parameters is constrained by stability requirements, typically expressed through the Courant-Friedrichs-Lewy (CFL) condition [2].

Velocity space discretization leads to the determination of the discrete velocity set  $\{\mathbf{c}_i\}$ .

Each velocity set employs the notation DdQq, where  $d$  represents the number of spatial dimensions and  $q$  denotes the number of discrete velocities. The selection of velocity sets involves a trade-off between computational cost and accuracy, with higher-order sets providing better isotropy and rotational invariance at the expense of increased memory and computational requirements [9]. The Altair’s UltraFluidX (UFX) solver, used for numerical analysis in this research, employs the D3Q27 velocity set, illustrated in Figure 2.3.

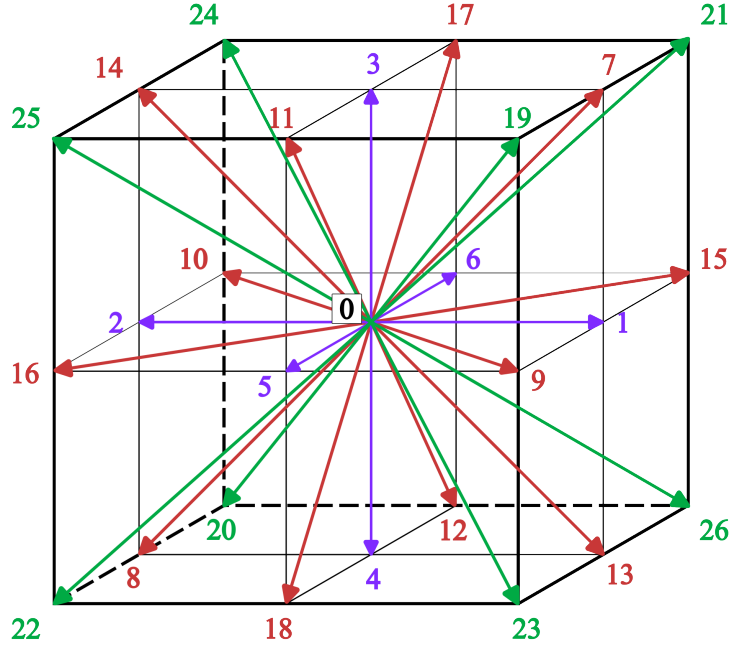


**Figure 2.3:** Three-dimensional D3Q27 velocity set comprising one zero velocity at the center (rest particles) and 26 non-zero discrete velocities. The velocity vectors connect the central lattice node to its nearest neighbors (six vectors, purple arrows), next-nearest neighbors (twelve vectors, red arrows), and diagonal neighbors (eight vectors, green arrows), providing enhanced isotropy and rotational invariance compared to lower-order velocity sets.

The D3Q27 velocity set offers superior numerical stability and significantly reduces anisotropy errors compared to lower-order alternatives, such as D3Q15 or D3Q19 [34]. The enhanced isotropy is particularly beneficial for applications involving complex geometries or rotating flows, where directional bias can significantly affect solution accuracy [36]. Previous studies have demonstrated the robustness of the D3Q27 velocity set for modeling medium and high Reynolds number flows [34–36]. Consequently, the D3Q27 velocity set is expected to provide higher accuracy than other popular alternatives, such as D2Q9, D3Q15, and D3Q19, albeit at an increased computational cost.

Following discretization, the lattice Boltzmann equation is expressed as:

$$f_i(\mathbf{x} + \mathbf{c}_i \Delta t, t + \Delta t) = f_i(\mathbf{x}, t) + \Omega_i(\mathbf{x}, t) \quad (2.4)$$

Equation 2.4 describes the evolution of particle populations with discrete velocity  $\mathbf{c}_i$  from the current lattice node  $\mathbf{x}$  to the neighboring node  $(\mathbf{x} + \mathbf{c}_i \Delta t)$  during the time step  $\Delta t$ . The collision operator  $\Omega_i(\mathbf{x}, t)$  represents the change in particle populations due to intermolecular collisions during each time step. The lattice Boltzmann equation can be conceptually divided into two distinct phases executed sequentially: collision (relaxation) and streaming (propagation), as illustrated in Figure 2.4.

During the collision step, particles interact locally at each lattice node, resulting in the redistribution of particle populations according to the collision operator (left to middle panel of Figure 2.4). Subsequently, during the streaming step, the post-collision particle populations propagate to neighboring nodes according to their respective discrete velocities (middle to right panel of Figure 2.4).

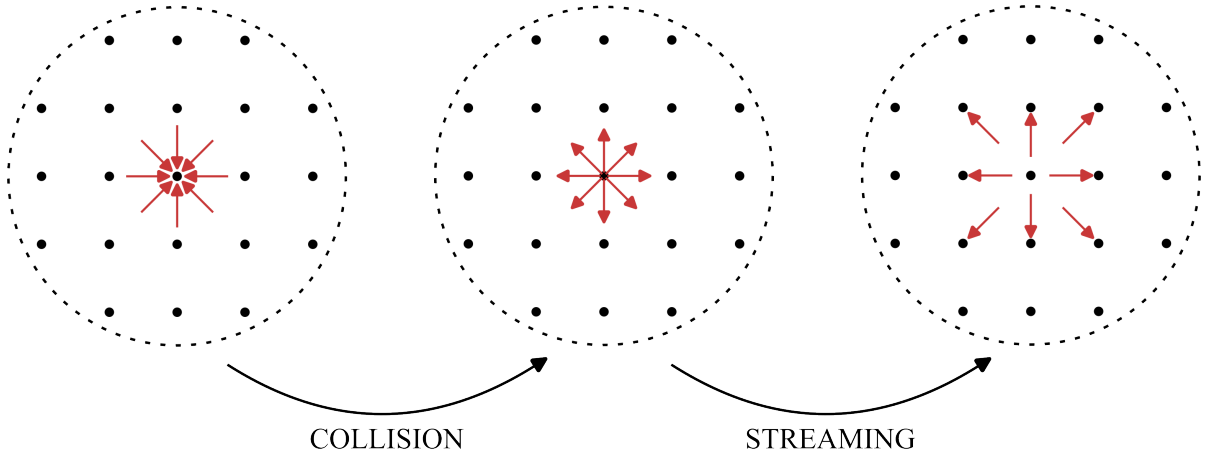


**Figure 2.4:** Collision-streaming algorithm in the LBM showing initial particle populations (left), post-collision redistribution (middle), and streaming to neighboring nodes (right).

Figure 2.4 illustrates the fundamental two-step algorithm that drives the LBM. In the initial state (left panel), particles are distributed among discrete velocity directions at each lattice node, represented by the red arrows radiating from the central node. During the collision step (middle panel), these particle populations undergo local redistribution according to the collision operator, which models the local interactions and drives the system toward equilibrium. The arrows show how the particle populations are reoriented and redistributed among the available discrete velocity directions. Finally, in the streaming step (right panel), the post-collision particle populations propagate simultaneously to their neighboring nodes along their respective

discrete velocity vectors. This streaming process represents the advective transport of particles through the lattice. The combination of these collision and streaming operations, performed iteratively across all lattice nodes, enables the LBM to solve fluid flow problems by evolving the particle distribution functions in both velocity and physical space.

The form and complexity of the collision operator  $\Omega_i(\mathbf{x}, t)$  significantly influence the numerical properties of the LBM algorithm, including stability, accuracy, and computational efficiency [86]. The choice of collision operator represents one of the most active areas of LBM research, with various formulations offering different balances between simplicity, accuracy, and stability [2].

The UFX solver implements the high-fidelity cumulant collision operator, which exhibits exceptionally low numerical diffusion and enhanced stability properties [22, 23, 87–89]. The cumulant collision operator represents a significant advancement over traditional approaches by working directly with cumulants of the distribution function, which are Galilean invariant quantities that naturally separate equilibrium and non-equilibrium contributions [22]. The cumulant operator is more recent, highly accurate, and computationally more complex than simpler alternatives such as the Bhatnagar-Gross-Krook (BGK) operator [90–96].

For turbulent flow simulation, LBM can employ a hybrid approach that incorporates the Large Eddy Simulation (LES) [5, 97–99] through the inherent filtering effect of the lattice discretization. The lattice spacing acts as an implicit filter, with subgrid-scale turbulence modeled through appropriate subgrid-scale stress models [100–103]. The reason lies in the improved wall resolution achieved with conventional CFD methods compared to a pure mesoscopic LBM approach. Therefore, UFX applies the LES turbulence modeling framework with a Smagorinsky subgrid-scale model for closure [100]. Additionally, UFX employs generalized wall functions to handle turbulent boundary layers near solid surfaces [99, 104].

Boundary condition implementation in LBM differs fundamentally from traditional CFD methods due to the particle-based nature of the algorithm. The discrete particle populations require special treatment at boundaries where standard streaming cannot be applied. Boundary schemes in LBM are classified into two primary categories: link-wise and wet-node approaches, both of which are implemented in the UFX solver. Link-wise schemes are applied at solid boundaries, which correspond to the no-slip boundary conditions in the conventional CFD approaches. On the other hand, wet-node schemes are used at the inlet and outlet boundaries. The bounce-back method [105] is used for the link-wise boundary scheme [4], which means that

during particle propagation, the particles reflect to their original location with reversed velocity when they collide with a solid boundary [2, 106]. The bounce-back boundary condition naturally preserves mass conservation and provides second-order accuracy for curved boundaries when combined with appropriate interpolation schemes [105].

The LBM offers several fundamental advantages over traditional CFD methods, including inherent parallelization due to local operations, the natural handling of complex geometries through simple boundary conditions, and the automatic incorporation of kinetic effects. However, it also presents challenges, including memory requirements proportional to the number of discrete velocities and limitations in compressibility range due to the low Mach number assumption [2].

## 2.3 Numerical Setup and Computational Domain Configuration

The numerical domain is configured to replicate the dimensions of the wind tunnel test section ( $0.6 \text{ m} \times 0.305 \text{ m} \times 0.305 \text{ m}$ ), ensuring direct comparability between experimental and computational results. The NACA 0012 airfoil retains identical dimensions, with a chord length of  $0.15 \text{ m}$  and a span of  $0.3 \text{ m}$ , and is positioned within the test section exactly as in the experimental setup. Airfoil profile was constructed using coordinates obtained from Airfoil Tools [107], while the 3D wing model was created by importing and extruding the 2D airfoil profile in SolidWorks. This geometric consistency is crucial for validation studies, as it eliminates potential discrepancies arising from variations in blockage ratios or wall effects between the experimental and computational configurations.

Unlike conventional CFD approaches that employ body-fitted structured or unstructured grids, LBM utilizes a Cartesian voxel distribution throughout the computational domain. The voxel-based approach inherent to LBM offers significant advantages in terms of simplicity in grid generation, geometric flexibility, and computational efficiency, particularly for complex geometries [2]. Initially, the coarsest mesh size is defined, which represents the edge length of cubic volumetric elements, and is referred to as a voxel, as mentioned above. This parameter defines the coarsest resolution of the Cartesian grid, with finer local refinements achieved through refinement zones that must be powers of 2 relative to this base mesh size. Specifically, if the coarsest mesh size is  $1 \text{ m}$ , the first refinement level yields  $0.5 \text{ m}$ , the second yields  $0.25 \text{ m}$ ,



and so forth. This geometric progression ensures smooth transitions between refinement levels while maintaining computational efficiency and numerical stability. Based on these principles, the refinement zone distribution is established as visualized in Figure 2.5, with precise positioning and dimensions specified in Table 2.2. The configuration employs four nested refinement zones concentrating resolution around the airfoil and its immediate wake region.

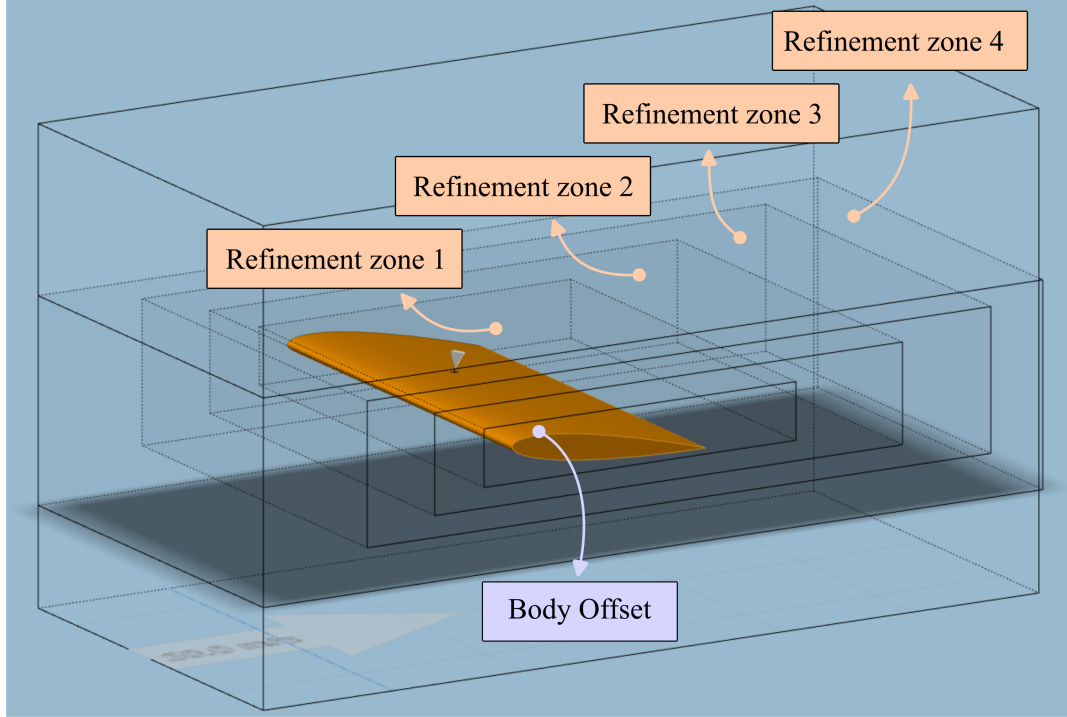


**Figure 2.5:** Computational domain configuration showing nested refinement zones (orange boxes with arrows) and body offset region (purple box with arrow).

**Table 2.2:** Refinement zone specifications including mesh sizes, spatial dimensions, and positioning coordinates, along with body offset parameters for near-wall resolution.

Mesh control type	Refinement level	Type	Offset Distance [m]
Body Offset	6	Distance	0.002
Mesh control type	Mesh size [m]	Dimensions (L x H x W) [m]	Position (X x Y x Z) [m]
Refinement Zone 1	0.001063	0.24 x 0.04 x 0.305	0.170 x 0.129 x 0.0
Refinement Zone 2	0.002125	0.36 x 0.07 x 0.305	0.132 x 0.115 x 0.0
Refinement Zone 3	0.00425	0.48 x 0.10 x 0.305	0.080 x 0.100 x 0.0
Refinement Zone 4	0.0085	0.60 x 0.16 x 0.305	0.000 x 0.070 x 0.0

Although the computational domain is initially defined to match the wind tunnel test section, the final domain dimensions differ slightly due to the requirements of UltraFluidX. The software mandates that domain dimensions in each direction must be multiples of four times the

coarsest mesh size to ensure proper load balancing and memory alignment for efficient parallel processing. Consequently, the domain is automatically enlarged in the positive  $x$ -direction, positive  $z$ -direction, and symmetrically in the  $y$ -direction when this requirement is not satisfied. In this study, the coarsest mesh size of 0.017 m results in adjusted domain dimensions of 0.612 m in the  $x$ -direction and 0.34 m in both  $y$ - and  $z$ -directions. The refinement zones are scaled proportionally with the domain adjustments. This minor enlargement actually provides a beneficial reduction in wall effects on the airfoil flow field, improving the simulation's representation of free-stream conditions. Overall, these changes introduce minimal impact on the comparative analysis while enhancing the physical accuracy of the simulation.

As illustrated in Figure 2.5, four distinct refinement zones are positioned around the airfoil (highlighted with orange arrows), while the purple arrow indicates the body offset. The body offset implements refinement level 6, corresponding to a mesh size of  $2.66 \cdot 10^{-4}$  m, with a distance of 0.002 m from the airfoil surface. This configuration provides sufficient resolution to capture the development of the boundary layer and near-wall flow phenomena. The body offset approach is analogous to near-wall refinement in traditional CFD, but it leverages LBM's wall function capabilities to maintain computational efficiency while ensuring an accurate boundary layer representation.

The mesh distribution is visualized comprehensively in Figure 2.6, where orange and purple arrows indicate regions of varying mesh density around the airfoil. Figure 2.6(a) and (b) present three-dimensional views of the complete and sectioned domains, respectively. Figure 2.6(c) displays the two-dimensional mesh distribution across the mid-plane, while Figure 2.6(d) provides a detailed view of the refined zones surrounding the airfoil.

UltraFluidX automatically generates transitional refinement layers between user-defined zones to ensure smooth gradients and numerical stability. These intermediate layers prevent abrupt mesh size changes that could introduce spurious numerical artifacts. In this configuration, an additional refinement zone 5 is visible in Figure 2.6(d), representing such an automatically generated transitional layer. The mesh is progressively refined toward the airfoil, ensuring higher flow resolution in smaller voxels where complex physics occur.

Additionally, a one-way coupling with Generalized Wall Functions (GWF) is applied near the airfoil surface [108], with the slip velocity factor set to 0.5. This approach numerically enforces a thinner effective boundary layer representation while providing enhanced stability and reduced oscillatory behavior compared to fully resolved boundary layer simulations. The wall

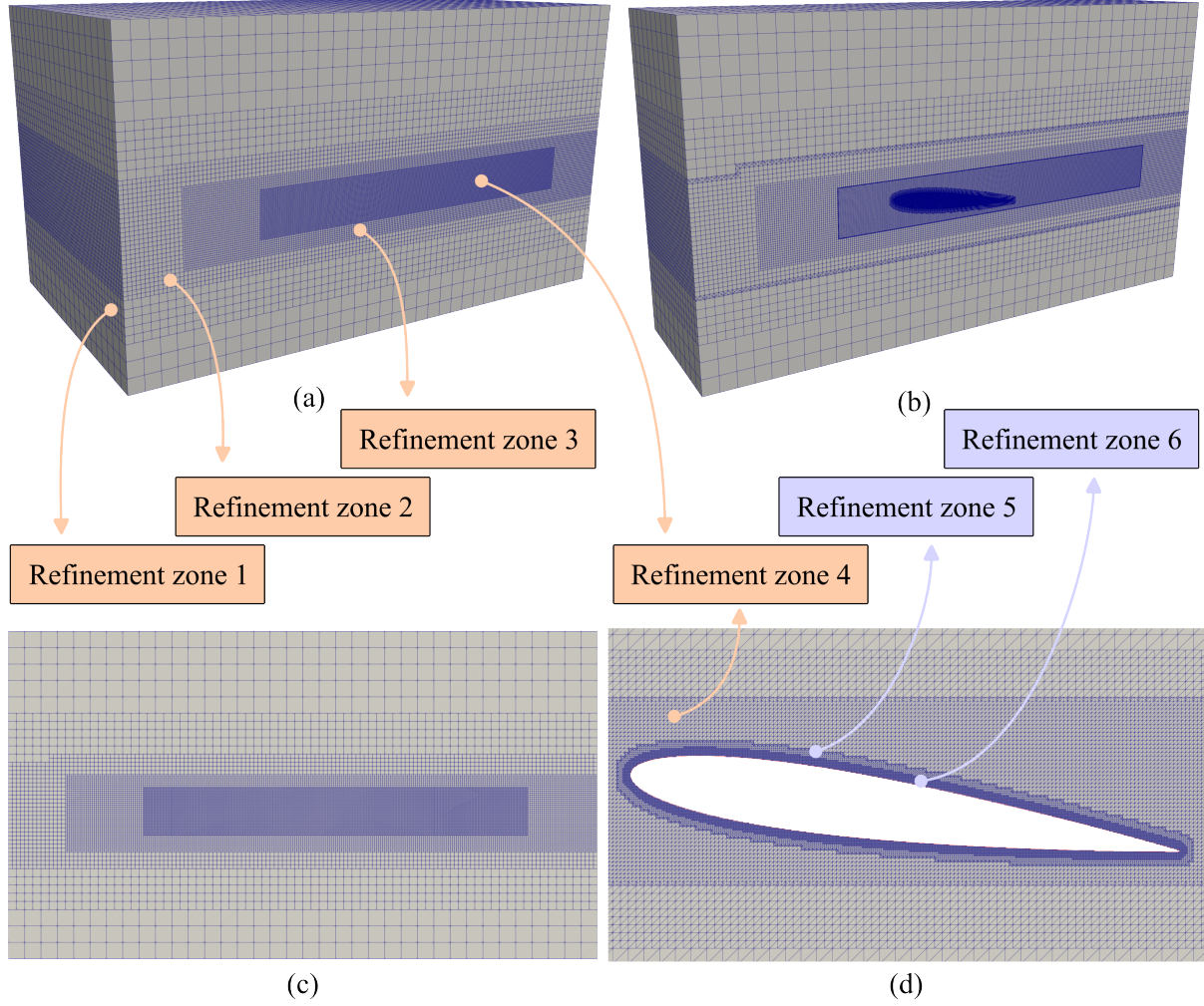


**Figure 2.6:** Computational mesh distribution around the NACA 0012 airfoil showing the hierarchical refinement strategy: (a) complete three-dimensional domain, (b) sectioned three-dimensional view, (c) two-dimensional mid-plane cross-section, and (d) detailed view of near-airfoil refinement zones.

function approach represents a practical compromise between computational cost and physical accuracy for engineering applications.

To complete the numerical setup, fluid properties are defined to match the experimental conditions precisely. The working fluid is air with a temperature of 27°C and an inlet velocity of 20 m/s. Based on the specified temperature, the density is 1.175 kg/m<sup>3</sup> and the dynamic viscosity is  $1.846 \cdot 10^{-5}$  Pa·s. The specific gas constant is 287.058 J/(kg·K), which, combined with the specific heat ratio  $\gamma = 1.4$ , yields a speed of sound of 347.31 m/s according to  $c = \sqrt{\gamma \cdot R \cdot T}$ . These thermodynamic properties correspond to standard atmospheric conditions with slight temperature elevation, ensuring consistency with experimental conditions. Consequently, the Mach number, calculated as  $Ma = v_{in}/c$ , yields 0.0576, where  $v_{in}$  represents the velocity at the inlet

surface, which confirms highly incompressible flow conditions where compressibility effects remain negligible. This low Mach number validates the usage of LBM for incompressible flow, with its limitations up to the Mach number of 0.4. The Reynolds number, determined from  $Re = (\rho \cdot v_{in} \cdot L_C) / \mu$ , equals approximately 191,000, where  $L_C$  is the wing's chord length, which matches the experimental target value.

The temporal discretization is intrinsically linked to the spatial mesh through the Courant-Friedrichs-Lewy (CFL) stability condition. In UltraFluidX, the time step is calculated using Equation 2.5, which represents a modified CFL formulation expressed as a Mach scaling factor with a default value of one:

$$\delta t = \frac{\Delta x_{coar} \cdot M_{sf}}{\sqrt{3} \cdot c} \quad (2.5)$$

where  $\Delta x_{coar}$  represents coarsest mesh size, while  $M_{sf}$  stands for the Mach scaling factor. The factor  $\sqrt{3}$  accounts for the three-dimensional nature of the lattice, ensuring stability in the most restrictive direction. The Mach scaling factor provides flexibility to adjust the effective CFL number for convergence acceleration or enhanced stability, though it was maintained at unity throughout this study.

For the physical simulation time ( $t_{pt}$ ), UltraFluidX recommends a duration sufficient for multiple flow-through times over the object of interest. The proposed calculation is  $t_{pt} = (30 \cdot L_C) / v_{in}$ , yielding 0.225 s. This duration ensures that transient startup effects dissipate and the flow field reaches a quasi-steady state, suitable for meaningful comparisons of force and pressure coefficients. However, to provide an additional safety margin for numerical stability and convergence, the final simulation time is extended to 0.3 s and is maintained for all simulations with different AoA, as revealed in Section 2.6. The number of iterations required to achieve the specified physical time is calculated as  $N = t_{pt} / \delta t$ , where  $N$  represents the total iteration count.

Regarding output parameters, the simulation captures various flow variables, including pressure scalars, velocity vectors, wall shear stress distributions, and surface normal vectors. UltraFluidX offers an efficient time-averaging capability where variables are averaged internally at each time step, providing superior accuracy and computational efficiency for post-processing. This internal averaging approach proves particularly advantageous for surface quantities around the airfoil, where the refinement level 6 corresponds to a mesh size of  $2.66 \cdot 10^{-4}$  m, resulting in an extremely small time step of  $4.422 \cdot 10^{-7}$  s.

For comparison purposes, the time step gathered at the coarsest mesh size gives the value of  $2.826 \cdot 10^{-5}$  s, which is 64 times larger than the finest time step. The internal averaging approach, therefore, captures higher-frequency fluctuations that would otherwise be aliased or missed in coarser temporal sampling. For the subsequent validation analysis in Section 2.6, pressure coefficient distributions are computed using pressure values averaged over the final 10% of the simulation duration, ensuring statistical convergence while eliminating transient startup effects.

## 2.4 Mesh Sensitivity Assessment

Grid sensitivity analysis is conducted for four different mesh configurations, ranging from coarsest to finest resolution. These configurations differ in terms of total voxel count and individual coarsest mesh size ratios, as visualized in Figure 2.7. Grid independence studies are fundamental to CFD validation, ensuring that numerical solutions converge to grid-independent values as mesh resolution increases. The objective is to demonstrate that further mesh refinement does not significantly alter the solution, thereby establishing confidence in the numerical accuracy of the results. The exponential growth in voxel count, evident from the trend line in Figure 2.7, illustrates the computational cost scaling associated with three-dimensional mesh refinement.

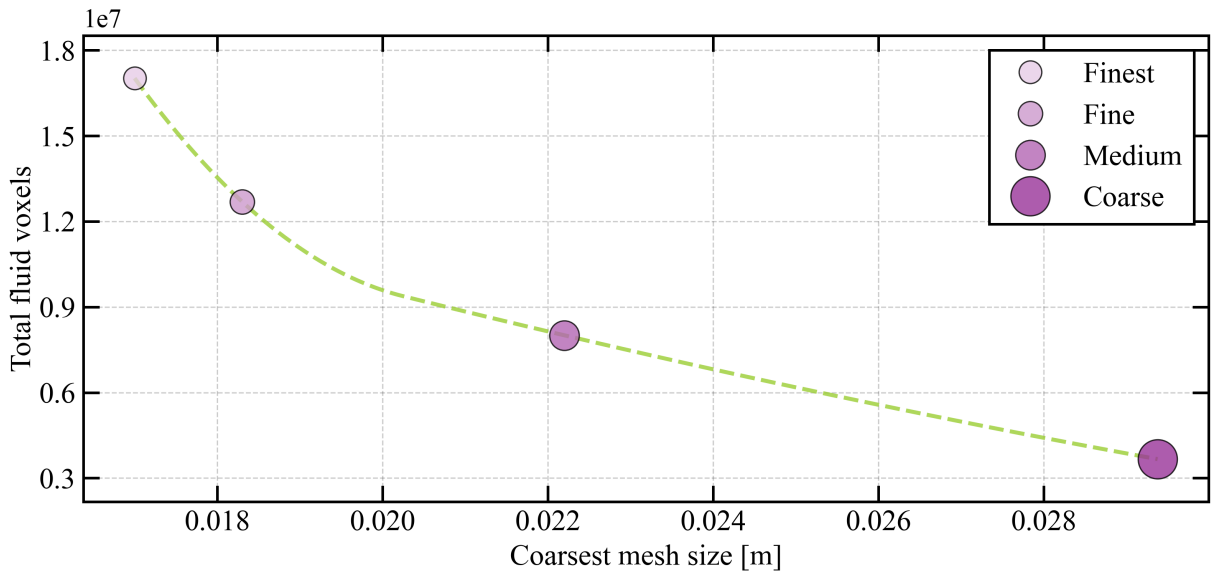


**Figure 2.7:** Exponential voxel growth with decreasing coarsest mesh size, shown by the yellow-green trend line. Purple circles represent mesh configurations (Coarse, Medium, Fine, Finest), with marker size proportional to the coarsest mesh dimension.

In this study, pressure coefficient and velocity distributions are evaluated and compared across cases with varying mesh densities. Figure 2.8(a) and (b) present pressure coefficient distributions over the normalized chord length for different mesh configurations on the airfoil's upper and lower surfaces, respectively.

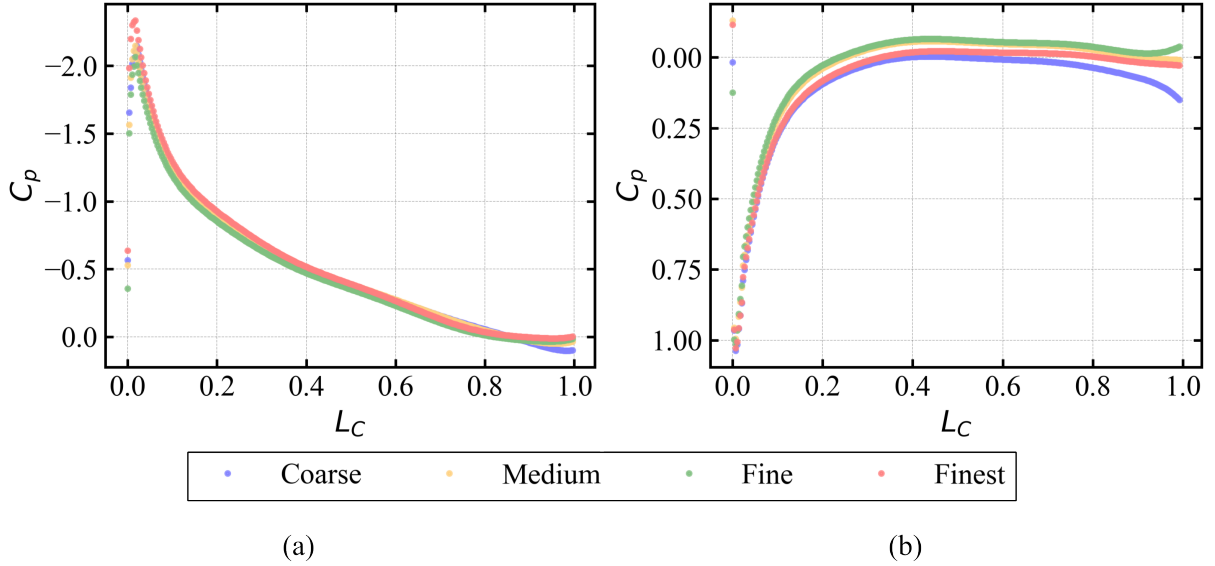


**Figure 2.8:** Pressure coefficient distribution along the normalized chord length for four mesh configurations: (a) upper surface showing excellent convergence except near the leading edge, where the finest mesh captures enhanced suction peaks, and (b) lower surface demonstrating consistent behavior across mesh refinements with trailing edge variations for the coarsest mesh.

Figure 2.8(a) demonstrates relative equivalence between results for different grids, with noticeable deviation occurring near the trailing edge for the coarsest mesh. The trailing edge region is particularly sensitive to mesh resolution due to the sharp geometric discontinuity and the associated pressure recovery, which requires adequate spatial resolution to capture accurately. A similar trend is exhibited in Figure 2.8(b), where the correlation between meshes is satisfactory except for the coarse mesh near the trailing edge. At the leading edge (Figure 2.8(a)), the finest mesh achieves the lowest  $C_p$  values compared to the other three cases, indicating enhanced capture of the suction peak. This behavior is expected as finer meshes better resolve the sharp pressure gradients associated with flow acceleration around curved surfaces, particularly the leading edge region where geometric curvature is maximum. At other locations on the upper surface, the data correlate well between cases.

Beyond the visual assessment provided in Figure 2.8, quantitative analysis of pressure coefficient extrema is presented in Table 2.3. For all four cases, the total number of fluid voxels,

maximum, and minimum pressure coefficients are documented. According to Bernoulli's equation for incompressible flow, the maximum pressure coefficient should theoretically approach unity at stagnation points where the flow velocity approaches zero, as mentioned in Section 2.1. Based on this theoretical foundation, the coarse mesh exhibits a relative error of 3.68%, while the other three cases maintain numerical errors below 3%, demonstrating improved accuracy with mesh refinement.

**Table 2.3:** Mesh configuration summary showing total fluid voxels and pressure coefficient extrema for mesh assessment.

Mesh type case	Total fluid voxels [ $\cdot 10^5$ ]	Max $C_p$	Min $C_p$
Coarse	3.66	1.037	-2.121
Medium	8.01	0.995	-2.130
Fine	12.69	1.014	-2.037
Finest	17.02	1.028	-2.324

To extend the comparison beyond visual assessment and pressure coefficient extrema, a statistical analysis methodology is implemented. Root Mean Square Error (RMSE) is employed for quantitative comparison between predicted values from different mesh configurations. RMSE provides a measure of the average magnitude of differences between mesh solutions, with lower values indicating better convergence. This statistical approach complements visual inspection by providing objective convergence metrics. The results are presented in Table 2.4, where RMSE is calculated using:

$$\text{RMSE}_{C_p} = \sqrt{\frac{1}{n} \sum_{i=1}^n [(C_p)_{\text{mesh1},i} - (C_p)_{\text{mesh2},i}]^2} \quad (2.6)$$

where  $n$  represents the number of comparison points along the airfoil surface, and the subscripts denote different mesh configurations.

**Table 2.4:** RMSE analysis of pressure coefficient distributions between different meshes for both airfoil surfaces.

Mesh type case	RMSE $_{C_p}$ Lower surface	RMSE $_{C_p}$ Upper surface
Coarse-Medium	0.0627	0.0187
Medium-Fine	0.0202	0.0494
Fine-Finest	0.0488	0.0843

The lower surface RMSE exhibits the highest value for the coarse-medium comparison due to inconsistent trailing edge representation visible in Figure 2.8(b). This behavior is typical in CFD validation studies, where coarse meshes fail to adequately resolve flow features in regions of high gradient, resulting in larger solution differences when compared to refined meshes. Regarding the upper surface, coarse, medium, and fine meshes demonstrate solid correlation. However, a larger divergence appears between fine and finest meshes for two primary reasons. First, the fine mesh underpredicts  $C_p$  values compared to medium and finest meshes, contributing to higher differences. The RMSE of 0.0351 between medium and finest mesh cases supports this observation. Second, the finest mesh captures enhanced  $C_p$  values around the leading edge due to significantly denser voxel distribution on the airfoil surface. Overall, the results demonstrate good congruence, with minimal variation, thereby establishing grid consistency for pressure coefficient analysis.

Velocity distribution assessment is conducted by evaluating velocity magnitude profiles at the centerline of several  $yz$ -plane cross-sections. The obtained profiles and corresponding locations are presented in Figure 2.9. The upper panel represents a clipped segment of the computational domain extending from  $x = 0.177$  m to  $0.36$  m in the streamwise direction and  $y = 0.129$  m to  $0.169$  m in the vertical direction. The domain contains the airfoil at an  $8^\circ$  angle of attack, with contours colored by velocity magnitude values. Black dashed lines on the contours emphasize centerline regions where velocity magnitudes are extracted for the four graphs in the lower panel.

Profiles for sections  $Dx_1$  and  $Dx_2$  indicate that upstream of the airfoil, velocity values for different grids remain consistent due to uniform inflow conditions. This upstream consistency is expected since the free-stream region contains minimal flow gradients, making it less sensitive to mesh resolution. The second profile ( $Dx_2$ ) additionally reveals small deviations in the coarsest mesh near the leading edge region.

Conversely, values in the wake region ( $Dx_3$  and  $Dx_4$ ) exhibit fluctuations as velocity decreases due to viscous effects and wake development. The wake region presents particular challenges for mesh independence studies due to the presence of unsteady vortical structures, velocity deficits, and enhanced turbulent mixing, all of which require adequate spatial resolution to be accurately captured. These differences, particularly the larger deviations from the coarsest mesh, result directly from insufficient mesh density in this region, leading to inadequate capture of complex flow structures. Nevertheless, the similar profile shapes obtained with medium, fine,



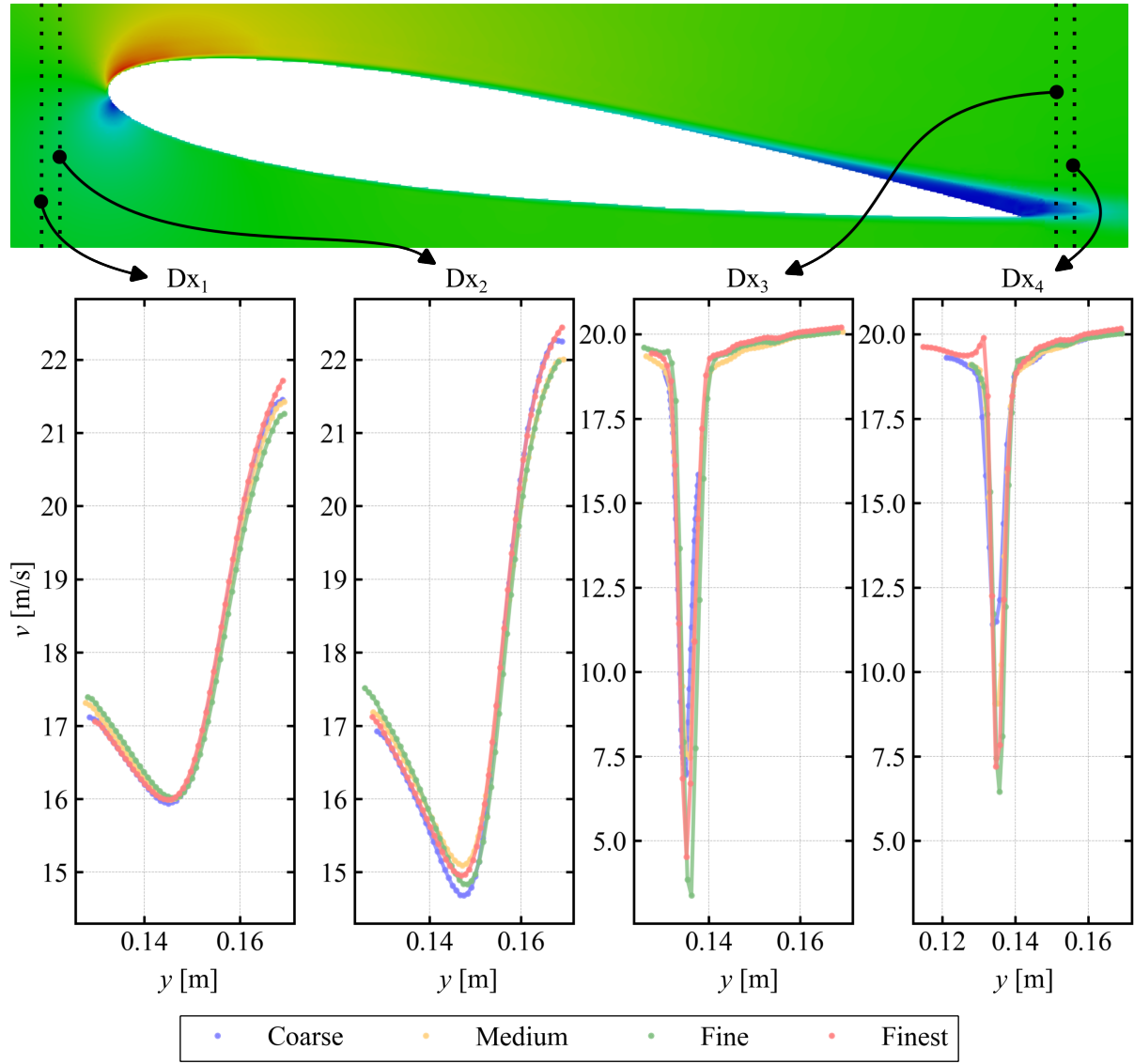


**Figure 2.9:** Velocity magnitude profiles extracted at  $yz$ -plane cross-sections for  $8^\circ$  angle of attack across different mesh configurations. Cross-sections  $Dx_1$  through  $Dx_4$  are located at  $x = 0.182$  m,  $0.185$  m,  $0.348$  m, and  $0.351$  m, respectively. Profiles represent time-averaged velocity magnitude over the final 10% of simulation duration, demonstrating mesh independence in upstream regions and convergence behavior in the complex wake region.

and finest meshes indicate satisfactory mesh independence quality, even in the turbulent wake region where velocity minima occur.

The choice of  $8^\circ$  angle of attack for the grid sensitivity study is strategic, as this represents the highest incidence angle investigated in this chapter and therefore exhibits the most complex flow physics. Due to the higher turbulence level associated with larger angles of attack, this case serves as a conservative benchmark for other cases. Therefore, the mesh assessment with the chosen finest mesh configuration should be applicable to the remaining three angles of attack.

Based on the comprehensive assessment, several conclusions emerge. The coarse mesh

proves inadequate near the leading and trailing edge regions and should be avoided for accurate predictions. The remaining grid configurations are suitable and yield consistent results for both pressure coefficients and velocity distributions. To minimize potential mesh-associated errors and ensure adequate resolution of all relevant flow scales, the finest grid is selected for subsequent analyses. The demonstrated grid convergence provides the foundation for reliable numerical predictions and validates the computational setup for subsequent validation against experimental data.

## 2.5 Experimental results

Experimental measurement results have been analyzed and evaluated using Python data processing routines. Experimental data processing in aerodynamics requires careful consideration of measurement uncertainties, systematic errors, and statistical analysis to ensure reliable and reproducible results [109]. Experimental data are presented via the pressure coefficient, which has been calculated according to Equation 2.1 defined in Section 2.1. This equation incorporates static pressure, stagnation pressure, and reference pressure and can be further expressed as Equation 2.7:

$$C_p = \frac{p_{st} - p_{ref}}{p_{stag} - p_{ref}} = \frac{p_{rel}}{p_{dyn}} \quad (2.7)$$

where  $p_{ref}$  represents the reference free-stream static pressure within the test section, while  $p_{rel}$  denotes relative pressure as the difference between static ( $p_{st}$ ) and free-stream pressure. Additionally,  $p_{dyn}$  represents dynamic pressure as the difference between stagnation ( $p_{stag}$ ) and reference pressure. The use of  $C_p$  enables a clear representation of the relative pressure distribution around the airfoil. The maximum value that  $C_p$  can achieve is unity ( $C_p = 1$ ), which occurs when static pressure equals stagnation pressure ( $p_{st} = p_{stag}$ ), corresponding to stagnation conditions where the fluid velocity approaches zero. This theoretical maximum is derived from the isentropic stagnation relations and represents the ideal pressure recovery at a stagnation point [82]. If  $p_{st} = p_{ref}$ , then the pressure coefficient equals zero ( $C_p = 0$ ), indicating undisturbed free-stream conditions.

When plotting pressure coefficient distributions, the abscissa typically represents the ratio of distance from the leading edge to the total chord length of the airfoil. This approach is consistently adopted in accordance with the methodology employed in Section 2.4. The pressure

coefficient distribution over normalized chord length for all four angles of attack is presented in Figure 2.10.

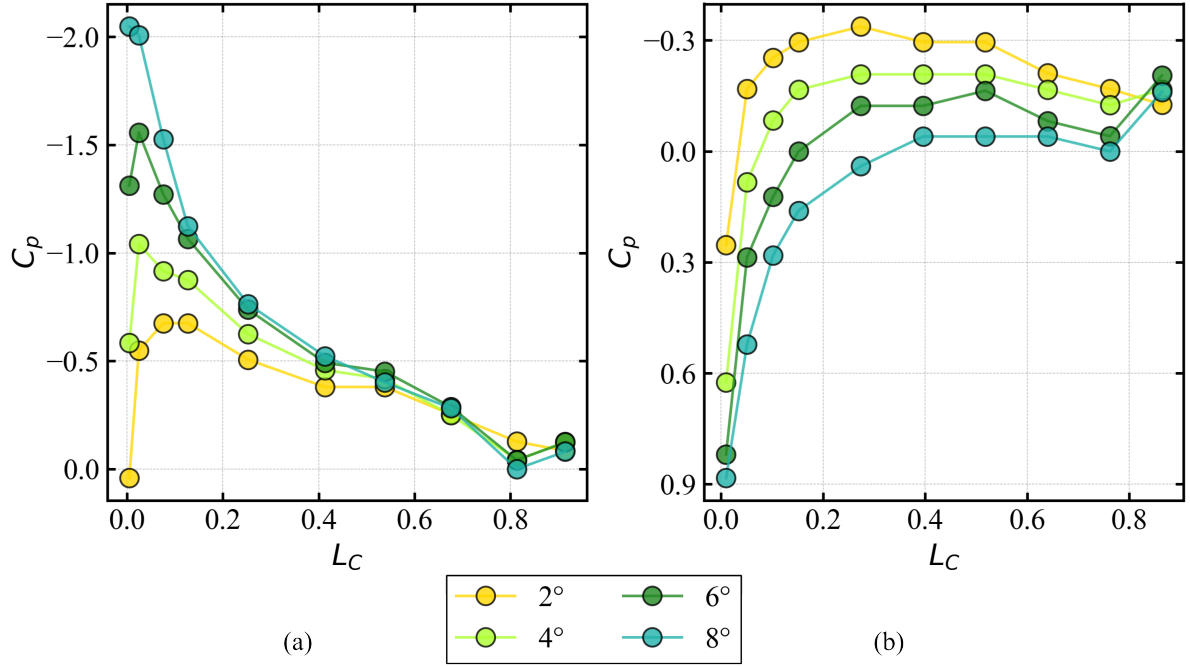


**Figure 2.10:** Wind tunnel measured pressure coefficient distributions at discrete tapping points over normalized chord length for four angles of attack: 2° (yellow), 4° (light green), 6° (forest green), and 8° (light sea green) for the airfoil's (a) upper surface and (b) lower surface.

Figure 2.10 demonstrates the expected asymptotic behavior of pressure coefficient values approaching the trailing edge region. However, there is a notable deviation at the trailing edge near  $L_c = 0.8$ , particularly pronounced for angles of attack of 8° and 6°, while being less obvious at 4° and negligible at 2°. This trailing edge behavior is characteristic of viscous flow separation and boundary layer thickening, which become more pronounced at higher angles of attack as the adverse pressure gradient strengthens [82].

Beyond physical flow phenomena, experimental factors may contribute to measurement variations. Measurement equipment inherently possesses finite accuracy, which can become more pronounced when overall pressure values are small, such as in the trailing edge region where pressure recovery occurs. Similarly, structural vibrations can influence measurements, particularly at higher flow speeds, since the airfoil experiences cantilever mounting conditions.

Experimental results do not reach the theoretical pressure coefficient maximum of unity due to the discrete tapping position limitations. The initial measurement tapping positions are located slightly downstream of the actual stagnation point. The stagnation point location is not fixed but migrates with changing angle of attack according to the relation  $x_{stag}/L_c \approx \sin(\alpha)$

for small angles, where  $\alpha$  represents the angle of attack [82]. Consequently, higher angle of attack values yield maximum  $C_p$  values closer to unity because the stagnation point moves downstream, approaching the first tapping position on the lower surface located 1.52 mm from the leading edge (Table 2.1).

Enhanced visualization of pressure coefficient extrema is provided through Figure 2.11, which illustrates the pressure field distribution around the airfoil for different angles of attack.

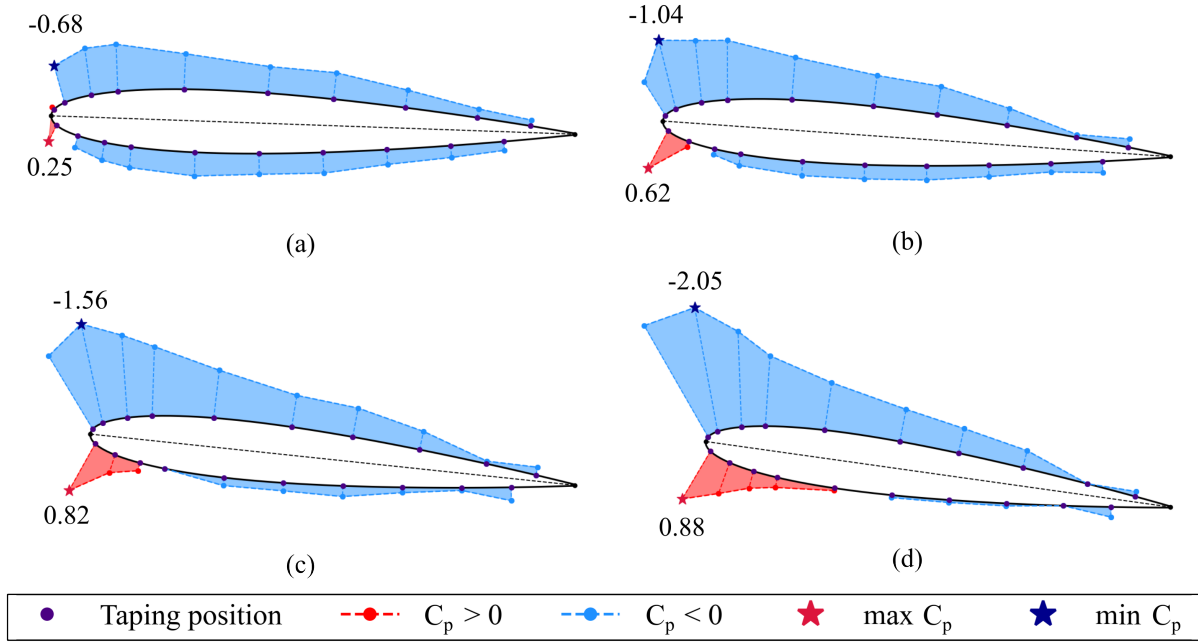


**Figure 2.11:** Pressure coefficient distribution visualization for the NACA 0012 airfoil at varying angles of attack: (a) 2°, (b) 4°, (c) 6°, and (d) 8°. High-pressure regions (red shading) indicate positive  $C_p$  values, while low-pressure regions (blue shading) represent negative  $C_p$  values. Purple circles denote tapping positions, with red and blue stars marking maximum and minimum  $C_p$  locations, respectively.

The progressive intensification of suction peaks with increasing angle of attack is clearly visible in Figure 2.11. This behavior reflects the fundamental mechanism of lift generation through asymmetric pressure distribution, where the net upward force results from the pressure difference between upper and lower surfaces.

Quantifying experimental uncertainty is crucial for establishing confidence intervals and enabling meaningful comparisons with computational results. The sources of uncertainty in wind tunnel pressure measurements include systematic errors from calibration drift, random errors from turbulence fluctuations, and environmental factors such as temperature and barometric pressure variations [109].

These deviations require statistical analysis to quantify their impact on measurement confidence. Measurement deviations can be quantified through statistical analysis of the pressure coefficient time series. As described in Section 2.1, experimental data were recorded over 300 seconds at 0.5-second intervals, yielding 600 individual measurements per tapping location. The pressure coefficient was calculated for each time step. From this time series, the standard deviation of pressure coefficient measurements is calculated using Equation 2.8:

$$\sigma = \sqrt{\frac{\sum_{i=1}^n (C_{p_i} - \overline{C_p})^2}{n}} \quad (2.8)$$

where  $\sigma$  represents the standard deviation,  $n$  is the number of measurements in the sample (600),  $C_{p_i}$  denotes the pressure coefficient for an individual measurement, and  $\overline{C_p}$  represents the time-averaged pressure coefficient. This statistical approach follows standard practices in experimental uncertainty analysis, providing a measure of measurement repeatability and the magnitude of random error [109]. The measurement uncertainties calculated for all experimental configurations (four different angles of attack) are illustrated in Figure 2.12, which shows pressure coefficient distributions with associated error bars.

The measurement uncertainties displayed in Figure 2.12 are relatively small, indicating acceptable measurement precision throughout the experimental campaign. Detailed numerical values are presented in Table 2.5, which summarizes the maximum standard deviations and their corresponding tapping positions for different angles of attack.

**Table 2.5:** Maximum pressure coefficient standard deviations for upper and lower surfaces with corresponding tapping position numbers for each angle of attack configuration.

Angle of attack	$\sigma_{max}$ upper surface	Tapping position	$\sigma_{max}$ lower surface	Tapping position
2°	0.0211	13	0.0207	16
4°	0.0328	3	0.0173	10
6°	0.0395	3	0.0331	2
8°	0.0479	1	0.0280	16

According to Table 2.5, the largest standard deviation for the upper surface occurs at 8° angle of attack at tapping position 1 (near the leading edge). Conversely, for the lower surface, the maximum deviation occurs at tapping position 2 for the 6° angle of attack case. The occurrence of peak uncertainties near leading and trailing edges aligns with expectations, as these regions experience the most complex flow phenomena and steepest pressure gradients.

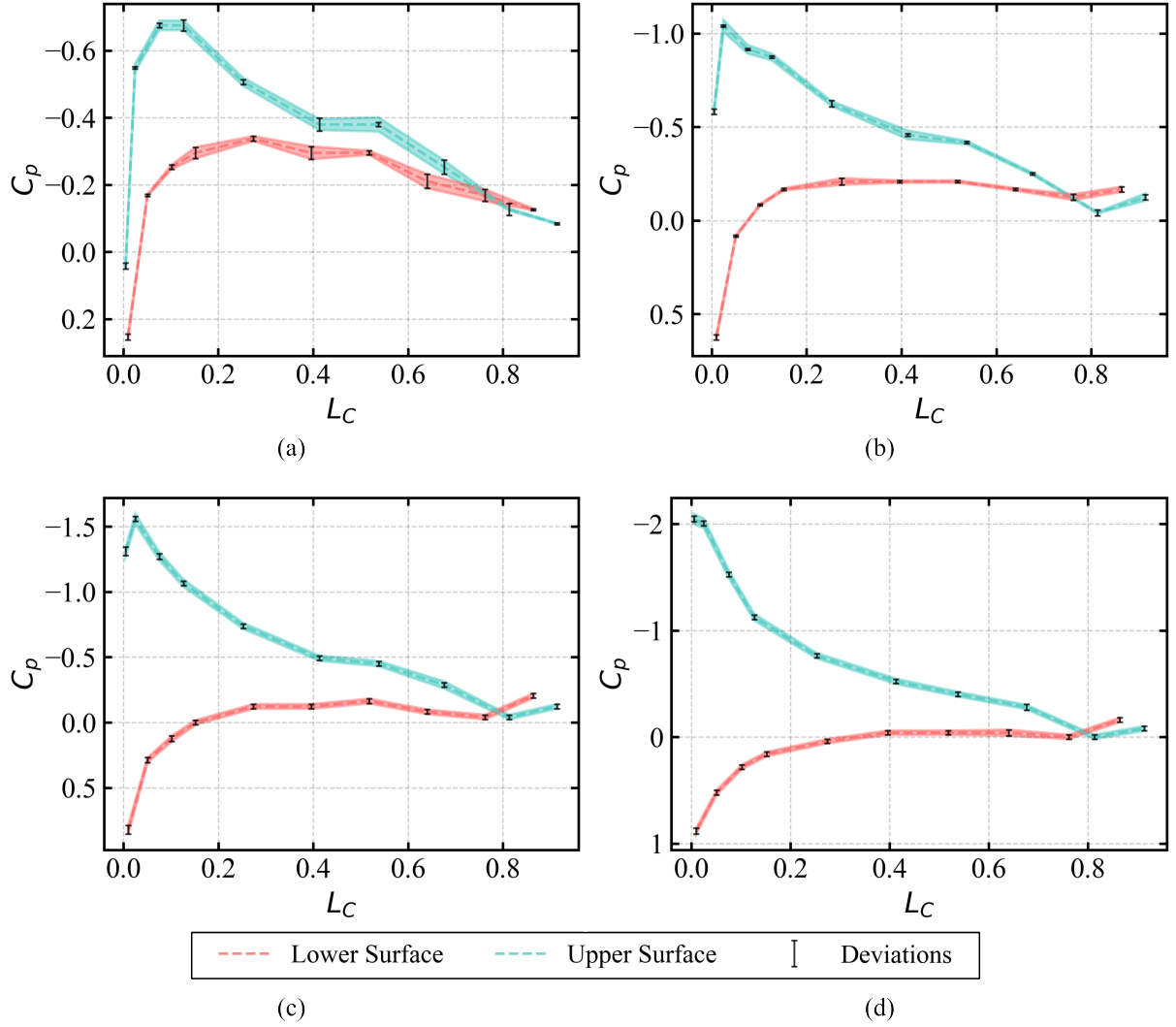


**Figure 2.12:** Experimental pressure coefficient distributions with measurement uncertainties (error bars) for lower surface (red) and upper surface (teal) at four angles of attack: (a)  $2^\circ$ , (b)  $4^\circ$ , (c)  $6^\circ$ , and (d)  $8^\circ$ . The error bars represent one standard deviation from the mean, providing confidence intervals for the experimental measurements.

All measurement uncertainties maintain standard deviations below 5%, which falls within acceptable limits for experimental aerodynamics according to established guidelines [109]. This level of precision enables confident comparison with numerical results and validates the experimental methodology for subsequent validation studies. Therefore, the time-averaged experimental results presented in this section provide a reliable benchmark for computational validation in Section 2.6.

## 2.6 LBM Validation Against Experimental Results

The numerical setup described in Section 2.3 is employed using the finest mesh configuration from Section 2.4 for all angle of attack test cases. Before conducting a quantitative comparison between numerical and experimental results, a comprehensive overview of the LBM flow field characteristics is presented.

As expected, the results presented in Figure 2.13 demonstrate that increasing the AoA produces correspondingly stronger pressure gradients around the airfoil. The pressure field clearly shows a distinct stagnation point at the leading edge, evidenced by the high-pressure region (red coloring) in Figures 2.13(a-d), where the flow decelerates to zero velocity, visible as blue regions in Figures 2.13(e-h). Moving along the airfoil surface, the favorable pressure gradient on the upper surface creates the characteristic low-pressure zone (blue-green regions) responsible for lift generation. The flow acceleration over the upper surface, indicated by higher velocity magnitudes (yellow-red regions) in Figure 2.13(e-h), demonstrates mass conservation principles and the conversion of pressure head to kinetic energy. This behavior directly validates Bernoulli's equation for incompressible flow, where  $p + \frac{1}{2}\rho V^2 = \text{constant}$  along streamlines, resulting in inverse correlation between pressure and velocity [82].

The red dashed line in the velocity magnitude panels of Figure 2.13 shows regions where blue coloring intensifies from the marked line toward the trailing edge across all four angle configurations. Since these represent time-averaged values to facilitate comparison with experimental data, transient phenomena are not pursued in detail within this chapter. Time averaging inherently filters out unsteady fluctuations and vortical structures, providing a statistical representation of the mean flow field that corresponds to the averaged experimental measurement conditions. Consequently, discrete vortices are not visible, although this does not preclude the existence of turbulent flow in regions such as the wake and boundary layer, particularly at higher angles of attack.

The observed low velocities and elevated pressures near the trailing edge suggest possible flow separation and laminar-to-turbulent boundary layer transition. These phenomena are characteristic of moderate Reynolds number flows where adverse pressure gradients can induce boundary layer separation and subsequent transition to turbulence [110]. More comprehensive analysis of these physical phenomena is presented in Chapters 3 and 4.

The stagnation point migration with increasing angle of attack is further emphasized in Figure 2.14, which demonstrates the downstream movement of the maximum pressure coefficient

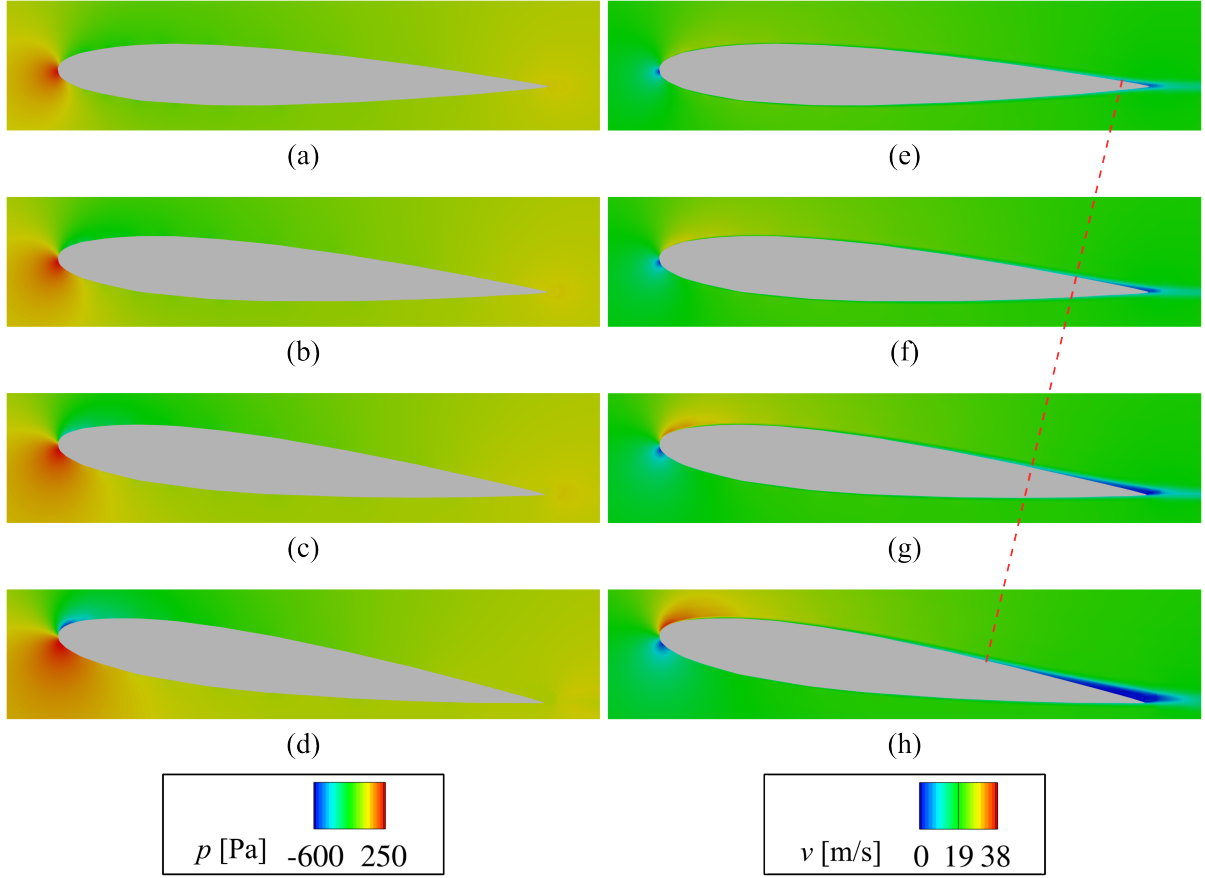


**Figure 2.13:** Time-averaged pressure (a-d) and velocity magnitude (e-h) contours at the mid-plane XY cross-section for angles of attack: (a,e)  $2^\circ$ , (b,f)  $4^\circ$ , (c,g)  $6^\circ$ , and (d,h)  $8^\circ$ . Averaging is performed over the final 10% of simulation time. The red dashed line is a demarcation of the boundary layer growth region.

location on the lower surface.

The magnified view within the purple rectangle clearly illustrates the downstream migration of  $C_{p,\max}$  with increasing angle of attack. This behavior explains the experimental limitation mentioned in Subsection 2.5 regarding the discrete tapping positions. Tapping position 2, located 1.52 mm from the leading edge, was unable to capture  $C_{p,\max}$  for lower angles of attack but approached this maximum as the angle increased. As already mentioned, the stagnation point location follows the approximate relation  $x_{\text{stag}}/L_c \approx \sin(\alpha)$  for small angles, where the stagnation point moves progressively downstream as the effective angle of attack increases [82]. Higher pressure coefficient values were obtained for steeper angles because  $C_{p,\max}$  approaches tapping position 2 at  $0.01013 L_c$  (1.52 mm) from the leading edge.

Besides CFD analysis alone, the primary objective of this validation study is to compare and assess LBM predictions against experimental wind tunnel data. Figure 2.15 presents a comprehensive comparison between LBM and experimental results for all four angle of attack



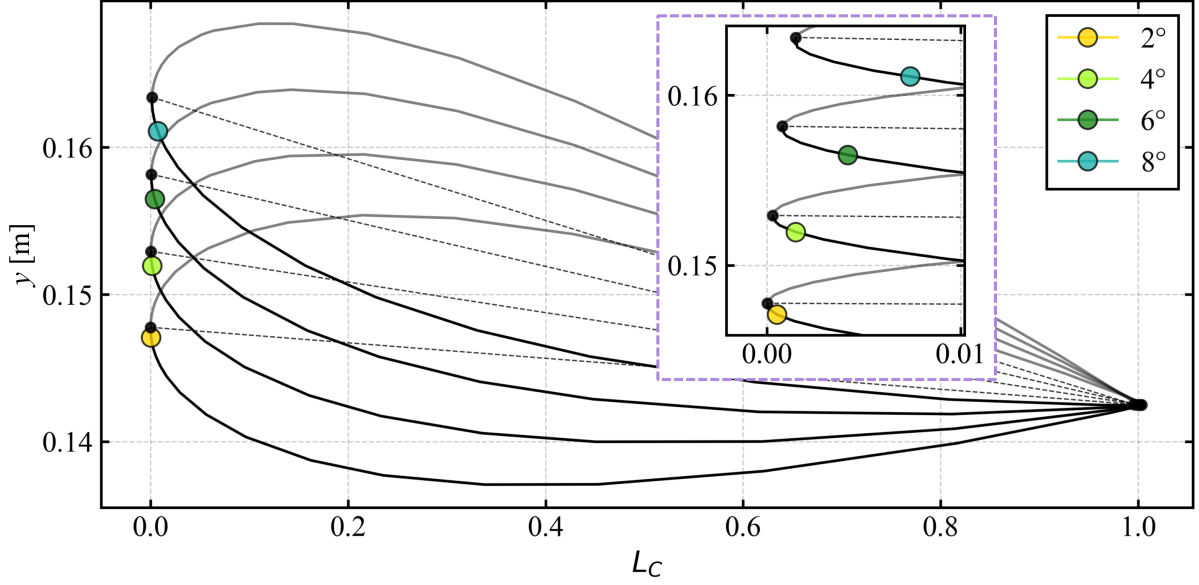


**Figure 2.14:** Stagnation point distribution for different angle of attack cases, with the magnified leading edge region highlighted by the purple rectangle. The lower surface is depicted in black, while the upper surface is shown in gray. Stagnation points circle markers are color-coded for different AoA: 2° (yellow), 4° (light green), 6° (forest green), and 8° (light sea green).

configurations.

At first examination, the correlation between numerical and experimental data appears satisfactory across all configurations. The relative error based on the theoretical maximum  $C_{p,\max} = 1$  for incompressible flow (Mach number well below 0.3) remains below 1.5% for all cases except the 8° angle of attack, where it reaches 2.8%. On the other hand, Figure 2.15(d) reveals excellent agreement for both surfaces at 8° angle of attack, besides the already mentioned minimum  $C_p$ . In comparison, for lower angles (Figures 2.15(a-c)), deviations become more pronounced approaching the trailing edge, particularly on the upper surface. Nevertheless, this level of accuracy validates the numerical methodology and confirms that the LBM-LES approach captures the essential physics of the flow field.

However, the systematic analysis reveals distinct characteristics of the flow regime. For the first 40% of the chord length from the leading edge, excellent agreement with minimal deviation from experimental results is maintained across all cases. In certain scenarios, such as the 6° angle of attack case (Figure 2.15(c)), minor deviations are visible in this region; however, the trends remain consistent, enabling the curves to overlap with minimal vertical displacement.

Interestingly, a notable pattern emerges around the mid-chord region, particularly on the upper surface. Experimental data show that the absolute values of the pressure coefficient suddenly increase, followed by decreases, at upper surface tapping positions 11, 13, and 15 (located

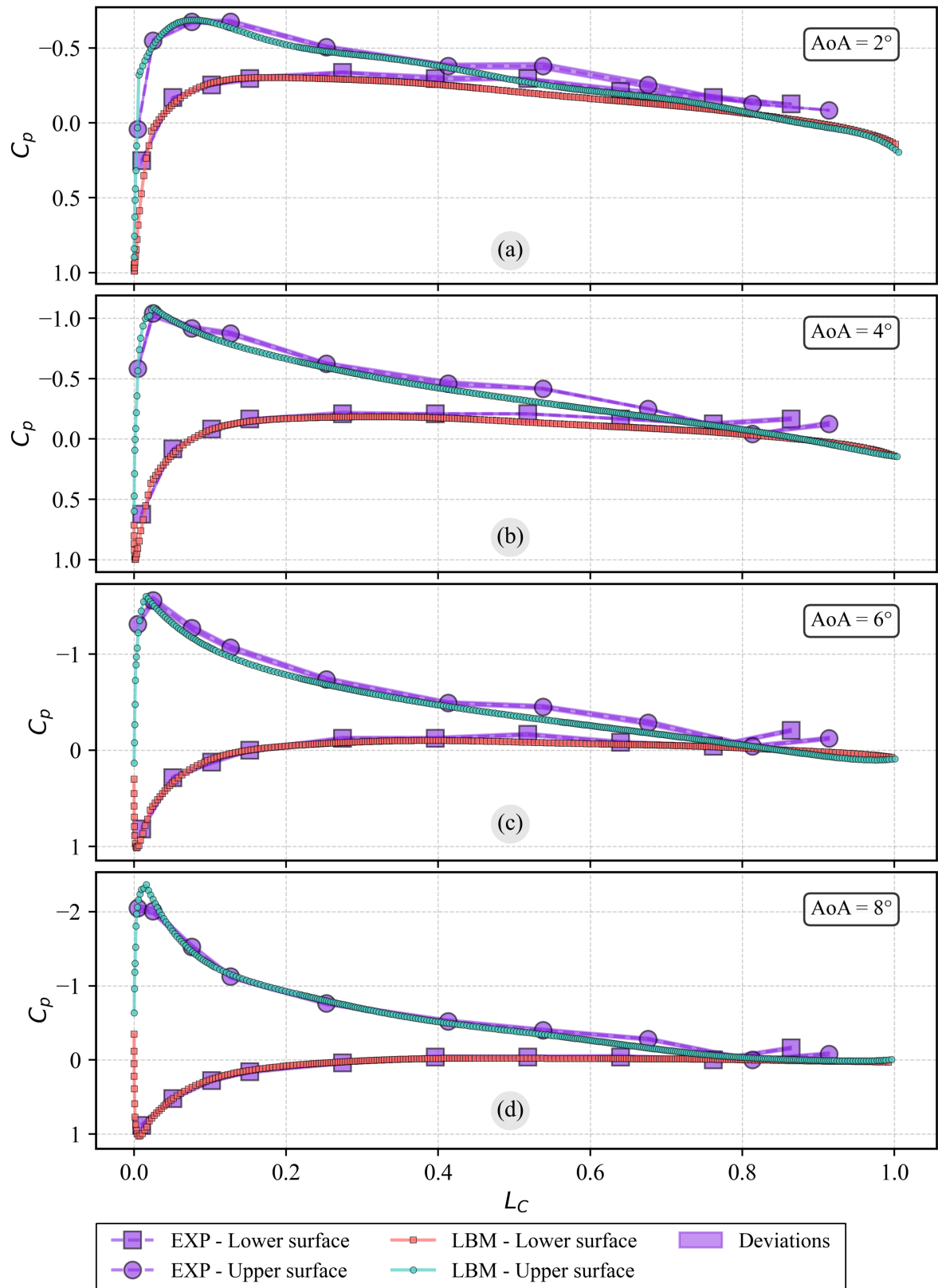


**Figure 2.15:** Pressure coefficient distributions comparing LBM results (red rectangles for lower surface, teal circles for upper surface) with experimental data (violet markers and dashed lines) around the NACA 0012 midplane surface. Semitransparent violet bands around the dashed lines represent experimental measurement uncertainties.

at 62 mm, 80.77 mm, and 101.35 mm, respectively). These pressure coefficient fluctuations are characteristic signatures of laminar separation bubble (LSB) formation, a well-documented phenomenon in moderate Reynolds number flows where laminar boundary layers separate due to adverse pressure gradients and subsequently reattach after transitioning to turbulence [82]. The stability characteristics of laminar separation bubbles are highly sensitive to the angle of attack and the Reynolds number. At lower angles, bubbles remain relatively stable, while at higher incidence angles, they become susceptible to "bursting"—a phenomenon where the bubble suddenly increases in length and becomes highly unsteady. This effect of AoA on LSB is nicely captured in Figures 2.15(a-d), where LSB is most prominent at lower angles of attack, while at 8°, the effect becomes less pronounced due to natural boundary layer destabilization. The LBM results demonstrate reasonable correlation with experimental trends in the aft portion of the airfoil but do not fully capture the detailed physics of laminar separation bubble dynamics.

Figure 2.16 provides a quantitative assessment through filled regions emphasizing differences between numerical and experimental results, using time-averaged experimental values without uncertainty bands.

Statistical validation metrics are presented in Table 2.6, where the coefficient of determination  $R^2$  is calculated according to Equation 2.9:

$$R^2 = 1 - \frac{\sum_{i=1}^n (y_i - \hat{y}_i)^2}{\sum_{i=1}^n (y_i - \bar{y})^2} \quad (2.9)$$

where  $y_i$  represents experimental data values,  $\hat{y}_i$  denotes LBM simulation results,  $\bar{y}$  is the mean of experimental values, and  $n$  symbolizes the number of comparison points. The  $R^2$  metric provides a normalized measure of how well the computational model explains the variance in experimental data, with values approaching unity indicating excellent agreement.

The 8° angle of attack case demonstrates best agreement with experimental data on the lower surface, surpassing all other configurations in terms of accuracy. Notably, excluding the first and last tapping positions on the lower surface (positions 2 and 20) would reduce the RMSE from 0.068 to 0.014, indicating that edge effects contribute significantly to the overall error. For the 6° AoA case, the most significant errors occur near the trailing edge (positions 19 and 20) and around the suspected LSB region, as illustrated in Figure 2.16(c). The 4° case exhibits similar deviations to the 6° AoA wing while maintaining excellent correlation elsewhere. The 2° angle of attack case exhibits the largest disagreement from mid-chord to trailing edge, which is confirmed as the least correlated result based on  $R^2$  metrics in Table 2.6.

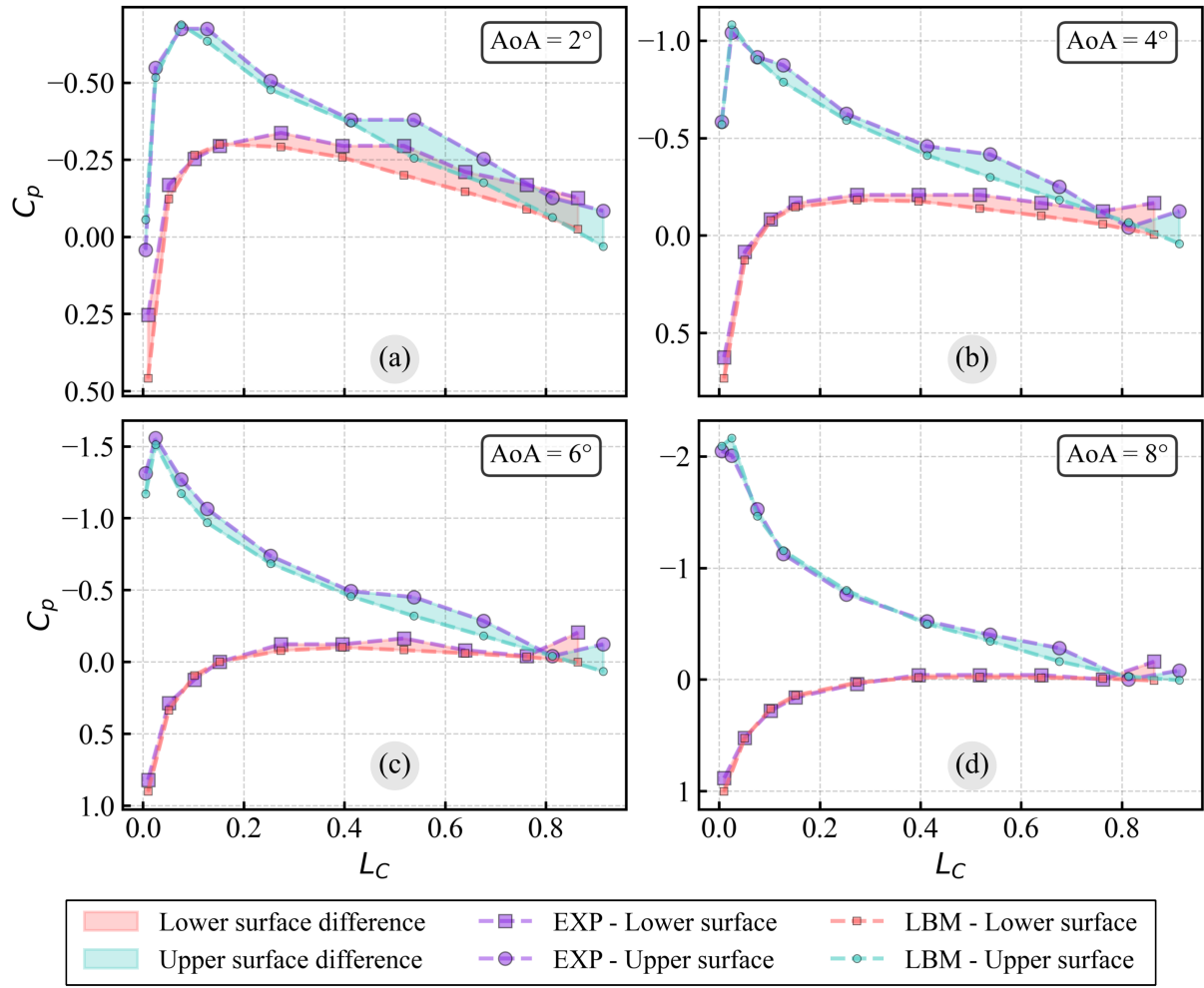


**Figure 2.16:** Comparison between experimental results (violet markers) and LBM predictions (red rectangles for lower surface, teal circles for upper surface). Semitransparent red and teal regions represent the magnitude of differences between computational and experimental data.

**Table 2.6:** Statistical validation metrics including Root Mean Square Error (RMSE) and coefficient of determination ( $R^2$ ) for different angles of attack, with separate RMSE values for upper and lower surfaces.

AoA (°)	RMSE Total	$R^2$ Total	RMSE Lower	RMSE Upper
2°	0.081	0.865	0.089	0.072
4°	0.076	0.958	0.075	0.077
6°	0.093	0.974	0.079	0.105
8°	0.073	0.991	0.068	0.077

The present validation at medium Reynolds number ( $Re = 191,000$ ) represents a significant advancement in assessing LBM capabilities for engineering applications. It demonstrates that LBM-LES implementation provides reliable results for moderate Reynolds number airfoil flows using Generalized Wall Functions, D3Q27 velocity set, and high-fidelity cumulant-based collision operators. Furthermore, the computational efficiency advantages are substantial: all

simulations were conducted using one Quadro M6000 GPU and one Intel CPU, with the finest mesh  $8^\circ$  angle of attack case requiring 23 hours, 34 minutes, and 17 seconds, a peak CPU memory consumption of 29.824 GB, and peak GPU memory usage of 9.522 GB. This performance represents a significant reduction in computational time compared to traditional high-fidelity CFD approaches, while maintaining comparable accuracy levels.

The demonstrated validation establishes confidence in the LBM methodology for subsequent analyses involving more complex flow phenomena, including bio-inspired airfoil configurations and unsteady flow dynamics addressed in Chapter 4.

# **3 LARGE EDDY SIMULATION ANALYSIS OF AERODYNAMICS AND AEROACOUSTICS IN THE SERRATED AIRFOIL**

This chapter presents a detailed numerical investigation of both primary and owl-inspired serrated trailing edge (STE) airfoils, focusing on a symmetric Joukowski airfoil with 12% thickness during the initial acceleration phase. The analysis employs a high-fidelity Large Eddy Simulation (LES) approach.

Section 3.1 outlines the methodological framework, including the numerical setup, software implementation, and hardware resources utilized for the LES computations. Section 3.2 describes the airfoil geometry and mesh generation, accompanied by a comprehensive grid sensitivity study and wall-unit grid spacing analysis. The numerical results are validated against the XFOIL [111] program for the Reynolds number of 250,000, Mach number of 0.25, and AoA of  $5^\circ$ .

Section 3.3 provides a detailed aerodynamic and aeroacoustic analysis of the primary trailing edge (PTE) airfoil, further divided into two subsections. Subsection 3.3.1 focuses on the aerodynamic efficiency of the PTE, while Subsection 3.3.2 investigates key regions on and around the airfoil that influence aerodynamic and aeroacoustic characteristics, including boundary layer transition and laminar separation bubble formation.

Section 3.4 presents a comparative analysis between the STE and PTE airfoils, utilizing data from the previous section. Finally, Section 3.5 extends the comparison to various Reynolds numbers from 100,000 to half a million, where more focus on aerodynamic forces and boundary layer transition is obtained through Subsection 3.5.1, while Subsection 3.5.2 conducts aeroacoustic analysis.

## **3.1 Computational Methodology and Numerical Framework**

As noted, the LES approach is employed to solve the fluid flow around the airfoil. The simulations are performed using CANARD (Compressible Aerodynamics & Aeroacoustics Research

code), an in-house, high-order, wavenumber-optimised DNS/LES solver developed at the University of Southampton. CANARD enables efficient and accurate simulations of compressible flows and sound waves on massively parallel supercomputers. The code has been extensively validated and has produced high-quality research outputs published in leading journals over the last five years [112–117].

In this study, four Reynolds numbers are considered, ranging from 100,000 up to 500,000, based on the chord length ( $L_c$ ) and the freestream velocity ( $U_\infty$ ) evaluated at the end of the acceleration phase (i.e., the onset of the post-acceleration phase at constant velocity). The final freestream Mach number is set to  $M_\infty = U_\infty/a_\infty = 0.25$ , and the angle of attack (AoA) is fixed at  $5^\circ$ . Here, the AoA is specified by adjusting the direction of the velocity vector, not by rotating the airfoil geometry; in all equations, the AoA is denoted by the Greek letter  $\alpha$ . The streamwise, vertical, and spanwise velocity components are defined as  $u_\infty = U_\infty \cos(\alpha)$ ,  $v_\infty = U_\infty \sin(\alpha)$ , and  $w_\infty = 0$ , respectively. Two coordinate systems are used throughout the analysis: a Cartesian system  $x_j = \{x, y, z\}$ , where the airfoil chord is aligned with the  $x$ -axis, and a generalized coordinate system  $\xi_i = \{\xi, \eta, \zeta\}$ , where the velocity streamlines are parallel to the  $\xi$ -axis. All other variables are non-dimensionalized, indicated by a superscript asterisk (e.g., non-dimensional force in the  $x$ -direction,  $f_x^*$ ).

In this work, the full three-dimensional compressible Navier–Stokes equations, including a source term for sponge layers, are solved in conservative form and transformed onto a generalized coordinate system, as shown in Eq. (3.1):

$$\frac{\partial}{\partial t} \left( \frac{\mathbf{Q}}{J} \right) + \frac{\partial}{\partial \xi_i} \left( \frac{\mathbf{E}_j}{J} \frac{\partial \xi_i}{\partial x_j} \right) = \frac{M_\infty}{Re_\infty} \frac{\partial}{\partial \xi_i} \left( \frac{\mathbf{F}_j}{J} \frac{\partial \xi_i}{\partial x_j} \right) - \frac{\mathbf{S}}{J}, \quad (3.1)$$

where  $i = 1, 2, 3$  and  $j = 1, 2, 3$ . The freestream velocity is defined as  $U_\infty = \sqrt{u_\infty^2 + v_\infty^2 + w_\infty^2}$ , and the Reynolds number is given by  $Re = \rho_\infty U_\infty L_c / \mu_\infty$ . The Mach number is  $M_\infty = U_\infty / a_\infty$ , where  $a_\infty = \sqrt{\gamma p_\infty / \rho_\infty}$  denotes the ambient speed of sound. All primary parameters are non-dimensionalized: the length scale by the airfoil chord  $L_c$ , the time scale by  $L_c / a_\infty$ , pressure by  $\rho_\infty a_\infty^2$ , and velocities by  $a_\infty$ . Similarly, temperature, density, and viscosity are normalized by their respective ambient values  $T_\infty$ ,  $\rho_\infty$ , and  $\mu_\infty$ .

The terms in Eq. (3.2) are defined as follows:

$$\begin{cases} \mathbf{Q} = [\rho, \rho u, \rho v, \rho w, \rho e_t]^T, \\ \mathbf{E}_j = [\rho u_j, (\rho u u_j + \delta_{1j} p), (\rho v u_j + \delta_{2j} p), (\rho w u_j + \delta_{3j} p), (\rho e_t + p) u_j]^T, \\ \mathbf{F}_j = [0, \tau_{1j}, \tau_{2j}, \tau_{3j}, u_i \tau_{ij} + q_i]^T, \\ \tau_{ij} = \mu \left( \frac{\partial u_i}{\partial x_j} + \frac{\partial u_j}{\partial x_i} - \frac{2}{3} \delta_{ij} \frac{\partial u_i}{\partial x_i} \right) \quad q_j = \frac{\mu}{(\gamma-1)Pr} \frac{\partial T}{\partial x_j}, \end{cases} \quad (3.2)$$

where the Jacobian determinant of the transformation from Cartesian to body-fitted coordinates is  $J^{-1} = |\partial(\xi, \eta, \zeta)/\partial(x, y, z)|$ . The vector  $\mathbf{Q}$  contains the conservative variables, with velocity components  $u_j = \{u, v, w\}$  and total energy  $e_t = p/[(\gamma-1)\rho] + u_j u_j/2$ . The Prandtl number is  $Pr = 0.71$ , and the heat capacity ratio is  $\gamma = 1.4$ . Convective, viscous, and heat fluxes are denoted by  $\mathbf{E}_j$ ,  $\mathbf{F}_j$ , and  $q_j$ , respectively. The stress tensor is  $\tau_{ij}$ , and  $\delta_{ij}$  is the Kronecker delta.

The additional source term  $\mathbf{S}$  is non-zero within a prescribed sponge layer [118, 119], which is designed to create perfectly anechoic conditions by suppressing numerical reflections of pressure waves from the domain boundaries. At the start of the simulation, the flow is gradually accelerated from rest to the target speed using a moving frame technique over eight time units, controlled by a Gaussian growth acceleration function:  $u_a(t) = u_\infty \cdot [(t/t_a - 1)^3(3 \cdot t/t_a + 1)]$  with  $t_a = 8$ . The entire simulation spans 20 non-dimensional time units ( $t^*$ ), with the acceleration phase lasting for the initial 8 time units, as depicted in blue in Figure 3.1. The use of a Gaussian velocity growth function provides two main advantages. First, its smooth initial ramp improves computational stability by gradually introducing flow into the domain. Second, the increased growth rate during most of the acceleration phase more accurately reflects real-world operational conditions compared to linear profiles.

This computational study employs a high-resolution implicit large eddy simulation (ILES) approach, utilizing a wavenumber-optimized discrete filter. This filter is applied directly to the conservative variables at each time step, ensuring dissipation of scales smaller than the filter cutoff wavelength. The ILES technique has been compared with explicit subgrid-scale (SGS) models and shown to accurately capture relevant flow physics [120]. Flux derivatives are computed using wavenumber-optimized, fourth-order pentadiagonal compact finite difference schemes with seven-point stencils [121]. Numerical stability is maintained by applying a sixth-order pentadiagonal compact filter, with a cutoff wavenumber (normalized by grid spacing) of  $0.88\pi$  [122]. Time integration is performed explicitly using the classical fourth-order



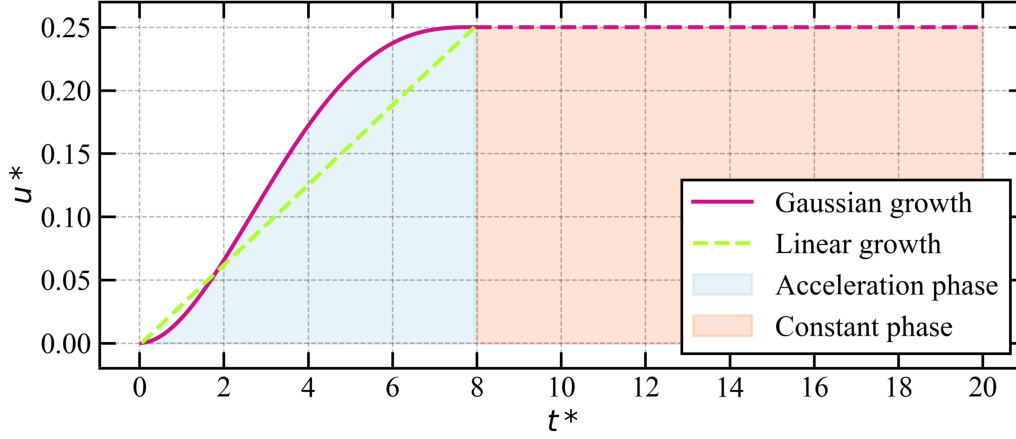


**Figure 3.1:** Acceleration phase at the start of the simulation, comparing Gaussian and linear velocity profiles, followed by a constant phase for  $t^* > 8$ .

Runge–Kutta scheme, with a Courant–Friedrichs–Lewy (CFL) number of 0.99.

Characteristic non-reflecting boundary conditions [123] are implemented in conjunction with a sponge layer at the far-field boundaries. Periodic boundary conditions are enforced on the spanwise boundary planes, while characteristic interface conditions are imposed at block interfaces. No-slip wall boundary conditions are applied on the airfoil surface [124].

The code is fully parallelized using domain decomposition and the Message Passing Interface (MPI) libraries. The distributed solution of pentadiagonal matrix systems is achieved through a quasi-disjoint approach [125]. The governing equations are solved on a structured multi-block grid system consisting of six blocks, with the first and fourth blocks containing the airfoil surfaces, as illustrated in Figure 3.2 (highlighted in blue).

The computational grid is distributed across 1200 processor cores, with each block assigned an appropriate number of processors based on its cell count. The processor allocation for each block is illustrated in Figure 3.2, while the number of grid cells per block is detailed in Table 3.1 in Section 3.2, which clarifies the distribution of processors among the blocks.

All simulations are performed on the IRIDIS-5 cluster at the University of Southampton. Thirty Lenovo SD530 compute nodes are utilized, each equipped with two Intel Xeon Gold 6138 CPUs. Each CPU contains 20 cores operating at a base frequency of 2.0 GHz, providing a total of 40 cores per node. Each node is configured with 192 GB of memory ( $12 \times 16$  GB TruDDR4 2666 MHz RDIMMs). Storage for each node includes two 2 TB 7.2K SAS hard drives, suitable for bulk storage and data logging, as well as a 128 GB SATA SSD, typically used for the operating system or high-IOPS workloads due to its superior random access speed compared to HDDs. High-speed networking is provided by a Mellanox ConnectX-4 EDR IB

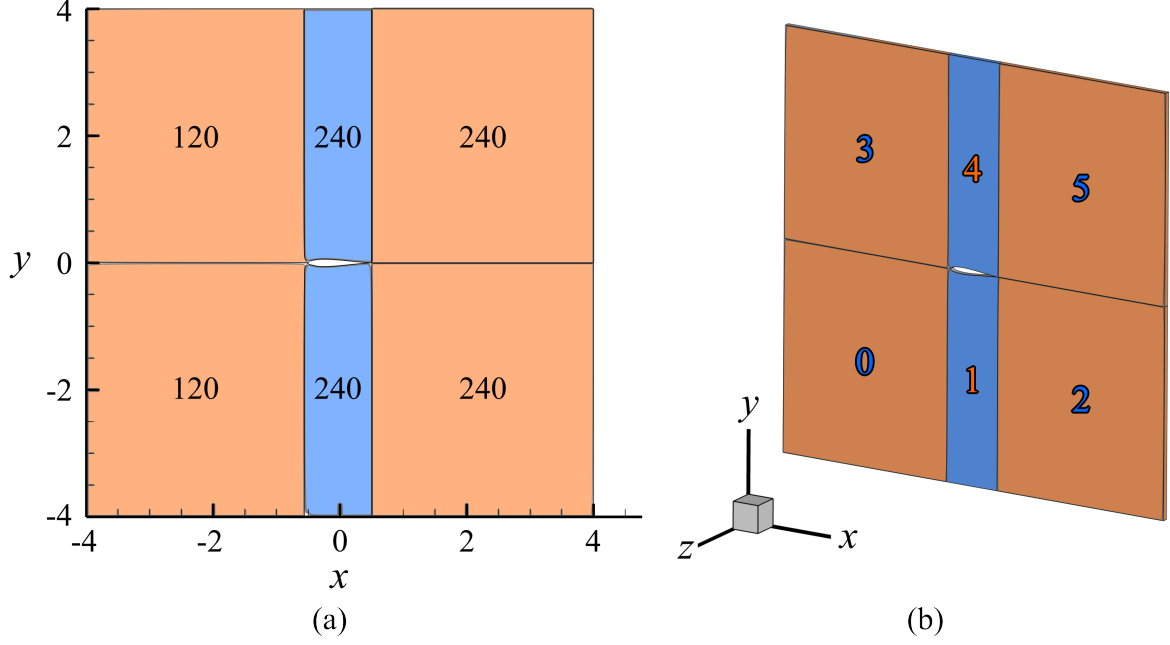


**Figure 3.2:** Block distribution for the airfoil multi-block grid system: (a) 2D XY-plane view showing the number of CPUs assigned to each block, and (b) 3D view of the same multi-block structure with block nomenclature.

VPI HCA, a high-performance network adapter supporting both EDR (Enhanced Data Rate) InfiniBand and 100 Gb/s Ethernet via its Virtual Protocol Interconnect (VPI) feature, ensuring fast data transfer and low latency for supercomputing applications.

## 3.2 Geometry and Mesh Generation

The computational study investigates a symmetric Joukowski airfoil with a 12% thickness-to-chord ratio. Two geometric configurations are analyzed: the primary trailing edge (PTE) airfoil and the serrated trailing edge (STE) variant. The STE configuration incorporates zero-thickness serrations extending 10% of the chord length ( $0.1L_c$ ) downstream from the baseline geometry, with a wavelength of  $0.05L_c$ , as illustrated in Figure 3.3(a).

The computational mesh employs a structured multi-block topology based on an H-grid configuration, with grid stretching applied in both the streamwise and vertical directions to achieve optimal resolution near the airfoil surface, thereby capturing the boundary layer accurately. The airfoil chord length  $L_c$  serves as the characteristic dimension, with the spanwise extent limited to  $0.1L_c$ . The domain extends  $\pm 4L_c$  in both streamwise and vertical directions ( $x, y \in [-4, 4]$ ), centered at the airfoil mid-chord, with spanwise boundaries at  $z \in [-0.05L_c, 0.05L_c]$ , as depicted in Figure 3.2.

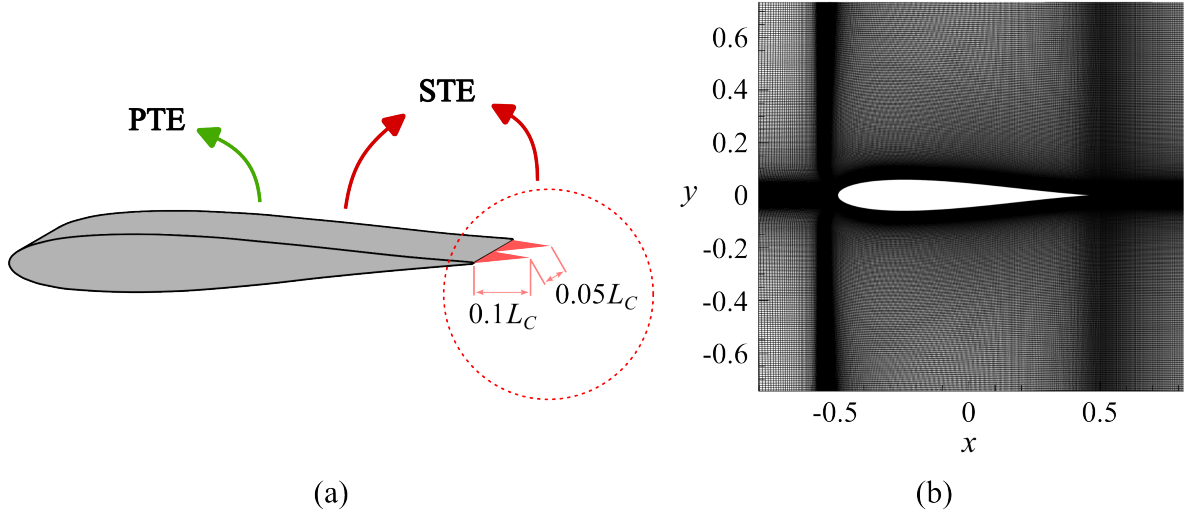


**Figure 3.3:** (a) Geometry of the primary airfoil with added serrations (marked red) that shows serration length and wavelength. (b) Mesh distribution on the 2D zoomed-in part of the domain around the airfoil's surface.

Grid independence is established through a systematic convergence study employing three mesh configurations: coarse (G1), medium (G2), and fine (G3). The refinement strategy applies a uniform scaling factor of 1.25 in all coordinate directions, except for inlet blocks, where streamwise resolution remains constant to maintain consistent boundary condition implementation. This approach yields a fine mesh with approximately twice the cell count of the coarse configuration. Table 3.1 summarizes the grid distribution characteristics across the generalized coordinate system.

**Table 3.1:** Grid distribution for PTE airfoil simulation validation employs three different mesh configurations.

	$n_{\xi, \text{airfoil}}$	$n_{\xi}$	$n_{\eta}$	$n_{\zeta}$	$n_{\text{total}} [\cdot 10^6]$
G1	256	672	512	72	24.77
G2	320	800	640	88	45.06
G3	400	960	800	110	84.48

For the medium mesh (G2), the cell distribution allocates  $4.51 \cdot 10^6$  cells to blocks 0 and 3, while the remaining four blocks (1, 2, 4, and 5) contain  $9.01 \cdot 10^6$  cells each, totaling  $45.06 \cdot 10^6$  cells. This distribution ensures optimal load balancing across the 1200 processor cores while maintaining computational efficiency.

The wall-resolved LES approach necessitates stringent near-wall grid spacing to accurately capture boundary layer physics without wall modeling. Figure 3.4 presents a comprehensive

analysis of near-wall mesh resolution normalized by friction velocity, where  $s^+$ ,  $n^+$ , and  $z^+$  represent streamwise, wall-normal, and spanwise spacing, respectively.

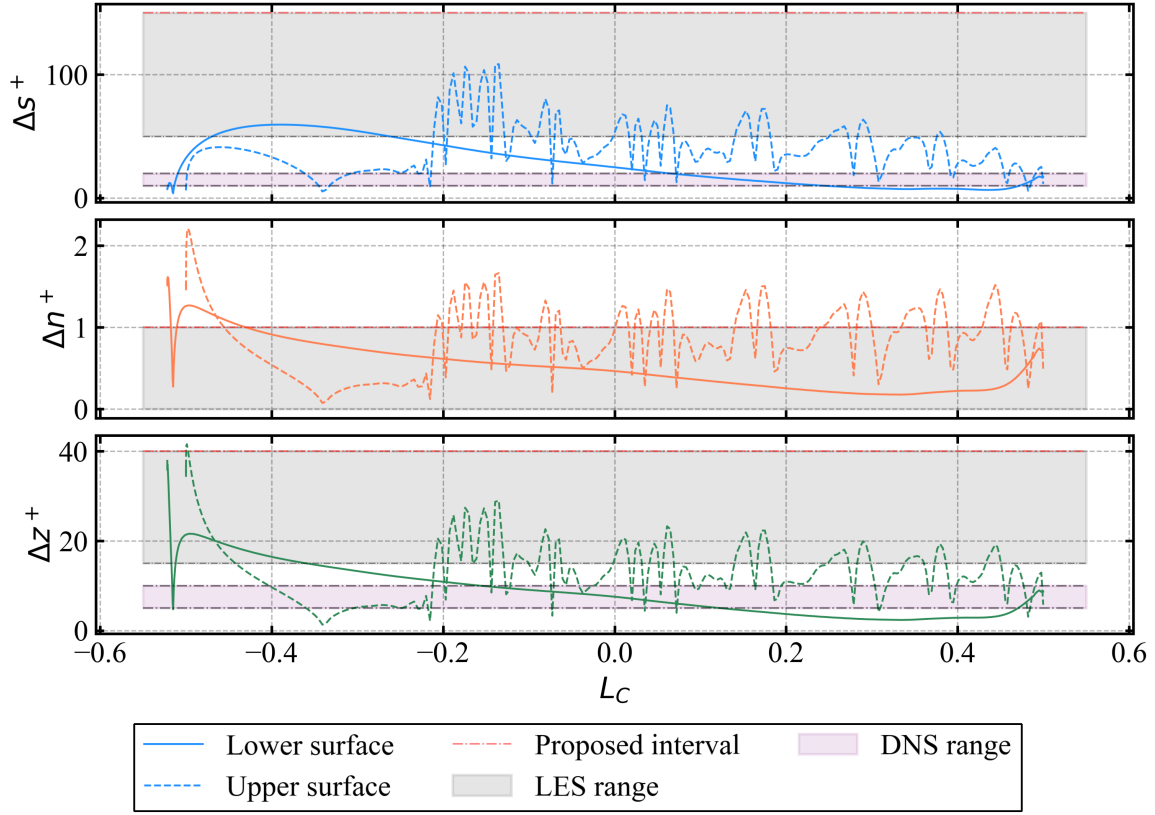


**Figure 3.4:** Wall-unit grid spacing for the G2 PTE airfoil where  $s^+$ ,  $n^+$ , and  $z^+$  represent streamwise (blue), normal (orange), and spanwise (green) spacing, respectively. Hatched parts represent the proposed LES and DNS range, while the red dash-dotted line represents the LES border.

The streamwise resolution consistently satisfies LES requirements ( $s^+ < 150$ ) as recommended by Piomelli [126] and Georgiadis et al. [127]. Spanwise spacing remains within acceptable limits ( $z^+ < 40$ ) for 98% of the airfoil surface, with minor exceedances occurring near the leading edge where laminar flow conditions prevail. Wall-normal spacing ( $n^+ < 1$ ) is achieved over approximately 70% of the airfoil surface, with elevated values concentrated in the leading edge region where laminar boundary layer physics dominate. Crucially, turbulent flow regions maintain  $n^+ < 1.5$ , ensuring adequate boundary layer resolution for accurate turbulence prediction.

Grid convergence is demonstrated through comprehensive force coefficient analysis across the three mesh configurations, as presented in Figure 3.5. The upper panels display complete simulation time histories for non-dimensional forces in both  $x$ - and  $y$ -directions, while the lower

panels provide a detailed examination of pressure and viscous force components during the constant velocity phase, emphasizing oscillation capture fidelity across different grid resolutions.

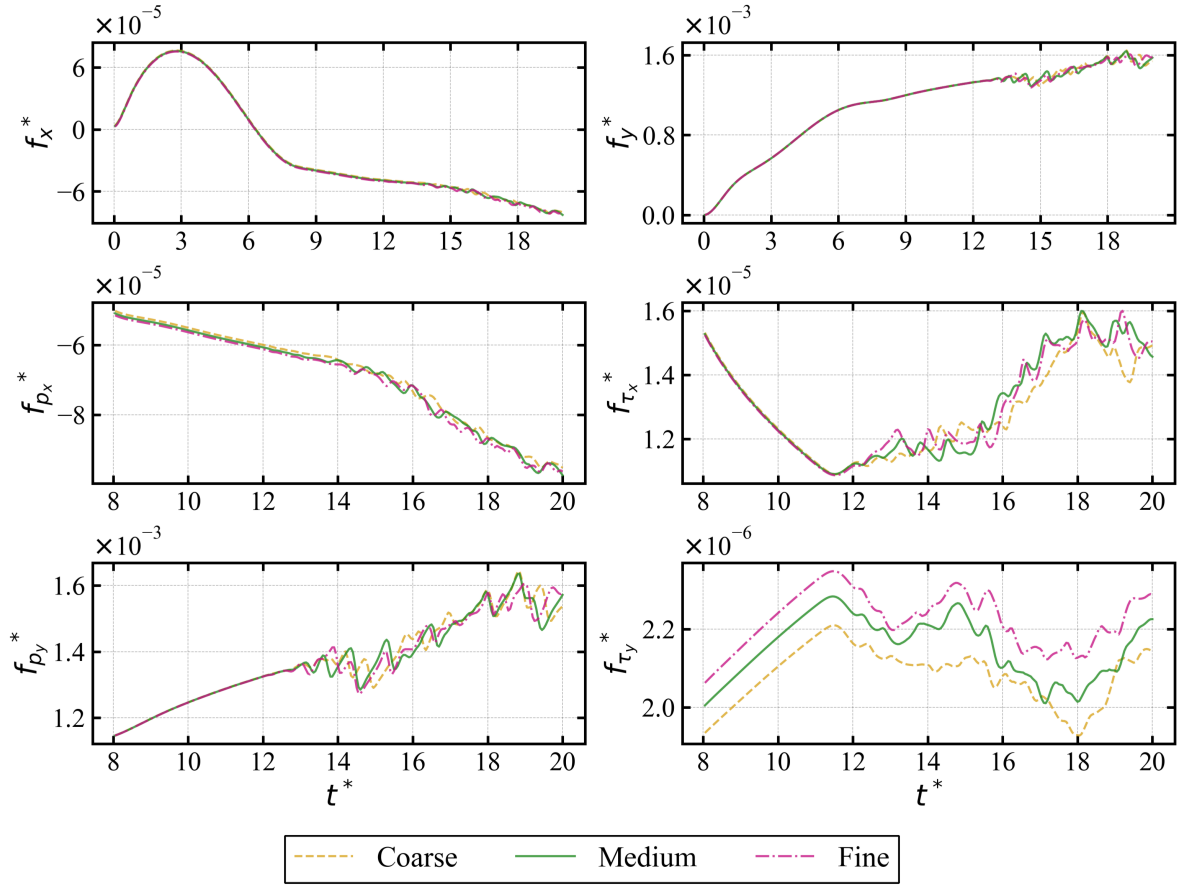


**Figure 3.5:** Grid validation for the PTE airfoil. The first two graphs compare the non-dimensional forces in the  $x$ - and  $y$ -directions. The remaining four graphs provide a detailed view of the pressure and skin friction components of the forces for the three different meshes: coarse (blue), medium (orange), and fine (green).

Root Mean Square Error (RMSE) analysis confirms excellent grid convergence characteristics. For non-dimensional force in the  $x$ -direction, RMSE values of  $1.04 \cdot 10^{-6}$  (G1-G2) and  $9.04 \cdot 10^{-7}$  (G2-G3) demonstrate excellent correlation. Similarly,  $y$ -direction forces exhibit RMSE values of  $2.49 \cdot 10^{-5}$  (G1-G2) and  $1.93 \cdot 10^{-5}$  (G2-G3). The medium mesh (G2) is selected for subsequent analyses based on its superior agreement with the fine mesh, particularly in accurately capturing temporal oscillations, while maintaining computational efficiency.

Computational results are validated against XFOIL predictions for the 12% thick Joukowski airfoil under identical flow conditions. Figure 3.6 presents pressure coefficient distributions comparing LES results with XFOIL data. While instantaneous LES results exhibit characteristic

turbulent fluctuations, particularly in the aft portion of the airfoil (Figure 3.6(a)), the time-averaged pressure distribution demonstrates excellent agreement with XFOIL predictions in the turbulent flow region (Figure 3.6(b)).

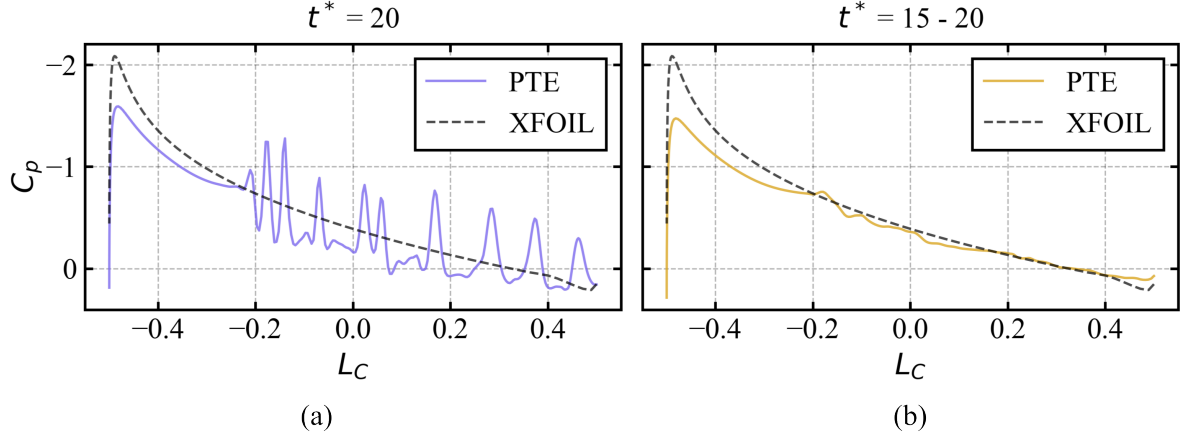


**Figure 3.6:** Comparison of the primary trailing edge airfoil for: (a) the last time unit  $t^* = 20$ , and (b) for the time-averaged values from 15 to 20 time units.

The observed overprediction of maximum  $C_p$  by XFOIL in the laminar region is consistent with documented limitations of panel methods for thick airfoils [128]. The focus on initial acceleration and short post-acceleration phases, rather than fully converged steady-state conditions, explains minor discrepancies in the laminar region, which would diminish with extended simulation duration. Nevertheless, the excellent correlation in the turbulent region validates the computational approach for the intended analysis scope.

### 3.3 Primary Trailing Edge (PTE) Airfoil Analysis

This section provides a comprehensive analysis of the PTE airfoil aerodynamic and flow physics characteristics. First, Subsection 3.3.1 presents the temporal evolution of aerodynamic performance during the acceleration and post-acceleration phases. Second, Subsection 3.3.2 examines the flow in detail, including boundary layer development and acoustic wave interactions with flow characteristics.

#### 3.3.1 Force Analysis and Starting Vortex Dynamics

As detailed in Section 3.1, the flow undergoes acceleration according to a Gaussian velocity profile during the initial eight non-dimensional time units (Figure 3.1). Since all quantities

are presented in non-dimensional form and the effective angle of attack varies continuously during acceleration, the analysis focuses on non-dimensional forces in the  $x$ - and  $y$ -directions rather than conventional drag and lift coefficients. This approach provides a more fundamental understanding of force generation mechanisms during unsteady flow conditions, where traditional steady-state coefficient definitions may not adequately capture the transient aerodynamic behavior.

Since this analysis involves viscous flow, both pressure and skin friction components influence the overall force intensity. However, surface shear stress variables are not directly available in the surface zone data. Therefore, velocity gradients at boundary surfaces must be derived from the volumetric velocity field of the computational domain. This approach requires the simultaneous loading of both surface zones, where force calculations are desired, and the adjacent volume zones that contain the requisite velocity field information. This computational strategy ensures accurate representation of viscous effects while maintaining consistency with the underlying Navier-Stokes equations [5].

The computational methodology for determining velocity gradients depends fundamentally on the grid topology employed in the numerical simulation. Unstructured finite-element grids require the implementation of moving least-squares approximation methods to reconstruct the necessary gradient information from the irregular node distribution. On the other hand, structured grids utilize velocity gradients that are computed using established curvilinear coordinate transformation techniques, which leverage the inherent grid connectivity to maintain high accuracy. The latter approach is employed here, as the analysis utilizes a structured multi-block topology based on an H-grid configuration, as mentioned in Section 3.2. The structured grid approach offers superior accuracy for gradient calculations due to the regular connectivity pattern and well-defined coordinate transformations [5].

The mathematical framework underlying these calculations is grounded in the principles of continuum mechanics. Under the assumption of Stokes' hypothesis, where the second coefficient of viscosity vanishes, the Newtonian stress tensor for a viscous fluid is expressed as:

$$\mathbf{T} = \mu [\nabla \mathbf{V} + (\nabla \mathbf{V})^T] - \left[ \frac{2}{3} \mu (\nabla \cdot \mathbf{V}) + p \right] \mathbf{I} \quad (3.3)$$

which can be written down in a matrix form as:

$$\mathbf{T} = \mu \begin{bmatrix} 2\frac{\partial u}{\partial x} - \frac{2}{3}D & \frac{\partial v}{\partial x} + \frac{\partial u}{\partial y} & \frac{\partial w}{\partial x} + \frac{\partial u}{\partial z} \\ \frac{\partial v}{\partial x} + \frac{\partial u}{\partial y} & 2\frac{\partial v}{\partial y} - \frac{2}{3}D & \frac{\partial v}{\partial z} + \frac{\partial w}{\partial y} \\ \frac{\partial w}{\partial x} + \frac{\partial u}{\partial z} & \frac{\partial v}{\partial z} + \frac{\partial w}{\partial y} & 2\frac{\partial w}{\partial z} - \frac{2}{3}D \end{bmatrix} - p\mathbf{I} \quad (3.4)$$

with

$$D = (\nabla \cdot \mathbf{V}) = \frac{\partial u}{\partial x} + \frac{\partial v}{\partial y} + \frac{\partial w}{\partial z} \quad (3.5)$$

where  $\mu$  is the dynamic viscosity,  $p$  is pressure, and  $\mathbf{I}$  is the identity matrix. The stress tensor formulation captures both the viscous shear effects and the normal stress contributions, providing a complete description of the fluid's mechanical response to deformation [34]. The surface traction is obtained by multiplying the stress tensor by the outward-pointing unit normal vector.

In the end, forces in  $x$ - and  $y$ -directions are calculated as:

$$f_x = \left[ \mu \left( 2\frac{\partial u}{\partial x} - \frac{2}{3}D \right) - p \right] \cdot n_x + \left[ \mu \left( \frac{\partial v}{\partial x} + \frac{\partial u}{\partial y} \right) \right] \cdot n_y + \left[ \mu \left( \frac{\partial w}{\partial x} + \frac{\partial u}{\partial z} \right) \right] \cdot n_z \quad (3.6)$$

$$f_y = \left[ \mu \left( \frac{\partial v}{\partial x} + \frac{\partial u}{\partial y} \right) \right] \cdot n_x + \left[ \mu \left( 2\frac{\partial v}{\partial y} - \frac{2}{3}D \right) - p \right] \cdot n_y + \left[ \mu \left( \frac{\partial v}{\partial z} + \frac{\partial w}{\partial y} \right) \right] \cdot n_z \quad (3.7)$$

where  $n_x$ ,  $n_y$ , and  $n_z$  are the unit normal vector components. This formulation ensures that all contributions to the surface force are properly accounted for, including both pressure and viscous stress effects across all three spatial dimensions.

To enhance understanding of force evolution mechanisms, both force components are decomposed into pressure and skin friction contributions, as illustrated in Figure 3.7. This decomposition is particularly valuable for identifying the dominant force-generating mechanisms and understanding how different physical phenomena contribute to the overall aerodynamic performance.

The  $y$ -direction force components are presented in Figure 3.7(b), clearly demonstrating that the pressure component dominates the total force  $f_y^*$ , while the skin friction contribution remains negligible throughout the simulation period. The pressure component exhibits pronounced growth during the acceleration phase, followed by oscillatory behavior rather than



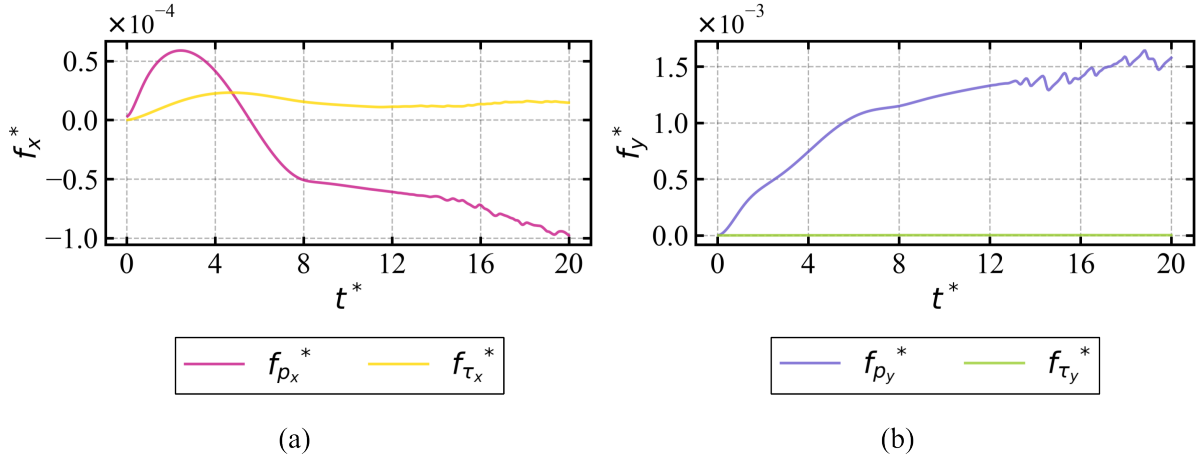


**Figure 3.7:** Temporal evolution of non-dimensional force components for the PTE airfoil at  $Re = 250,000$ : (a)  $x$ -direction forces showing pressure component (violet) and skin friction component (yellow); (b)  $y$ -direction forces showing pressure component (blue) and skin friction component (green).

smooth convergence to a steady state. These oscillations in  $f_{p_y}^*$ , which commence around  $t^* = 13$ , are analyzed in detail in Subsection 3.3.2. It should be noted that all simulations in Chapter 3 focus specifically on the initial acceleration and near post-acceleration phases with high temporal resolution, rather than achieving fully converged steady-state conditions.

The  $x$ -direction force components, shown in Figure 3.7(a), reveal a different behavior compared to the  $y$ -direction forces. While the pressure component remains dominant, the skin friction component contributes more significantly to the total  $x$ -direction force. The pressure component exhibits higher absolute values and more pronounced temporal oscillations compared to the relatively smooth evolution of skin friction. The initial high-pressure peak observed around  $t^* = 2.4$  is attributed to the flow acceleration process and the formation of the starting vortex phenomenon, as documented in previous studies [129, 130].

The starting vortex formation is an inherent consequence of the Joukowski airfoil's sharp trailing edge geometry combined with the non-zero angle of attack, as illustrated in Figure 3.8. This figure presents both the computational vorticity contour (Figure 3.8(a)) and a schematic representation of the vortex system balance (Figure 3.8(b)).

According to Kelvin's circulation theorem, the circulation around any material fluid contour remains constant in an inviscid flow. This fundamental principle forms the theoretical basis for understanding lift generation and starting vortex formation around airfoils. When an airfoil begins its motion from rest, the initial circulation around any contour enclosing the airfoil is zero. To maintain this zero net circulation as lift develops, the positive circulation that forms

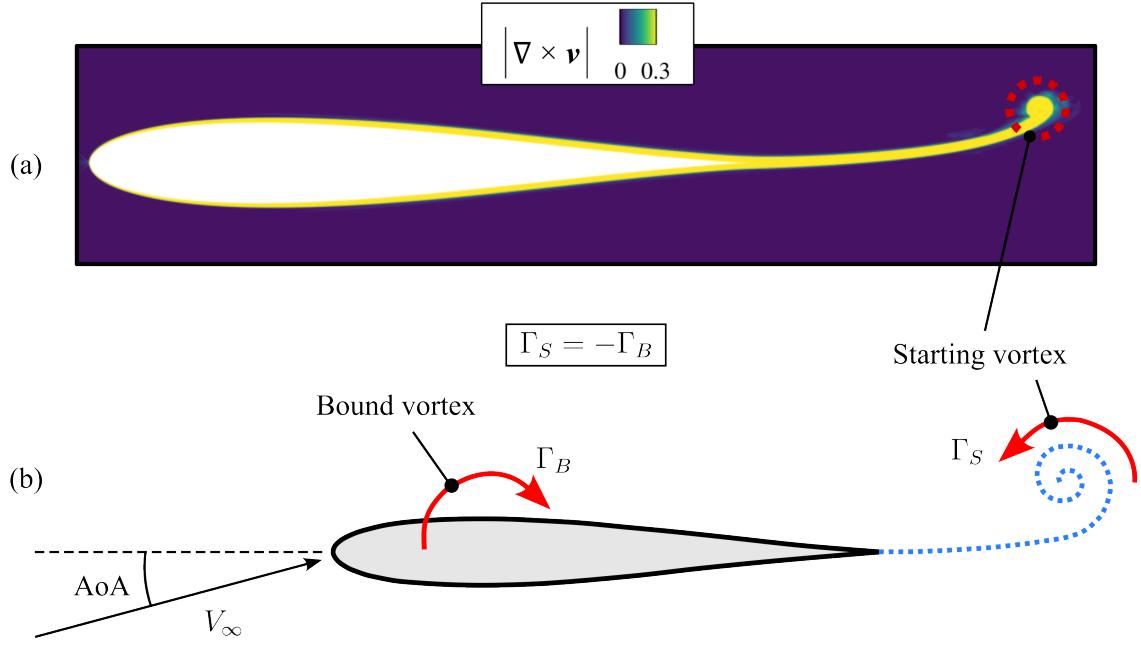


**Figure 3.8:** Starting vortex formation and circulation balance: (a) computational vorticity contour showing the starting vortex development (yellow regions indicate higher vorticity magnitude); (b) schematic illustration of the circulation balance between bound vortex ( $\Gamma_B$ ) and starting vortex ( $\Gamma_S$ ) according to Kelvin’s circulation theorem.

around the airfoil (bound vortex,  $\Gamma_B$ ) must be balanced by an equal and opposite circulation (starting vortex,  $\Gamma_S$ ), such that the total circulation remains zero:  $\Gamma_B + \Gamma_S = 0$  [82].

The bound vortex represents the circulation responsible for lift generation according to the Kutta-Joukowski theorem, where lift per unit span is given by  $L' = \rho U \Gamma_B$ . This circulation remains effectively attached to the airfoil and is maintained by the enforcement of the Kutta condition at the sharp trailing edge, which requires that the flow leave the trailing edge smoothly without infinite velocities. The starting vortex forms during the initial motion as a consequence of this circulation development and subsequently convects downstream with the flow [82].

The physical mechanism of starting vortex formation is fundamentally linked to the viscous effects at the sharp trailing edge. When the airfoil first begins to move, the inviscid flow solution would predict infinite velocities around the sharp trailing edge. However, the viscous boundary layer cannot sustain such extreme velocity gradients, causing the flow to separate and roll up into the starting vortex. This vortex formation process continues until the Kutta condition is established, after which the flow leaves the trailing edge tangentially [110].

For a symmetric airfoil at zero angle of attack in steady flow, classical thin airfoil theory predicts zero circulation and hence zero lift. Under these conditions, no bound vortex develops

around the airfoil, and consequently, no starting vortex is required to maintain circulation balance. The flow remains symmetric about the chord line, with the stagnation point located at the leading edge and the flow departing smoothly from the trailing edge without circulation [110].

In the present study, with an angle of attack of  $5^\circ$ , the bound vortex intensifies the flow acceleration on the airfoil's suction side. During the mean flow acceleration, the low-pressure region migrates from the trailing edge toward the leading edge, as visualized in the upper portion of Figure 3.9 and highlighted by the red dotted ellipses. Simultaneously, the high-pressure stagnation region shifts downstream along the airfoil surface, as shown in the lower portion of Figure 3.9. This phenomenon is quantified in the right panels of Figure 3.9, which track the temporal evolution of the maximum pressure coefficient location (stagnation point) on the airfoil surface.

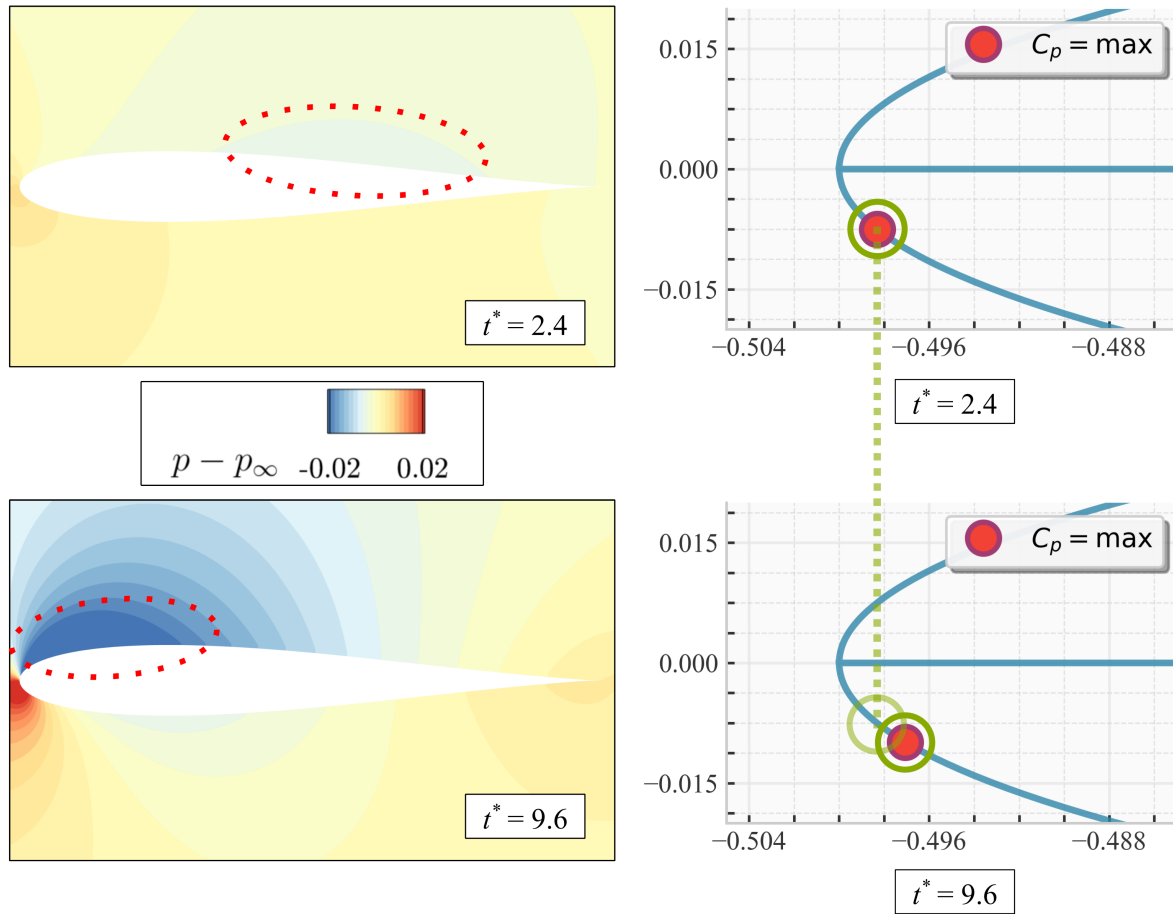


**Figure 3.9:** Pressure field evolution and stagnation point migration: (left) pressure fluctuation contours at  $t^* = 2.4$  (top) and  $t^* = 9.6$  (bottom), with low-pressure regions highlighted by red ellipses; (right) corresponding pressure coefficient distributions showing the downstream migration of maximum  $C_p$  location (stagnation point). The green circles emphasize the stagnation point displacement between the two time instances.

The temporal evolution of the stagnation point location provides insight into the effective angle of attack variation during the acceleration process. The transparent green circle in the lower right panel indicates the stagnation point position at  $t^* = 2.4$ , while the solid red circle with green highlighting shows its new downstream location at  $t^* = 9.6$ . This downstream migration correlates with the peak stagnation pressure observed at  $t^* = 2.4$  in Figure 3.7(a), demonstrating the coupled evolution of pressure distribution and force generation during the unsteady acceleration phase. This stagnation point migration is characteristic of unsteady airfoil motion and provides valuable insight into the transient aerodynamic behavior that cannot be captured through steady-state analysis alone.

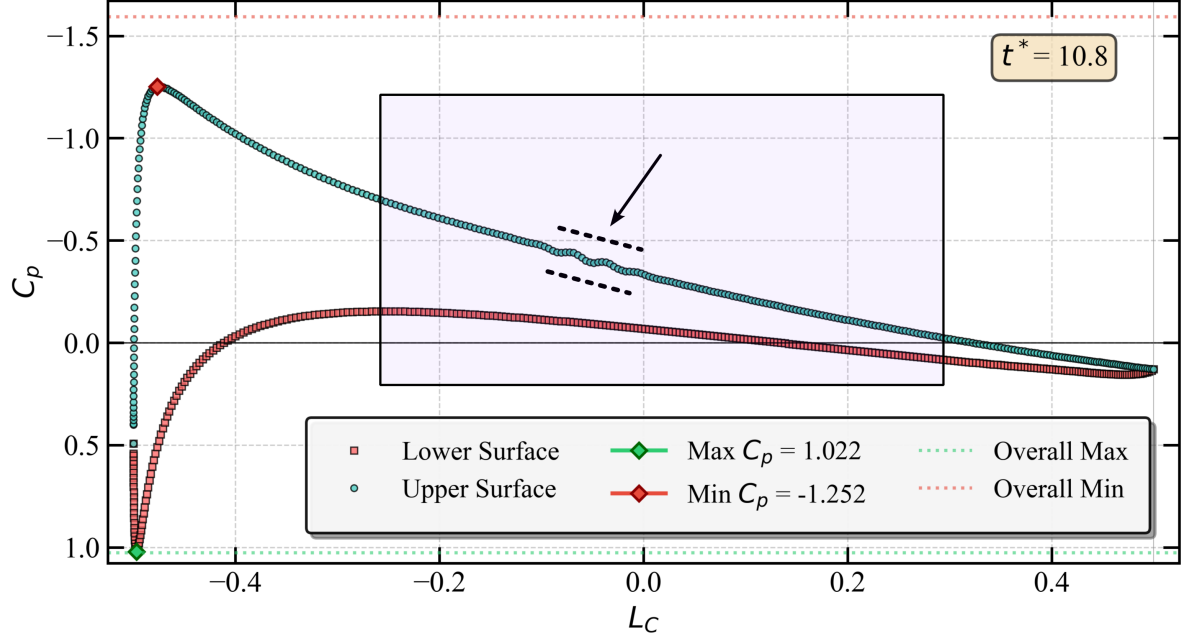
### 3.3.2 Coupled Aerodynamic-Aeroacoustic Analysis of Boundary Layer Transition

The oscillations observed around  $t^* = 13$  in Subsection 3.3.2, Figure 3.7, warrant a detailed investigation to understand the underlying flow physics. While non-dimensional force components provide valuable quantitative information, pressure coefficient analysis offers superior insight into local flow characteristics and boundary layer behavior. By extracting pressure and coordinate data from each voxel on the airfoil's surface, the pressure coefficient ( $C_p$ ) is calculated at each time step. For computational efficiency and given the minimal three-dimensional effects in this configuration, the analysis focuses on the mid-plane cross-section.

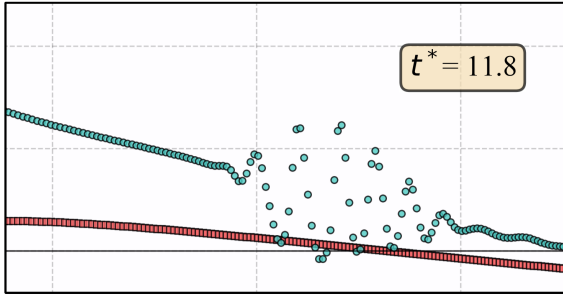
In comparison to the non-dimensional force in the y-direction, the pressure coefficient analysis provides an enhanced understanding of flow characteristics. Furthermore, integrating the area encompassed by the  $C_p$  distribution yields the pressure component of the lift coefficient  $C_{L_p}$ , which effectively represents the total lift coefficient due to the negligible skin friction contribution demonstrated in Subsection 3.3.1 and illustrated in Figure 3.7(b).

Accordingly, Figure 3.10 illustrates the temporal evolution of pressure coefficient distributions, revealing critical flow transition phenomena. Following the initial acceleration phase, disturbances emerge on the airfoil's suction side, as highlighted by the teal circles in the figure. These oscillations progressively intensify over time, as demonstrated in the sequential snapshots of Figures 3.10(b) and (c).

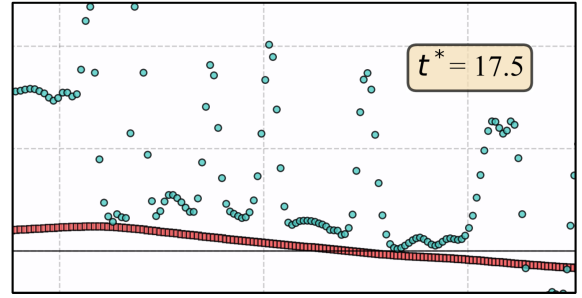
As a reminder, Figure 3.10(a) shows upper and lower surfaces of the Joukowski airfoil operating at  $5^\circ$  angle of attack, Reynolds number of 250,000, and Mach number of 0.25. At  $t^* = 10.8$ , initial oscillations appear near the mid-chord region, closer to the leading edge,



(a)



(b)



(c)

**Figure 3.10:** Temporal evolution of pressure coefficient distribution on the airfoil mid-plane surface showing boundary layer instability development: (a) initial oscillation detection at  $t^* = 10.8$ , (b) amplitude growth and downstream propagation at  $t^* = 11.8$ , and (c) fully developed oscillatory behavior at  $t^* = 17.5$ . Teal circles and red rectangles represent upper and lower surface  $C_p$  values, respectively. Red and green diamonds indicate the instantaneous minimum and maximum  $C_p$  values, respectively, while dotted lines represent the global extrema throughout the simulation.

as indicated by the black arrow and dashed lines in Figure 3.10(a). Within one time unit, these oscillations intensify significantly and propagate toward the trailing edge with markedly increased amplitude, as shown in Figure 3.10(b). By  $t^* = 17.5$ , the airfoil's upper surface exhibits significant oscillations (visible at Figure 3.10c) that extend in both leading and trailing edge direction, compromising the stability of the PTE airfoil.

To complement the two-dimensional pressure coefficient analysis and capture three-dimensional flow structures,  $Q$ -criterion iso-contours are employed for vortex visualization. Despite the limited spanwise extent (10% chord length) with periodic boundary conditions, this approach

provides valuable insight into boundary layer transition mechanisms. Figure 3.11 presents detailed boundary layer instability development through vortex structure visualization on the airfoil's suction side. The  $Q$ -criterion visualization reveals boundary layer instabilities earlier than the pressure coefficient analysis, with initial disturbances detected around  $t^* = 10.2$  (Figure 3.11(a)). This enhanced sensitivity stems from the three-dimensional nature of the visualization, which captures subtle flow structures invisible in two-dimensional cross-sections.

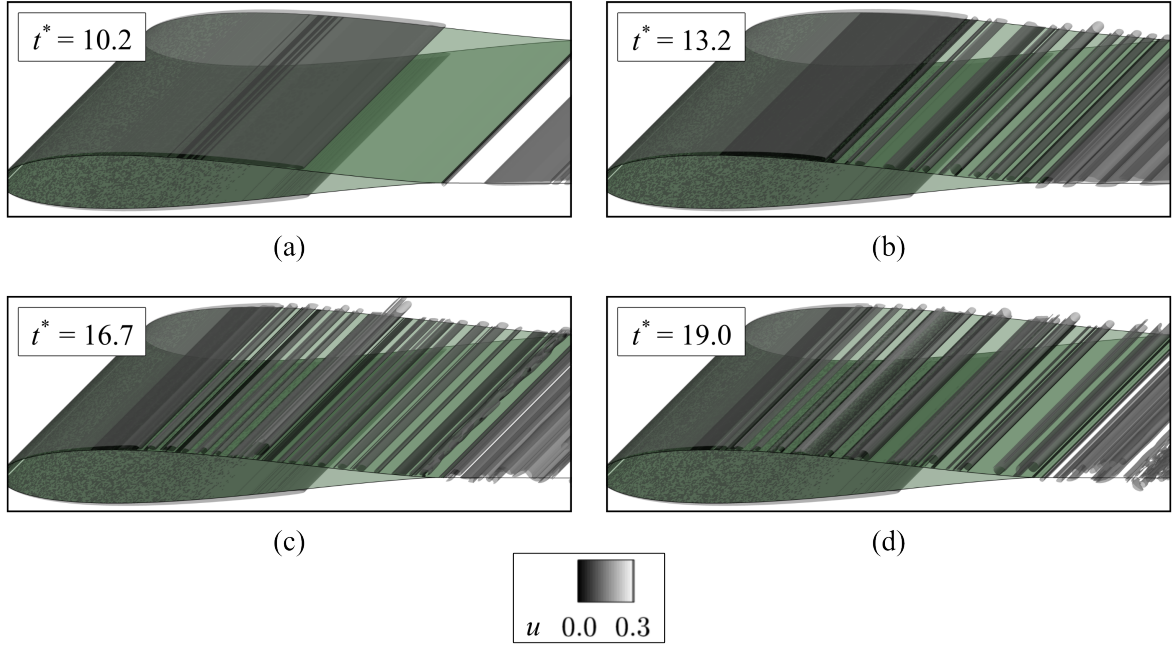


**Figure 3.11:** Boundary layer transition visualization using  $Q$ -criterion iso-surfaces ( $Q = 0.01$ ) colored by streamwise velocity magnitude: (a) initial instability detection at  $t^* = 10.2$ , (b) downstream propagation and amplification at  $t^* = 13.2$ , (c) characteristic roll-up formation at  $t^* = 16.7$ , and (d) wake turbulence development at  $t^* = 19.0$ . The spanwise dimension is exaggerated for visualization clarity.

The temporal evolution demonstrates the systematic propagation of instability. The boundary layer remains laminar and stable until  $t^* = 10.2$ , after which transition commences with downstream-propagating oscillations. The initial boundary layer disturbances reach the trailing edge within approximately three time units, as shown in Figure 3.11(b). At  $t^* = 16.7$ , characteristic roll-up structures emerge with increased irregularity, though without full turbulent transition. By  $t^* = 19.0$ , while maintaining similar roll-up distributions, the iso-contours reveal turbulence development in the wake region (Figure 3.11d), which is visually better encompassed in Figure 3.13c.

The time step window between  $t^* = 13.2$  and  $t^* = 16.7$  (Figures 3.11(b) and (c)) corresponds to the formation of a laminar separation bubble (LSB), a well-documented aerodynamic

phenomenon occurring on airfoils at moderate Reynolds numbers and adverse pressure gradients [82, 131]. An LSB forms when the laminar boundary layer separates due to an adverse pressure gradient but subsequently transitions to turbulence and reattaches downstream, creating a recirculation zone characterized by reversed flow. This fundamental mechanism occurs because the separated laminar shear layer becomes unstable and undergoes transition to turbulence, which enhances momentum transfer and enables the turbulent flow to overcome the adverse pressure gradient and reattach to the surface.

The presence of an LSB significantly influences airfoil performance by altering the effective airfoil shape and pressure distribution on the suction side. The recirculation zone within the bubble acts as a virtual extension of the airfoil geometry, modifying the local flow field and pressure recovery characteristics. If the separated laminar flow fails to reattach, the separated region grows, potentially leading to a stall characterized by a dramatic loss of lift and an increase in drag [82]. However, when successful reattachment occurs, the turbulent boundary layer downstream of the bubble can sustain higher adverse pressure gradients compared to the original laminar boundary layer, partially recovering aerodynamic performance.

The formation and dynamics of LSBs depend critically on Reynolds number, angle of attack, and pressure gradient distribution along the airfoil surface [131]. At Reynolds numbers in the range of  $10^5$  to  $10^6$ , as encountered in the present study, LSBs are particularly common and can induce unsteady aerodynamic forces due to their inherent sensitivity to flow disturbances and transition processes. The influence of Reynolds numbers on the boundary layer is examined in the subsequent analysis through Section 3.5. The unsteady behavior of the LSB, including periodic growth and bursting cycles, directly contributes to the oscillations in lift and drag coefficients observed in Figure 3.7, particularly the pronounced fluctuations that begin around  $t^* = 13$ .

This LSB formation is clearly visualized through streamline analysis in Figure 3.12. Figure 3.12(a) illustrates the stable laminar boundary layer configuration at  $t^* = 10.0$ , representing the baseline attached flow condition. Detailed examination of the suction side reveals initial boundary layer instabilities at  $t^* = 11.3$  (Figure 3.12(b)), consistent with the  $Q$ -criterion analysis showing roll-up formation without three-dimensional deviation or turbulent transition. By  $t^* = 14.0$ , the laminar separation bubble becomes clearly defined, with the white blank space indicating the recirculation zone region highlighted by the green dotted ellipse in Figure 3.12(c).

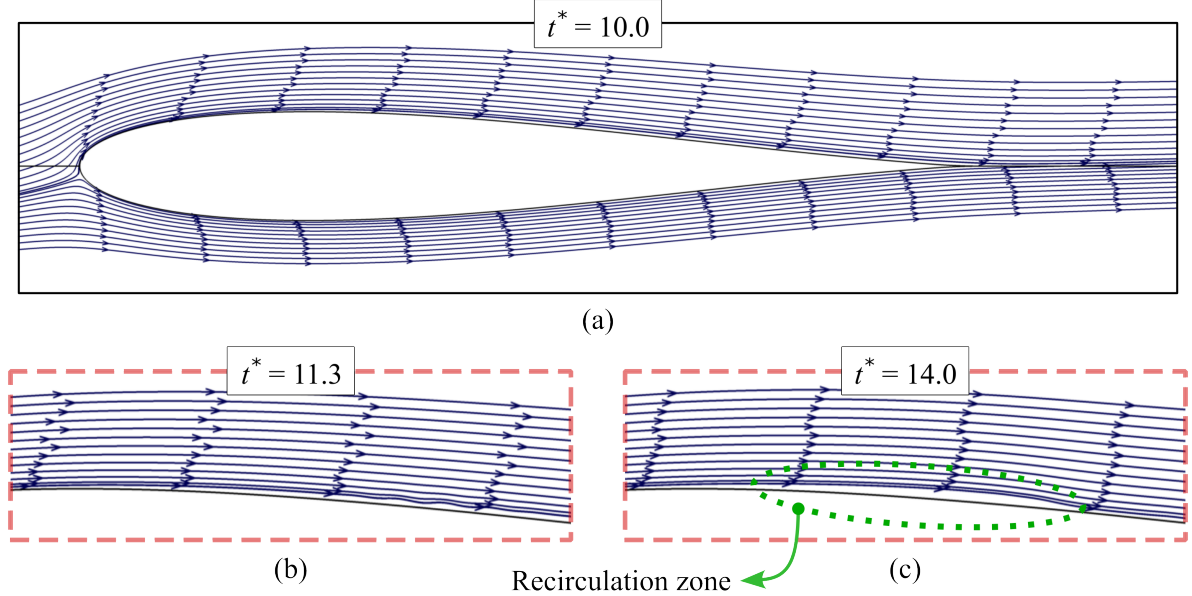


**Figure 3.12:** Mid-plane streamline evolution showing boundary layer transition progression: (a) attached laminar boundary layer at  $t^* = 10.0$ , (b) initial boundary layer disturbances at  $t^* = 11.3$ , and (c) fully developed laminar separation bubble with recirculation zone (highlighted by green dotted ellipse) at  $t^* = 14.0$ .

The physical mechanism underlying LSB formation in the present case is driven by the combination of the airfoil's curvature-induced adverse pressure gradient and the unsteady acceleration effects. As the flow decelerates along the suction side due to the adverse pressure gradient, the momentum deficit in the laminar boundary layer leads to separation. The separated shear layer then undergoes natural transition to turbulence through amplification of instability waves, eventually reattaching as a turbulent boundary layer capable of overcoming the adverse pressure gradient. This process is fundamental to understanding transition phenomena on airfoils and represents a critical consideration for applications in the moderate Reynolds number regime encountered by small aircraft and unmanned aerial vehicles.

While the analysis has focused on boundary layer oscillations, it is equally important to address the occurrence of shear layer instability in the wake region. Due to airflow detachment at the trailing edge, a high-velocity gradient forms between the accelerated flow on the suction side and the slower-moving air below. When velocity differences across the layer become sufficiently large, the growth of vortical structures within the shear layer begins, commonly associated with Kelvin-Helmholtz instability. This instability manifests as a result of the Bernoulli effect, where perturbations in the shear layer create pressure differences that amplify



the initial disturbances, potentially leading to secondary vortex formation and enhanced mixing. Furthermore, instability in the shear layer generates low-amplitude sound waves, which can be visualized by plotting contours of density and velocity divergence with a reduced legend range. Figure 3.13 highlights both the sound wave contours and the  $Q$ -criterion iso-contours for boundary layer and shear layer instabilities.

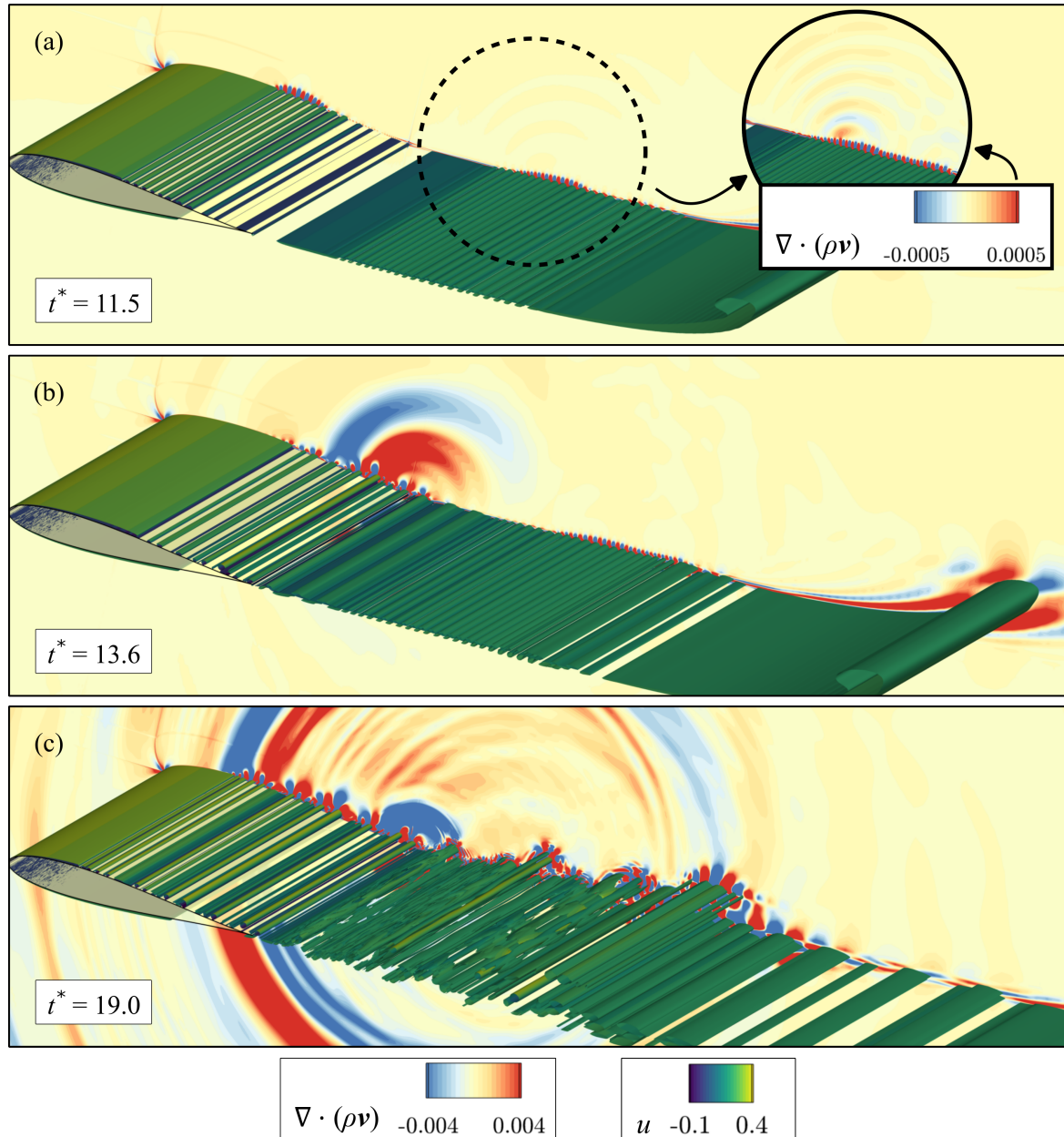


**Figure 3.13:** Representation of shear layer and boundary layer instability using  $Q$ -criterion ( $Q = 0.01$ ) at different time instances: (a)  $t^* = 11.5$ , (b)  $t^* = 13.6$ , and (c)  $t^* = 19.0$ . A mid-plane cut along the spanwise axis visualizes sound waves at the same time instances as the 3D vortices. Legends apply to all subfigures, except for the extracted circle in the upper-right corner, which represents a reduced legend range to visualize shear layer-generated sound waves.

$Q$ -criterion iso-contours are colored by streamwise velocity, while sound waves are visualized at the domain's mid-plane cut. Coherent vortical structures form behind the trailing edge as the shear layer folds over itself, creating roll-ups. These structures generate shear layer noise, which is barely visible in Figure 3.13(a). However, it becomes more pronounced in the upper-right circle, where the legend range is reduced by a factor of eight. In contrast, trailing edge noise is more prominent, as highlighted in Figure 3.13(b). Trailing edge noise occurs when vortical structures from the boundary layer move downstream and interact with the airfoil's sharp trailing edge. These pressure fluctuations manifest as acoustic waves that propagate outward as sound. In this case, trailing edge noise begins around  $t^* = 13.2$  but becomes more pronounced after another 0.4 time units for visualization purposes. Over time, vortices grow larger and stronger by drawing energy from the mean flow. Eventually, these structures break down into smaller, more chaotic forms, leading to fully developed turbulence. At  $t^* = 19.0$  (Figure 3.13(c)), the boundary layer remains non-turbulent, with visible characteristic roll-ups in the transitional region. However, early signs of turbulence, including disturbances in all three dimensions, are observed in a portion of the wake region at the same time instance.

A noteworthy observation is the correlation between streamwise fluid flow and the propagation of sound waves. Sound waves propagate both downstream and upstream through the domain, potentially influencing the flow field. In this specific case, trailing edge sound waves contribute to the bursting of the LSB, as visualized in Figure 3.14 and explained in the subsequent analysis.

As previously demonstrated, the recirculation zone is visible in Figure 3.12(c) at  $t^* = 14.0$ . By  $t^* = 14.5$ , the LSB is still present and has grown further, as shown in Figure 3.14(e). The figure's bottom panels (Figures 3.14(e) and (f)) illustrate streamlines, while the upper panels (Figures 3.14(a-d)) show sound wave propagation and its interaction with the fluid flow. For enhanced visualization and analysis, 400 snapshots were obtained throughout the 20 time-unit simulation period, providing 0.05 time-unit intervals between snapshots. This high-resolution temporal sampling, while computationally demanding in terms of memory, storage, and post-processing time, enables detailed observation of rapid flow phenomena. Several automated scripts were developed using Tecplot and Python, leveraging the PyTecplot tool, to streamline the entire process from simulation execution to final visualization, thereby facilitating comprehensive analysis of complex fluid flow characteristics.

For better understanding and visualization, a transparent dashed violet line with a violet

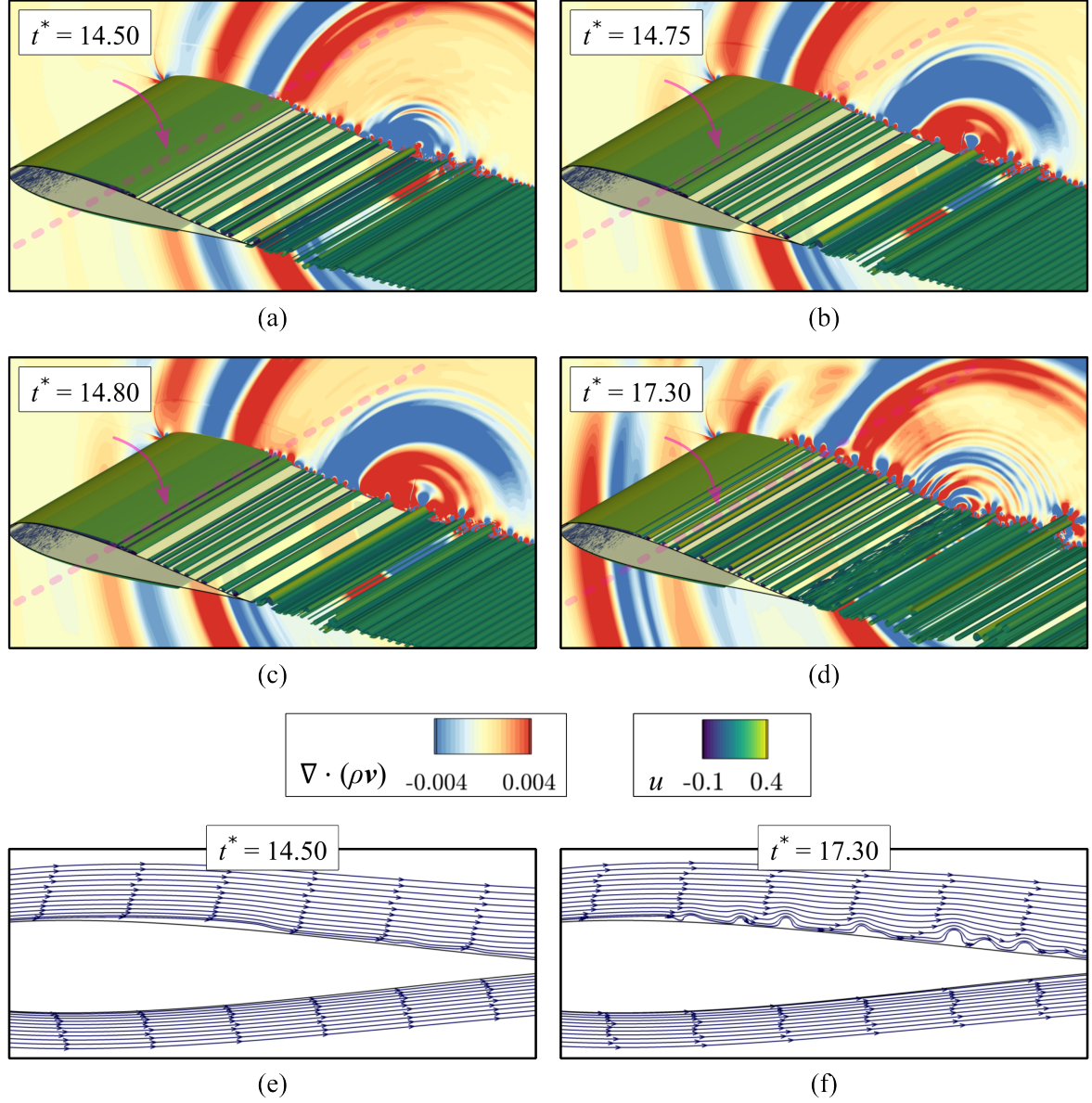


**Figure 3.14:** Formation and breakdown of the laminar separation bubble visualized using  $Q$ -criterion ( $Q = 0.01$ ), with sound wave propagation (a-d) and streamlines in a mid-plane cut (e-f) at different time instances. The transparent dashed violet line emphasizes the region of laminar separation bubble bursting.

arrow marks the exact spanwise position on the airfoil's surface where the LSB occurs. This marker is visible across all four snapshots starting at  $t^* = 14.5$ . This marking is added due to the LSB's limited visibility in Figure 3.14(a), although it can be observed at the same time step through the streamlined view in Figure 3.14(e). However, after 0.25 time units, changes beneath the marked transparent line become apparent. After just 0.05 time units later, it becomes even more evident that the LSB begins to burst. By  $t^* = 17.3$ , additional vortical structures have formed at the LSB's previous location, indicating its breakdown. The streamlined visualization

in Figures 3.14(e) and (f) confirms observations from  $Q$ -criterion iso-contours. Both visualizations highlight the LSB's significant inflation at  $t^* = 14.5$  and its subsequent breakdown by  $t^* = 17.3$ .

The critical question remains: why does the LSB break down? By combining the visualization of vortical structures through the  $Q$ -criterion with the mid-plane contour representing the divergence of density and velocity vector, which reveals instabilities in the domain observable as sound waves, the mechanism becomes clear. Closely examining Figures 3.14(a) and (b) reveals that the LSB begins to burst after the first trailing edge sound waves reach the spatial position where the LSB coincides. In Figure 3.14(a), it is visible that at  $t^* = 14.5$ , the first two pairs of trailing edge sound waves have just reached the position where the LSB occurs. At  $t^* = 14.75$  (Figure 3.14(b)), these sound waves pass by the LSB position, which starts to burst due to pressure disturbances produced by sound wave propagation originating from the trailing edge.

This analysis leads to the conclusion that trailing edge sound waves influence the fluid flow in the airfoil's boundary layer and are consequently responsible for the LSB's breakdown. The LSB formation represents a critical aerodynamic phenomenon that can significantly impact the performance of airfoils. If the flow fails to reattach downstream of the separation point, a complete stall condition may develop, severely degrading lift generation and increasing drag. In the present case, however, the acoustic-induced LSB breakdown actually facilitates flow reattachment, demonstrating the complex interplay between aerodynamic and aeroacoustic phenomena in unsteady airfoil flows.

Overall, this detailed examination of the PTE airfoil's post-acceleration phase provides essential insights into the coupling between boundary layer transition, laminar separation bubble dynamics, and acoustic wave propagation. These findings establish a comprehensive foundation for the comparative analysis with the STE airfoil presented in Section 3.4.

### **3.4 Comparative Analysis at $Re = 250,000$ : PTE vs. STE Airfoils**

This section presents a comparative analysis between the primary trailing edge airfoil data from Section 3.3 and the serrated trailing edge configuration. As a reminder, PTE represents the primary trailing edge configuration, while STE denotes the serrated trailing edge variant. The

airfoil geometry, except for the added serrations, remains identical and is fully defined in Section 3.2. Following the approach established in Section 3.3, the analysis begins with aerodynamic performance assessment through temporal force distribution examination.

The comparative methodology employed here follows established practices in airfoil performance evaluation, where baseline configurations are systematically compared against modified geometries to isolate the effects of specific design changes [82]. This approach enables the direct attribution of performance variations to the trailing edge modifications, while maintaining identical flow conditions and computational parameters for a Reynolds number of 250,000.

From Figure 3.15, it is evident that during the acceleration phase, no significant difference exists in the non-dimensional  $x$ -direction force ( $f_x^*$ ) between the PTE and STE airfoils. After approximately eight time units, corresponding to the transition from acceleration to constant velocity, the results begin to diverge, with the STE configuration exhibiting higher non-dimensional force in the  $x$ -direction, indicating increased drag. However, this difference diminishes over time, resulting in convergent values toward the end of the simulation period. Detailed quantification of force magnitudes is provided in Section 3.5, where force comparisons across various Reynolds numbers are presented. The following analysis aims to elucidate the underlying physical mechanisms responsible for these observed trends.

Decomposing the total force into pressure (Figure 3.15(b)) and skin friction (Figure 3.15(c)) components reveals that the pressure component exerts greater influence on overall force characteristics, consistent with the findings presented in Subsection 3.3.1. However, a significant increase in skin friction force has an adverse effect on the total force magnitude for the STE configuration. This behavior is theoretically expected, as serration addition increases the airfoil's surface area exposed to the fluid flow, consequently elevating friction drag. According to fundamental boundary layer theory, skin friction is directly proportional to the surface area and the local shear stress, where  $\tau_w = \mu \frac{\partial u}{\partial y} \big|_{y=0}$  [82]. Therefore, the increased surface area introduced by serrations inherently elevates the total friction drag component.

Additionally, serrations promote earlier boundary layer transition to turbulence, resulting in higher wall shear stresses within the turbulent boundary layer compared to the laminar state. This phenomenon occurs because turbulent boundary layers exhibit significantly higher momentum transfer rates near the wall, resulting in steeper velocity gradients and consequently higher shear stresses. Conversely, the pressure force component shows slight improvement for

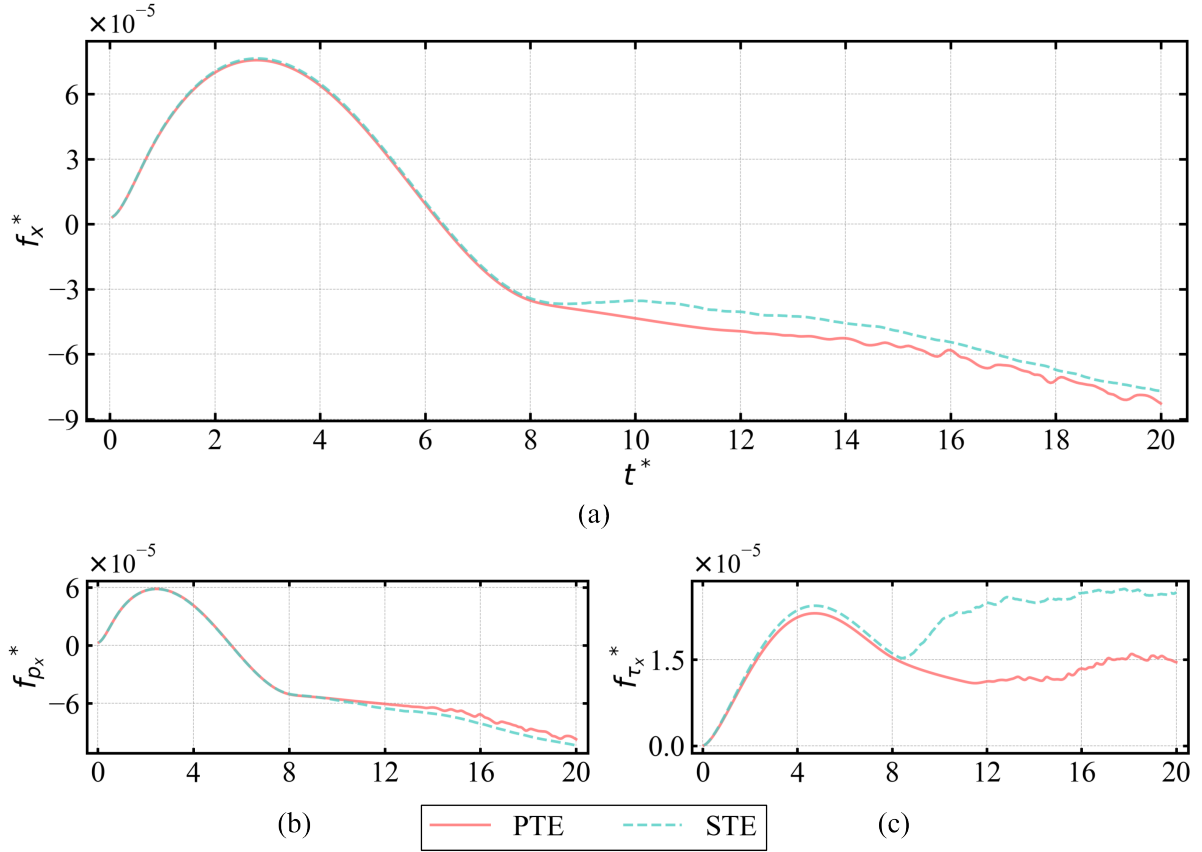


**Figure 3.15:** Temporal comparison of non-dimensional  $x$ -direction forces between PTE and STE airfoils: (a) total force magnitude, (b) pressure force component, and (c) skin friction force component. The divergence in performance becomes apparent after the acceleration phase concludes at  $t^* \approx 8$ .

the STE airfoil, though this enhancement is not universally observed across all operating conditions. Accordingly, most serrated trailing edge implementations are not designed primarily for aerodynamic improvement but rather for acoustic noise reduction. The primary mechanism underlying this noise reduction involves the disruption of coherent vortical structures at the trailing edge, nicely revealed in Figure 3.16(a) and (b), which are the dominant source of trailing edge noise generation [132].

Nevertheless, the observed pressure force improvement is attributed to the suppression of laminar separation bubble formation in the serrated trailing edge airfoil, where turbulent transition initiates earlier in the boundary layer development, as demonstrated in Figure 3.16.

Figure 3.16(a) illustrates the PTE airfoil configuration during the initial stages of LSB breakdown, consistent with the detailed analysis presented in Subsection 3.3.2. In contrast, the STE airfoil exhibits fully developed turbulent flow initiating at approximately one-quarter of the chord length from the leading edge (Figure 3.16(b)). This early transition to turbulence is a



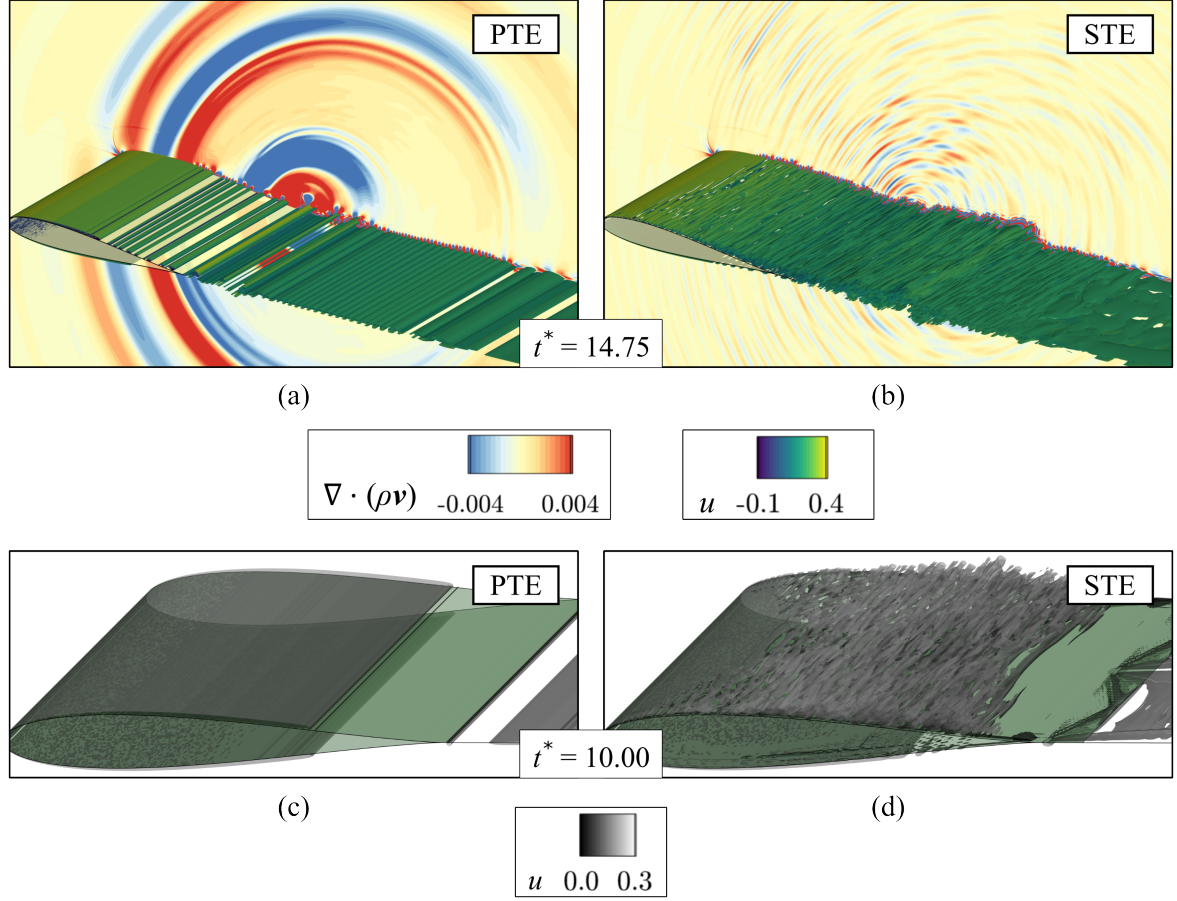


**Figure 3.16:** Comparative visualization of vortical structures and acoustic wave propagation for primary trailing edge (a,c) and serrated trailing edge (b,d) airfoils, demonstrating laminar separation bubble suppression through serration implementation.  $Q$ -criterion iso-surfaces ( $Q = 0.01$ ) are colored by streamwise velocity magnitude, while acoustic waves are visualized through divergence of density and velocity vector contours in the mid-plane.

fundamental characteristic of serrated trailing edges, which act as passive boundary layer transition devices by introducing three-dimensional flow disturbances that amplify boundary layer instabilities [131].

Turbulent transition in the STE configuration occurs significantly earlier than in the PTE case, as evidenced by comparing Figures 3.16(c) and 3.16(d). By the simulation midpoint, the boundary layer at mid-chord has achieved full turbulent development in the STE case, even before vortical structures reach the trailing edge. Conversely, the PTE airfoil remains in an extended transitional phase characterized by spanwise-coherent roll-up structures that have not yet achieved full three-dimensional turbulent development.

Regarding the wake region downstream of the trailing edge, the PTE configuration exhibits classical shear layer instability with characteristic two-dimensional roll-up structures, while

the entire wake region in the STE case demonstrates fully developed three-dimensional turbulent characteristics. This fundamental difference in wake structure directly impacts the acoustic signature of each configuration, as three-dimensional turbulent wakes generate broadband noise with lower peak amplitudes compared to the tonal noise components associated with two-dimensional coherent structures. These wave propagation patterns are clearly visualized in Figures 3.16(a) and (b), demonstrating that the STE airfoil configuration generates reduced acoustic intensity. The serrations fragment larger vortices into smaller structures, thereby reducing trailing edge noise, which represents the most significant acoustic source in this flow regime. However, detailed noise reduction quantification is not pursued in this analysis, as extensive research has already addressed this topic [70, 133, 134].

The non-dimensional force in the  $y$ -direction exhibits generally similar temporal evolution for both PTE and STE airfoils, as illustrated in Figure 3.17. However, differences during the acceleration phase between PTE and STE  $f_y^*$  values are visually more pronounced than those observed in the  $x$ -direction force comparison. In this case,  $f_y^*$  demonstrates higher magnitudes for the STE airfoil, providing a slight performance advantage for this configuration. Upon decomposing  $f_y^*$  into pressure and skin friction components, the analysis confirms, as previously established through Figure 3.7(b), that the skin friction component remains negligible. Therefore, despite a visibly pronounced reduction in the skin friction component for the STE configuration, shown in Figure 3.17(c), the overall effect on  $f_y^*$  remains minimal. This negligible impact becomes apparent when examining the component magnitudes, which are displayed on the order of  $10^{-6}$ , several orders of magnitude smaller than the pressure component.

Examining the overall  $y$ -direction force during the post-acceleration phase reveals a sudden decrease for the STE case around  $t^* = 12$ , while the PTE configuration begins oscillating approximately one to two time units later. Therefore, evaluating performance solely based on final lift values or time-averaged quantities over specific intervals fails to capture the broader insight regarding airfoil stability improvements introduced by serration implementation. Consequently, the post-acceleration phase receives further detailed examination through the focused analysis presented in Figure 3.18(a), beginning from  $t^* = 8.0$ .

The most significant difference manifests during the final third of the simulation period, where the STE curve exhibits characteristics resembling a regression line that smooths the volatile PTE data fluctuations. This stability enhancement represents a critical aerodynamic



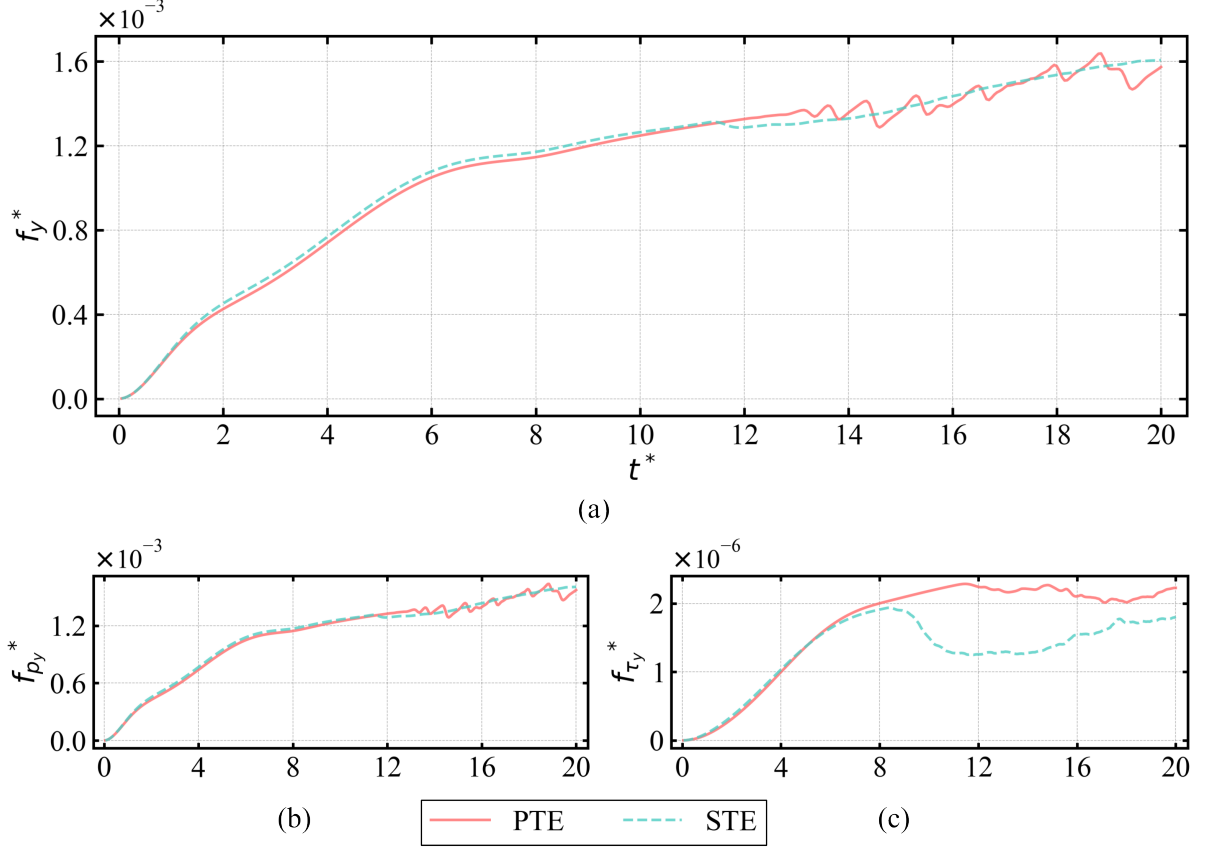


**Figure 3.17:** Temporal comparison of non-dimensional y-direction forces between PTE and STE airfoils: (a) total force magnitude, (b) pressure force component, and (c) skin friction force component.

advantage, particularly for applications requiring consistent lift generation, such as small aircraft and unmanned aerial vehicles operating at moderate Reynolds numbers [135]. The key mechanism in enhancing airfoil stability involves controlling boundary layer development and, critically, managing boundary layer transition processes. Through serration implementation, the trailing edge noise generation phase initiates earlier, as emphasized by the highlighted curve portions in Figure 3.18(a), where red and teal arrows indicate the transition from steadily increasing force to a sudden decrease before resuming the upward trend. The trailing edge noise source is visualized in Figures 3.18(b) and 3.18(c) through acoustic wave contour plots, though the noise generation realistically commences slightly earlier: approximately  $t^* = 13.4$  for the PTE airfoil and  $t^* = 11.5$  for the STE configuration.

The earlier onset of trailing edge noise in the STE configuration paradoxically contributes to improved stability by establishing consistent turbulent flow characteristics sooner in the development process. This early stabilization prevents the formation of large-scale unsteady flow

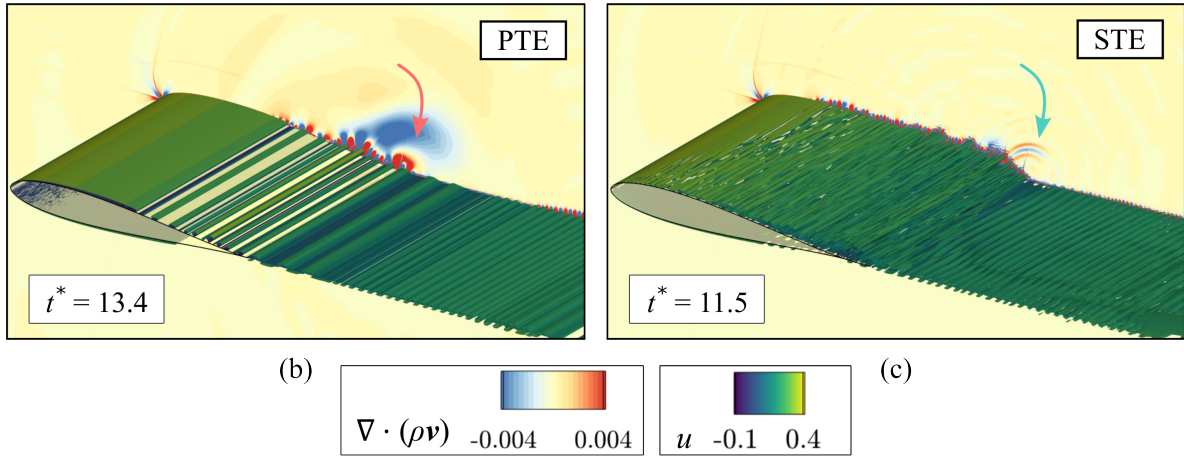
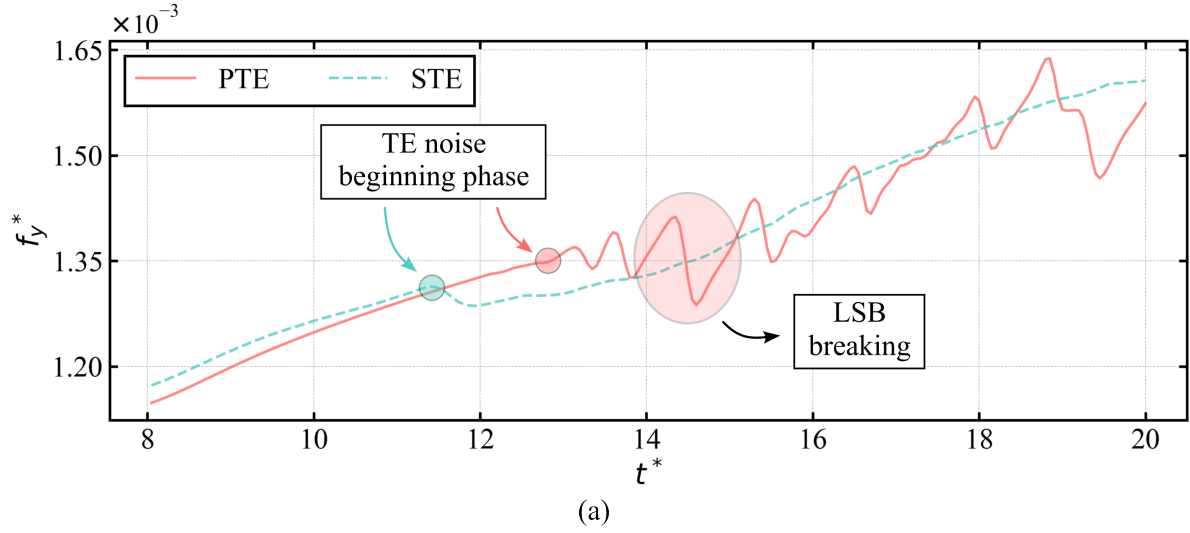


**Figure 3.18:** Detailed analysis of post-acceleration aerodynamic behavior: (a) temporal evolution of non-dimensional y-direction force during constant velocity operation, highlighting stability differences between configurations; (b,c) comparative visualization of trailing edge noise onset through acoustic wave contour plots, demonstrating earlier noise generation in the STE configuration at  $t^* = 11.5$  versus  $t^* = 13.4$  for the PTE airfoil.

structures that characterize the laminar separation bubble phenomenon, which is primarily responsible for the higher volatility observed in the PTE airfoil performance (Figure 3.18(a)).

To further demonstrate LSB avoidance, classical pressure coefficient distributions are presented in Figure 3.19(a), with  $C_p$  values averaged over the time interval from  $t^* = 14$  to  $t^* = 16$ . This temporal range strategically captures the formation, growth, and bursting phases of the LSB phenomenon. The time-averaged pressure coefficient distribution provides a clear indication of LSB presence through the characteristic plateau in the  $C_p$  curve, which corresponds to the recirculation zone where flow velocity approaches zero.

In addition to the time-averaged  $C_p$  distribution shown in Figure 3.19(a), Figures 3.19(b) and (c) highlight the temporal differences in surface pressure distributions. The instantaneous

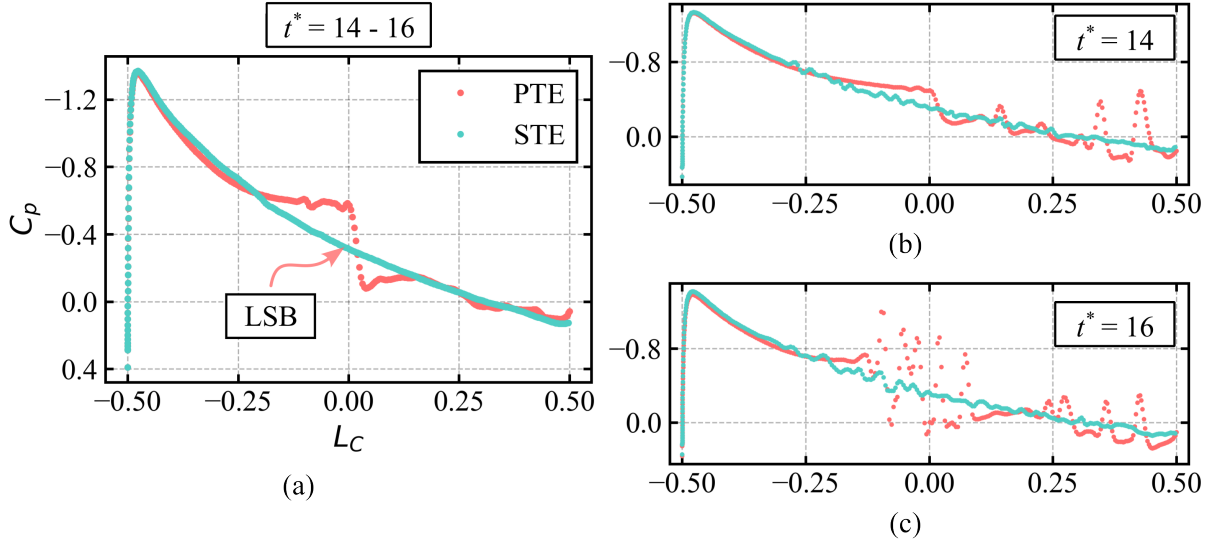


**Figure 3.19:** Pressure coefficient comparison between PTE (red dots) and STE (teal dots) configurations: (a) time-averaged  $C_p$  distribution over the interval  $t^* = 14$  to  $t^* = 16$ , demonstrating the absence of characteristic laminar separation bubble features in the STE case; (b,c) instantaneous pressure distributions at  $t^* = 14$  and  $t^* = 16$ , respectively, highlighting the reduced oscillatory behavior in the STE configuration.

pressure coefficient plots consistently demonstrate that the PTE airfoil boundary layer exhibits significantly higher oscillatory behavior compared to the more stable STE configuration. The scatter in the PTE pressure data reflects the unsteady nature of the laminar separation bubble, which undergoes periodic growth and bursting cycles that directly contribute to force oscillations.

As demonstrated throughout this section, the PTE airfoil exhibits substantially higher volatility compared to the STE configuration. Based on the comprehensive data analysis for Reynolds number 250,000, the STE airfoil demonstrates superior boundary layer stability and enhanced overall aerodynamic stability while simultaneously achieving trailing edge noise reduction from an aeroacoustic perspective. These findings align with the fundamental understanding that passive flow control devices, such as trailing edge serrations, can simultaneously address multiple aerodynamic challenges by manipulating boundary layer transition characteristics [136]. The trade-off between slightly increased friction drag and improved stability, combined with significant noise reduction benefits, makes serrated trailing edges particularly attractive for applications where acoustic signatures are critical, such as wind turbines and unmanned aerial vehicles [53].

### 3.5 Multi-Reynolds Number Analysis: PTE vs. STE Performance Comparison

This section extends the analysis of PTE and STE cases at  $Re = 250,000$  to include three additional Reynolds numbers:  $Re = 100,000$ ,  $400,000$ , and  $500,000$ . Reynolds number, defined as  $Re = \rho UL/\mu$ , quantifies the ratio of inertial to viscous forces and serves as a fundamental parameter governing boundary layer development, transition mechanisms, and flow stability. The aim is to examine how variations in Reynolds number influence the onset of trailing edge noise, the initiation of turbulent boundary layer, and overall airfoil performance through a comparison between PTE and STE configurations (Subsection 3.5.1). Additionally, more detailed aeroacoustic quantification between the cases is obtained (Subsection 3.5.2). This parametric study is particularly relevant for applications in the moderate Reynolds number regime, where boundary layer transition phenomena significantly influence both aerodynamic performance and acoustic signatures. Collectively, this section focuses on elucidating and highlighting the differences between PTE and STE airfoils through a detailed examination of the underlying physical phenomena.

#### 3.5.1 Force Characteristics and Boundary Layer Transition Analysis

Before introducing the comparison between PTE and STE configurations across various Reynolds numbers, a preliminary analysis examining only PTE airfoil noise occurrences is presented for different Reynolds numbers. The non-dimensional force in the y-direction is shown in Figure 3.20 to facilitate comparison between cases and highlight oscillations occurring in the simulation's second half ( $t^* > 10$ ). A characteristic feature of all four Reynolds number cases is the presence of strong oscillations that become more pronounced at lower Reynolds numbers. This behavior is attributed to the inverse relationship between Reynolds number and laminar boundary layer thickness, resulting in thicker, more unstable laminar regions at lower Reynolds numbers [82]. However, it is essential to emphasize that this observation applies specifically to the examined range of Reynolds numbers between 100,000 and 500,000, for this study. Conversely, oscillations commence earlier at higher Reynolds values, indicating the earlier onset of trailing edge noise generation.

Figure 3.20(a) clearly demonstrates the initial deviations from constant  $f_y^*$  growth, indicating disturbances and the influence of trailing edge noise on boundary layer behavior and,

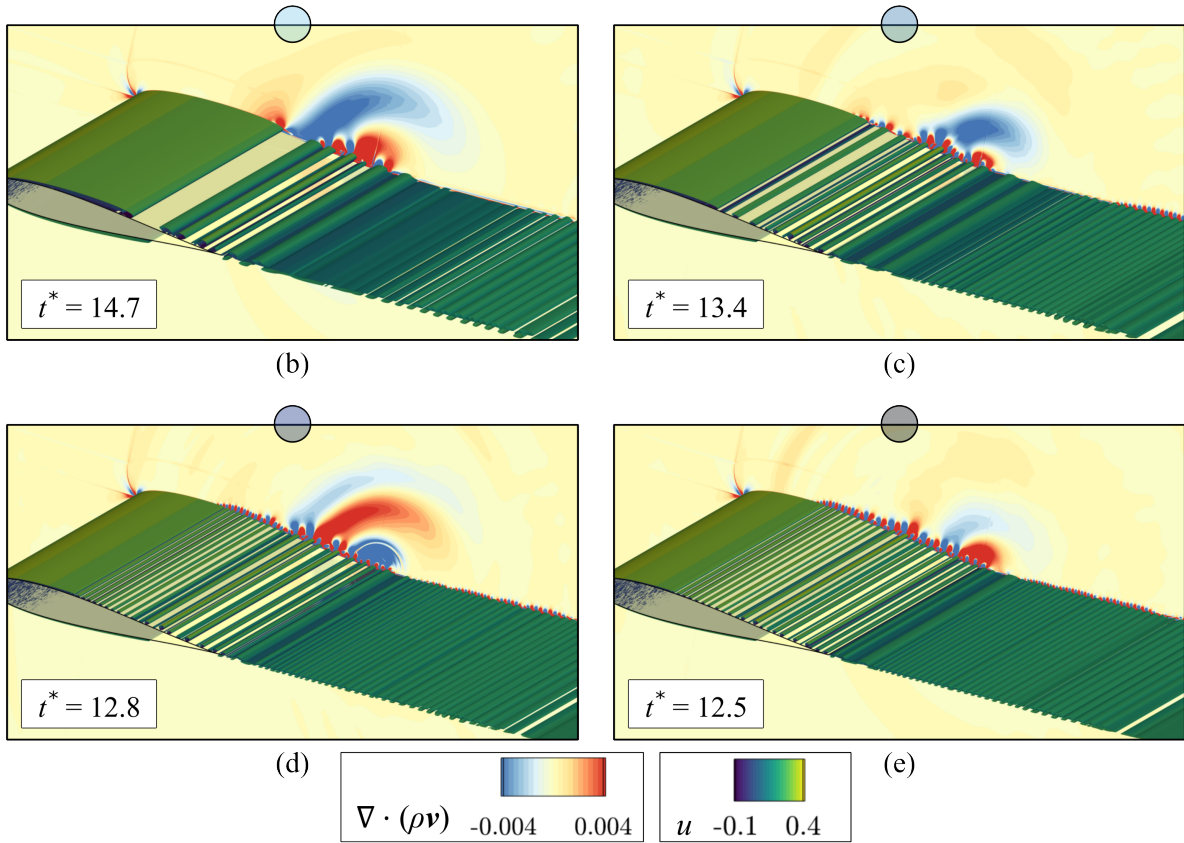
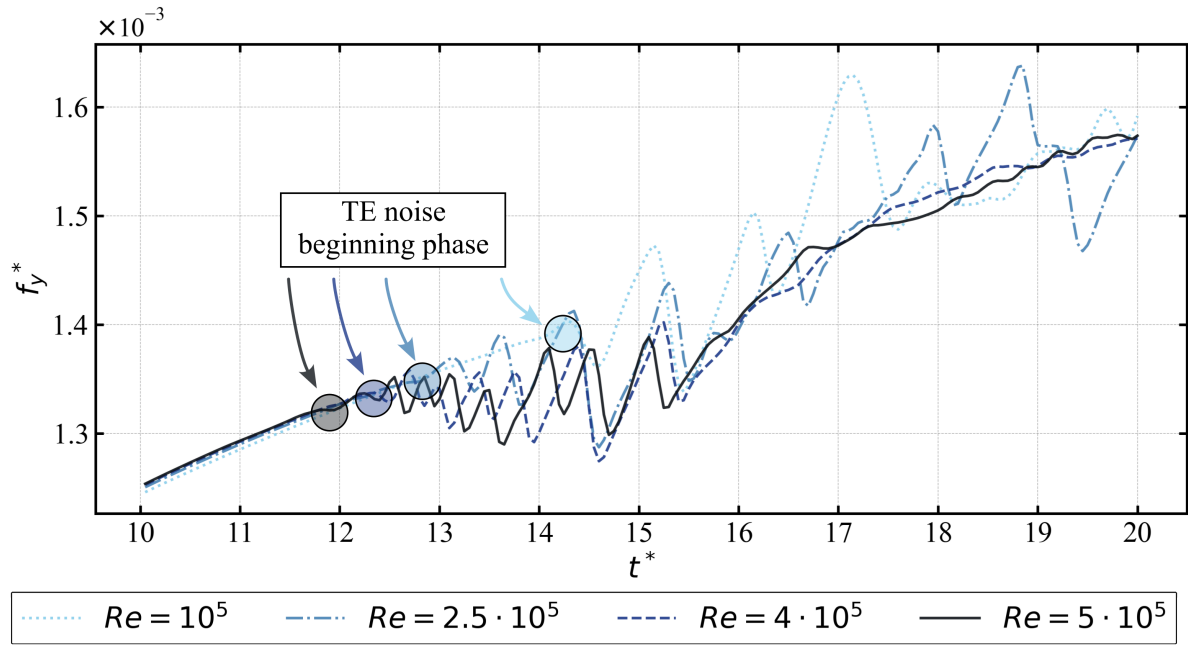


**Figure 3.20:** PTE airfoil trailing edge sound wave occurrence visualization for various Reynolds numbers: (a)  $f_y^*$  versus  $t^*$  graph with emphasized oscillations and trailing edge noise onset phases highlighted by transparent circles colored with blue palette; (b-e) sound wave contour plots and iso-surfaces at emphasized time steps, where each subfigure corresponds to the circle colors for respective Reynolds number cases.

consequently, aerodynamic performance. The transparent circles in Figure 3.20(a) highlight the moment of trailing edge noise occurrence for each Reynolds number case, distinguished by four different blue palette colors and line styles. These markers are validated in Figures 3.20(b), (c), (d), and (e), which employ the aforementioned visualization approach to display sound waves on mid-plane contours with iso-surfaces. Figure 3.20(b) shows the latest occurrence of sound waves at  $t^* \approx 14.7$ . As mentioned in Section 3.4 and demonstrated in Figure 3.18, the time steps visualized with contour plots and iso-surfaces precede the actual situation shown in the graphs by several time units. This temporal offset ensures clear visualization of sound waves, compensating for low visibility effects at the initial stages of the trailing edge noise phase. Figures 3.20(c), (d), and (e) demonstrate progressively earlier trailing edge sound wave generation and earlier boundary layer transformation from laminar to transitional phases. Beyond the earlier transition, larger portions of the airfoil surface experience boundary layer transition, with roll-up structures becoming visible closer to the leading edge as the Reynolds number increases.

Based on the preceding analysis, the STE airfoil is introduced for comparison with the PTE configuration across four Reynolds numbers. Non-dimensional y-direction force values during the post-acceleration period are presented in Figure 3.21. Although the comparison between PTE and STE at  $Re = 250,000$  has been previously presented, it is included here for enhanced comparison with other Reynolds number cases. Results demonstrate similar serration benefits for the three additional cases as observed in Figure 3.18 and repeated in Figure 3.21(b). Serration implementation results in smoother force curves, indicating improved stability and more reliable airfoil control. The smoothing effect arises from serrations' ability to promote earlier boundary layer transition, thereby suppressing large-scale unsteady flow structures associated with laminar separation bubbles. Furthermore, higher Reynolds number values demonstrate even greater benefits due to improved overall  $f_y^*$  values compared to the PTE airfoil.

Nevertheless, the sudden performance decline initiates earlier for the STE airfoil, followed by superior recovery with more controlled growth. The cause of this sudden performance decline stems from boundary layer vortices arriving at the airfoil's trailing edge, generating sound waves that propagate through the domain and induce additional disturbances on the suction side boundary layer. These moments of trailing edge sound wave initiation are highlighted with red and teal transparent circles in Figure 3.21. The earlier onset in the STE case paradoxically contributes to improved long-term stability by establishing consistent turbulent flow characteristics sooner, preventing the formation of large-scale unsteady structures.

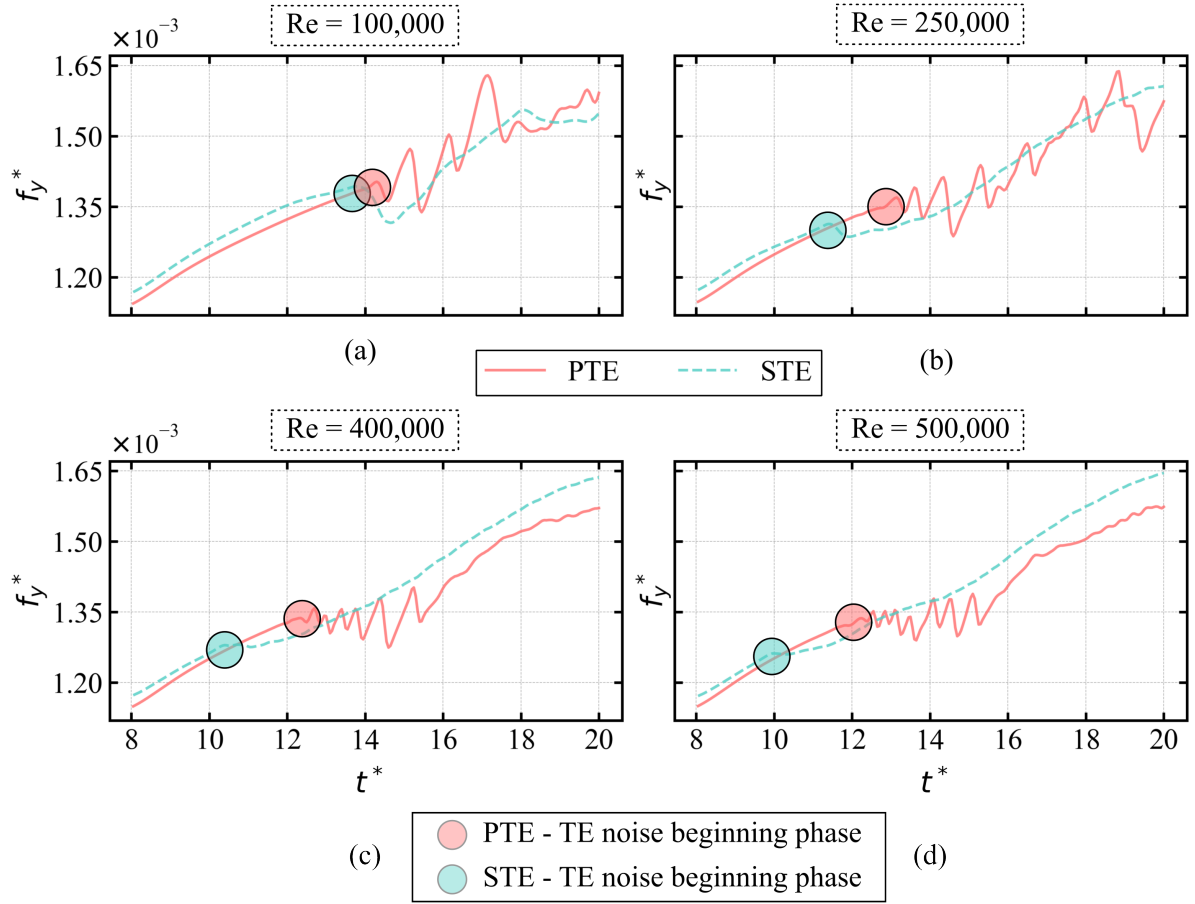


**Figure 3.21:** Comparison of non-dimensional y-direction forces for PTE (red) and STE (teal) airfoils across four Reynolds numbers: (a)  $Re = 100,000$ , (b)  $Re = 250,000$ , (c)  $Re = 400,000$ , and (d)  $Re = 500,000$ . Red (PTE) and teal (STE) circles highlight the onset of trailing edge sound wave propagation.

Furthermore, increasing the Reynolds number results in a larger temporal gap between the initiation of sound wave generation at the trailing edge for PTE and STE configurations. Explanation of those changes can be given through Figure 3.22, which presents non-dimensional  $x$ -direction forces for the four Reynolds number cases. The graphs appear on the left side of each subfigure, while the right side displays airfoil snapshots at different time steps corresponding to the period emphasized by teal arrows on the left. This period shows sudden  $f_x^*$  growth for the STE airfoil compared to the PTE configuration, attributed to earlier laminar-to-turbulent boundary layer transition. As visible on the right side of these subfigures, at identical time steps for each Reynolds number case, the STE configuration demonstrates the moment when the turbulent boundary layer transition commences. At the same time, the PTE airfoil maintains a laminar boundary layer for Reynolds numbers of 250,000 (Figure 3.22(b)), 400,000 (Figure 3.22(c)), and 500,000 (Figure 3.22(d)), or exhibits a transitional region with roll-ups for



Reynolds number 100,000 (Figure 3.22(a)).

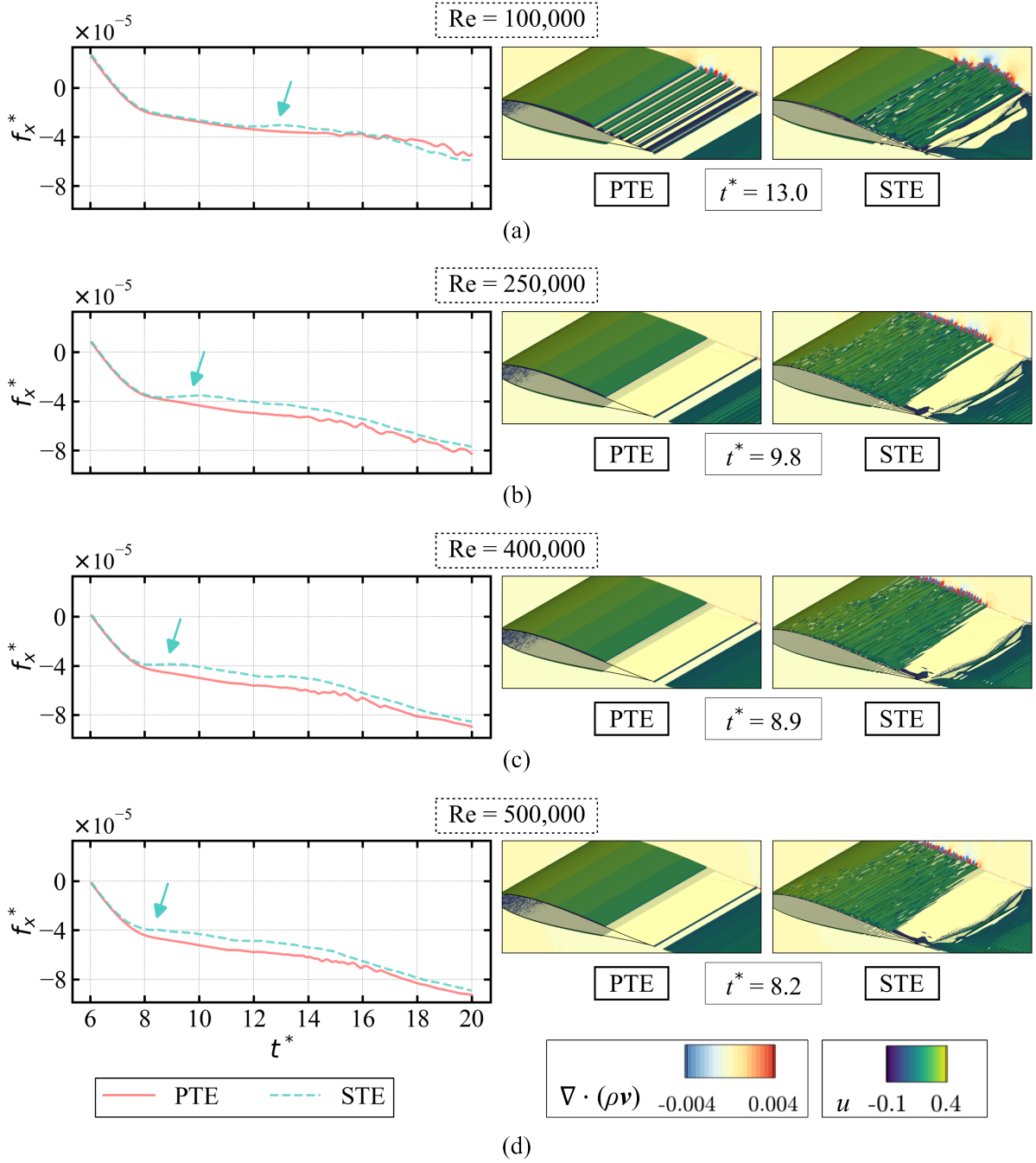


**Figure 3.22:** Comparison of non-dimensional  $x$ -direction forces for PTE (red) and STE (teal) airfoils with corresponding flow visualizations. Teal arrows highlight the turbulent boundary layer initiation phase for the STE airfoil. Four Reynolds number cases are presented: (a)  $Re = 100,000$ , (b)  $Re = 250,000$ , (c)  $Re = 400,000$ , and (d)  $Re = 500,000$ . The left legends apply to force plots, while the right legends correspond to flow visualization contours.

Regarding force analysis comparison,  $f_x^*$  exhibits the smallest difference between PTE and STE airfoils at Reynolds number 100,000, as visible in Figure 3.22(a). The PTE configuration actually outperforms the STE airfoil during the final three time units. The other three cases



demonstrate similar  $f_x^*$  trends with more stable curves but slightly degraded performance. To quantify differences in both  $f_x^*$  and  $f_y^*$ , Table 3.2 is introduced, showing the relative difference between PTE and STE forces averaged over the post-acceleration phase and the final five time units. The relative difference for  $x$ - and  $y$ -direction forces is calculated using Equations 3.8 and 3.9:

$$\epsilon_x = \frac{\overline{f_{x\ PTE}^*} - \overline{f_{x\ STE}^*}}{\overline{f_{x\ PTE}^*}} \cdot 100 [\%] \quad (3.8)$$

$$\epsilon_y = \frac{\overline{f_{y\ PTE}^*} - \overline{f_{y\ STE}^*}}{\overline{f_{y\ PTE}^*}} \cdot 100 [\%] \quad (3.9)$$

where all forces are averaged over time intervals from  $t^* = 8$  to  $t^* = 20$  or from  $t^* = 15$  to  $t^* = 20$ . Therefore, positive relative difference values indicate higher PTE forces relative to STE, and vice versa.

**Table 3.2:** Relative difference in mean non-dimensional forces in the  $x$ - and  $y$ -directions between the PTE and STE airfoils for four Reynolds numbers.

$Re \ [ \cdot 10^5 ]$	$t^* = 8 - 20$		$t^* = 15 - 20$	
	$\epsilon_x [\%]$	$\epsilon_y [\%]$	$\epsilon_x [\%]$	$\epsilon_y [\%]$
1	1.15	0.16	-5.51	1.54
2.5	12.65	-0.27	7.96	-1.1
4	12.52	-2.07	7.29	-3.72
5	11.35	-2.28	5.93	-4.05

Combining the  $f_x^*$  analysis from Figure 3.22 with force quantification from Table 3.2, it becomes evident that  $f_x^*$  improves slightly for the lowest Reynolds number. At the same time, the other three cases demonstrate approximately 12% degradation, primarily due to earlier turbulent boundary layer transition. This trade-off reflects the fundamental aerodynamic principle that turbulent boundary layers exhibit higher skin friction values compared to laminar layers. Nevertheless,  $f_x^*$  maintains relatively low values throughout the acceleration and short post-acceleration phases. The primary objective of this analysis is to capture, analyze, and explain specific physical phenomena and their manifestation in aerodynamic trends, rather than solely assessing force magnitudes.

Conversely,  $f_y^*$  shows negligible changes for Reynolds numbers 100,000 and 250,000, with slight deterioration and improvement, respectively. For higher Reynolds numbers, the difference becomes more pronounced, with values around 2% for the post-acceleration phase that

double when averaged over the final five time units. These values alone do not guarantee performance improvement; rather, a comprehensive analysis reveals that serrations enhance boundary layer stability, resulting in smoother force curves in both the  $x$ - and  $y$ -directions. Overall, conclusions drawn from the  $Re = 250,000$  case, where serrations improve boundary layer stability, extend to the broader Reynolds number range of 100,000–500,000.

### 3.5.2 Aeroacoustic Analysis and Noise Reduction Quantification

For the aeroacoustic analysis, 26 pressure measurement points are positioned in the airfoil's  $xy$  mid-plane with high-density data sampling at 3289 time steps over the complete 20-time-unit simulation duration. This sampling frequency and spatial distribution follow established practices in computational aeroacoustics, ensuring adequate temporal resolution to capture the frequency content of trailing edge noise while providing sufficient spatial coverage for directivity analysis [132]. The precise locations of these measurement points replicate microphone positioning in anechoic chamber experiments, where sensors are distributed radially around the noise source. Similarly, in this CFD analysis, 26 measurement points are distributed around the airfoil's trailing edge at a radial distance equal to one chord length, with angular positions ranging from  $30^\circ$  to  $150^\circ$  for the upper surface and  $210^\circ$  to  $330^\circ$  for the lower surface, as illustrated in Figure 3.23.

The one-chord-length radial distance represents a compromise between near-field accuracy and far-field applicability, positioning the measurement points within the geometric near-field while avoiding the fluid dynamic near-field where acoustic and vortical disturbances are coupled. Such dense spatial sampling enables detailed analysis of pressure fluctuations around the airfoil, capturing numerical differences between PTE and STE configurations across various Reynolds numbers, complementing the flow visualization interpretations obtained previously. The coordinate system referenced in Section 3.2 positions the airfoil and measurement points in the Cartesian system  $x_j = \{x, y, z\}$ , while the fluid flow is angled  $5^\circ$  to the Cartesian system, and it is measured in a generalized coordinate system  $\xi_i = \{\xi, \eta, \zeta\}$ . The measurement point at  $150^\circ$  is highlighted with a red circle because it exhibits the highest overall non-dimensional pressure ( $p^*$ ) and noise levels. Therefore, this location is examined in detail in the following figures, starting with Figure 3.24.

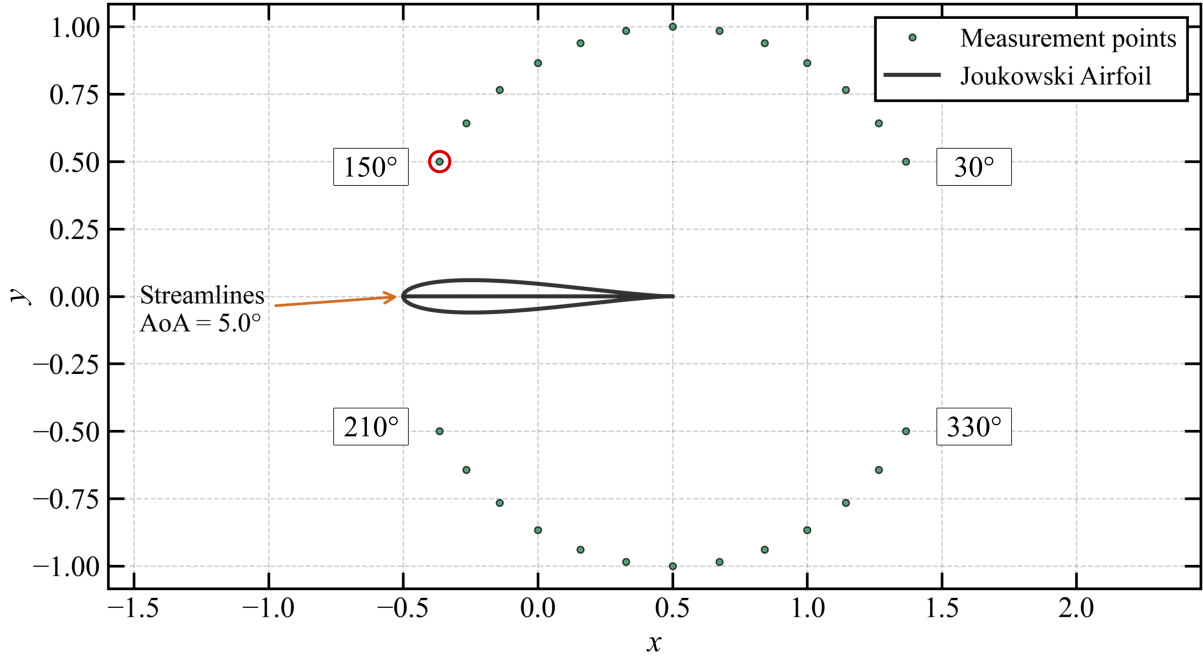


**Figure 3.23:** Measurement point locations around the Joukowski airfoil (green circles) with fluid flow direction indicated by the brown arrow. The red circle highlights the measurement point at  $150^\circ$  that receives detailed analysis in subsequent figures.

Examining all four Reynolds number cases reveals no pressure differences during the acceleration phase. Therefore, the transparent gray rectangles in the upper panels of Figures 3.24(a)-(d) are magnified in the lower panels, where interesting oscillations begin to manifest. As previously explained, the transition from a laminar boundary layer to a transitional period (PTE) or directly to a turbulent boundary layer (STE) introduces vortical structures that generate sound waves upon reaching the airfoil's trailing edge. Depending on the Reynolds number, these boundary layer changes occur earlier but persist for shorter durations at higher  $Re$ , and vice versa for lower  $Re$ . All four cases in Figure 3.24 show the magnified second half of the simulation, emphasizing non-dimensional pressure oscillations at a point located one chord length from the trailing edge at a  $150^\circ$  angle, highlighted by the red circle in Figure 3.23. Visual inspection reveals that oscillations commence around  $t^* \approx 15$  for  $Re = 100,000$ ,  $t^* \approx 14$  for  $Re = 250,000$ , and approximately  $t^* \approx 13$  for both  $Re = 400,000$  and  $Re = 500,000$ . This Reynolds number dependence reflects the enhanced convective transport and reduced diffusion at higher  $Re$ , enabling faster propagation of boundary layer disturbances to the trailing edge. Consequently, Sound Pressure Level (SPL) analyses visualized in Figures 3.25 and 3.26 are computed for time intervals  $t \in [15, 20]$  for  $Re = 1 \cdot 10^5$ ,  $t \in [14, 20]$  for  $Re = 2.5 \cdot 10^5$ , and  $t \in [13, 17]$  for  $Re = 4 \cdot 10^5$  and  $Re = 5 \cdot 10^5$ , as highlighted by the transparent purple regions in

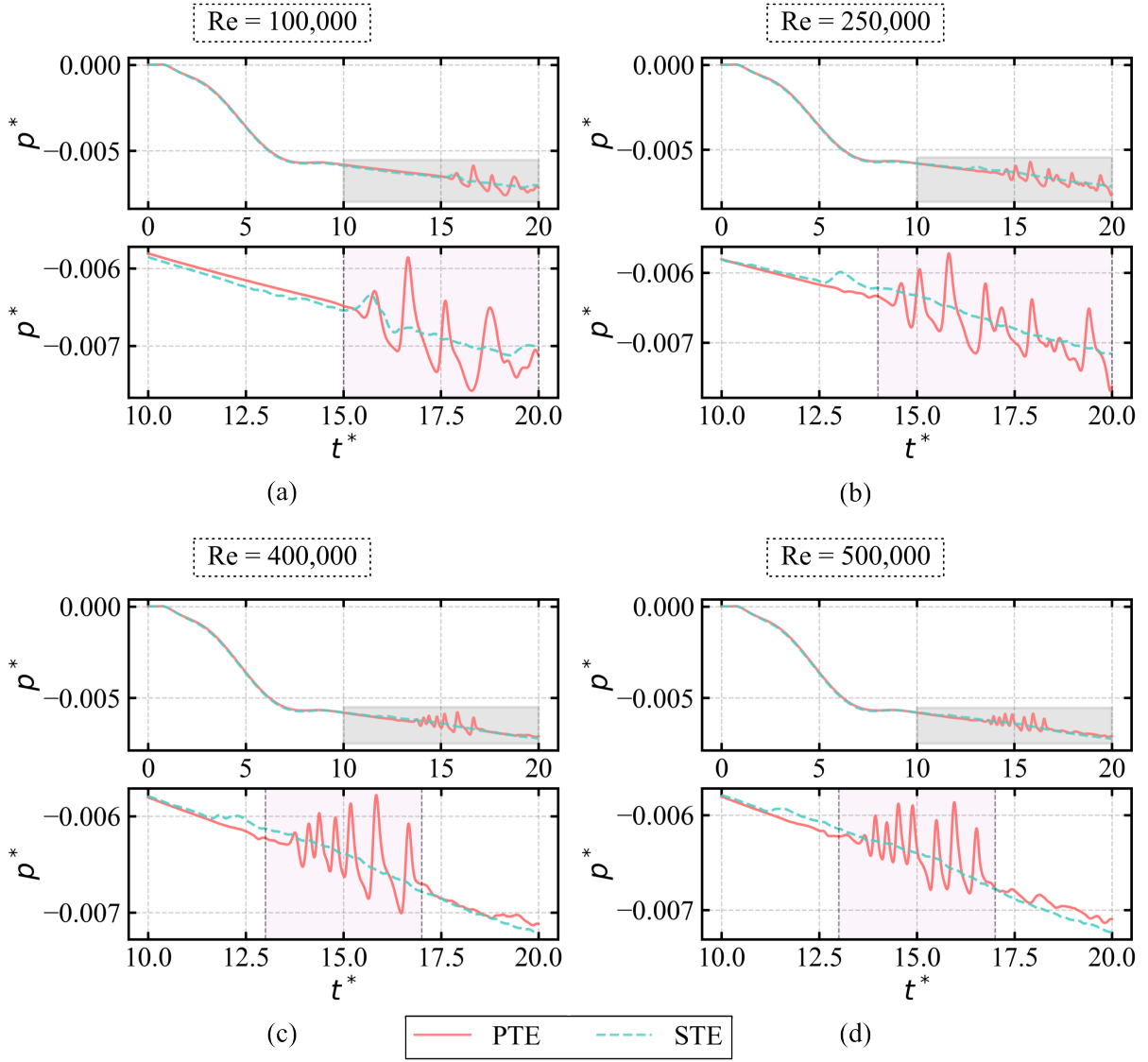


**Figure 3.24:** Non-dimensional pressure fluctuations for the measurement point at the  $150^\circ$  angle from the trailing edge for Reynolds numbers: (a) 100,000, (b) 250,000, (c) 400,000, and (d) 500,000. PTE curves are shown in red, while STE curves are shown in teal. Upper panels represent the complete simulation duration, while the gray rectangles indicate the zoomed regions displayed in the lower panels. The transparent purple region highlights the time period analyzed in subsequent figures.

the lower panels of Figure 3.24.

Based on pressure oscillations, SPL values are calculated for the aforementioned time intervals. Since pressure is obtained in non-dimensional form, all components in the SPL calculation must be non-dimensional to yield dimensionally consistent decibel values. The process begins with acquiring pressure time series data  $p^*(x_i, t)$  at  $N_p = 26$  discrete spatial locations  $x_i$  distributed around the trailing edge geometry, where the asterisk denotes non-dimensional quantities. The fundamental step in acoustic post-processing involves computing root-mean-square

(RMS) pressure values at each measurement location. The RMS calculation isolates the fluctuating acoustic pressure from the mean flow pressure, following the standard approach in aeroacoustics where only the unsteady pressure components contribute to sound generation [137]. For a given spatial point  $x_i$ , the non-dimensional RMS pressure is calculated as:

$$p_{\text{rms}}^*(x_i) = \sqrt{\frac{1}{N_t} \sum_{j=1}^{N_t} [p^*(x_i, t_j) - \overline{p^*}(x_i)]^2} \quad (3.10)$$

where  $N_t$  represents the total number of temporal samples,  $t_j$  denotes discrete time instances, and  $\overline{p^*}(x_i)$  is the temporal non-dimensional mean pressure at location  $x_i$ . This formulation effectively isolates the fluctuating pressure component, which contains acoustic information, from the time-averaged fluid dynamic pressure field. The temporal averaging window contains sufficient data with 564 sample points for  $Re = 1 \cdot 10^5$ , 678 for  $Re = 2.5 \cdot 10^5$ , 661 for  $Re = 4 \cdot 10^5$ , and 662 for  $Re = 5 \cdot 10^5$ .

The conversion to Sound Pressure Level follows the standard acoustic definition, adapted for non-dimensional analysis:

$$\text{SPL}(x_i) = 20 \log_{10} \left( \frac{p_{\text{rms}}^*(x_i)}{p_{\text{ref}}^*} \right) \quad [\text{dB}] \quad (3.11)$$

where  $p_{\text{ref}}^*$  represents the non-dimensional reference pressure corresponding to the standard acoustic reference of  $20 \cdot 10^{-6}$  Pa. The division of non-dimensional values under the logarithm ensures the SPL calculation remains dimensionally consistent, making this approach suitable and practically convenient. The logarithmic scale in SPL calculation compresses the wide dynamic range of acoustic pressures into a manageable scale, consistent with human auditory perception and standard acoustic measurement practices [137]. The resulting  $\text{SPL}(x_i)$  are effectively visualized in polar coordinates  $(r_i, \theta_i)$ , where  $r_i = \|x_i - x_{\text{TE}}\|$  represents the distance from the trailing edge location  $x_{\text{TE}}$  (equal to the chord length  $c^*$ ), and  $\theta_i = \arctan \left( \frac{y_i - y_{\text{TE}}}{x_i - x_{\text{TE}}} \right)$  defines the angular position. This polar representation provides valuable insight into the directional characteristics of trailing edge noise radiation and facilitates comparison between PTE and STE acoustic scattering from sharp edges.

Based on these calculations, four polar plots are presented in Figures 3.25 and 3.26. All cases contribute to the unified conclusion that serrations improve pressure fluctuations and reduce sound pressure levels in these regions by up to 8 dB. Overall, SPL intensity values for the

PTE airfoil are consistent with those reported in the literature [138, 139]. Beyond visual representation, Tables 3.3 and 3.4 provide quantification and statistical analysis of sound values.

By combining statistical and visual data, several observations emerge. First, for Reynolds number 100,000, the greatest improvements from serration implementation occur at the highest SPL values, while minimal benefits are achieved at the lowest sound intensities. Additionally, the upper surface exhibits more significant improvements with a mean of 4.00 dB compared to 3.34 dB for the lower surface. More importantly, the highest SPL on the upper surface is reduced by 5.92 dB from its original value of 78.69 dB. Consequently, instead of the maximum SPL occurring at  $150^\circ$  as in the PTE case, the STE case exhibits its maximum at  $210^\circ$  due to lower noise reduction on the lower surface compared to the upper surface. This directivity shift reflects the altered scattering characteristics introduced by serrations, which modify the coherence length of turbulent structures interacting with the trailing edge.

At  $Re = 250,000$ , the situation differs slightly, with higher improvements for lower-intensity SPL measurement points, while reductions decrease at positions with increased sound levels. Therefore, at the PTE's  $150^\circ$  position with the highest SPL of 78.59 dB, only a 2.30 dB reduction is achieved. However, the overall reduction is approximately 5.01 dB, which exceeds that of the previous case with a lower Reynolds number. Compared to the lower Reynolds number case, the reduction influence shifts from the upper to the lower surface. Quantitatively, the upper surface mean reduction is 4.75 dB, while the lower surface achieves 5.27 dB with a higher reduction even in the higher SPL regions compared to the upper surface. The Reynolds number dependency in serration effectiveness is related to the changing scales of turbulent structures in the boundary layer, which affects the interaction between eddies and the serrated geometry.

For  $Re = 400,000$  and  $Re = 500,000$  (Figure 3.26), the situation resembles the previous  $Re = 250,000$  case but with a more pronounced reduction across all regions. However, the time interval of interest is shorter for these two cases ( $t \in [13, 17]$ ) compared to those in Figure 3.25. Nevertheless, significant noise reduction is achieved through the addition of serration. For the  $Re = 400,000$  case, the overall reduction is 5.29 dB, while for  $Re = 500,000$ , it reaches 6.24 dB. In these two cases, greater reduction is again achieved on the upper surface compared to the lower surface, with means of 5.55 dB versus 5.03 dB and 6.51 dB versus 5.97 dB for the higher and lower Reynolds values, respectively.

Interestingly, for the STE case in both Figures 3.25(a) and (b), minimum SPL occurs at  $330^\circ$ , while for Figures 3.26(a) and (b), the minimum occurs at  $30^\circ$ . Consequently, minimum

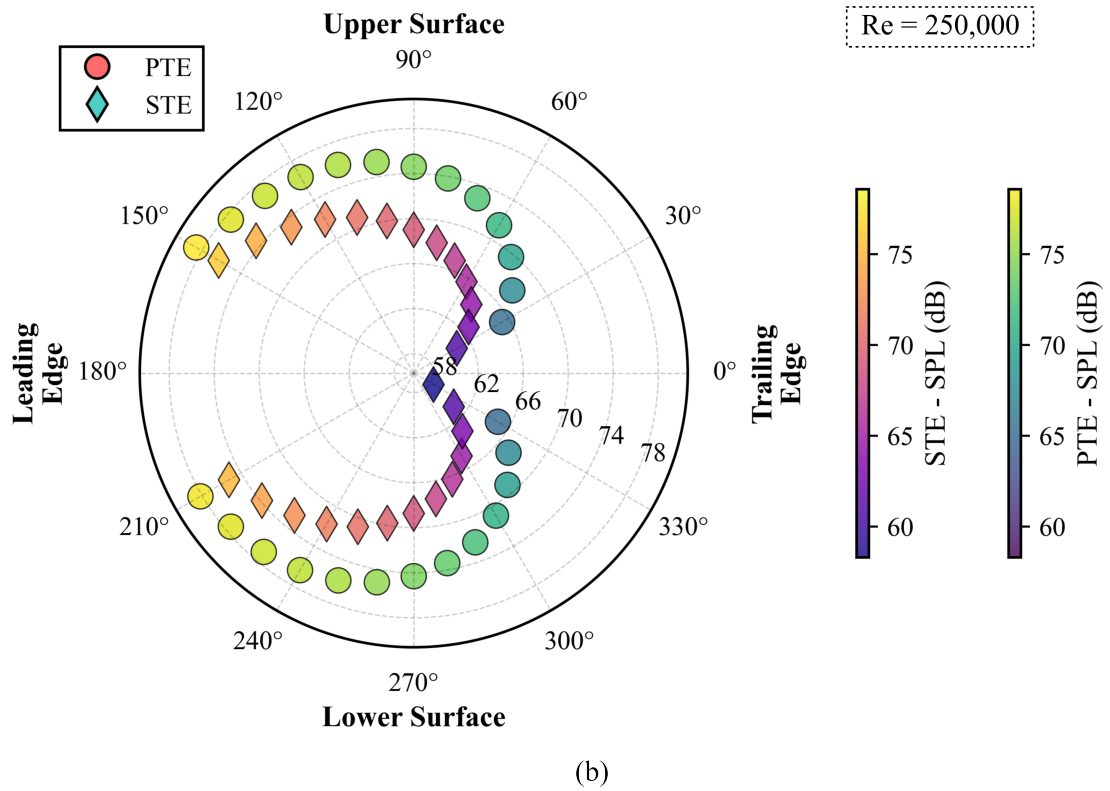
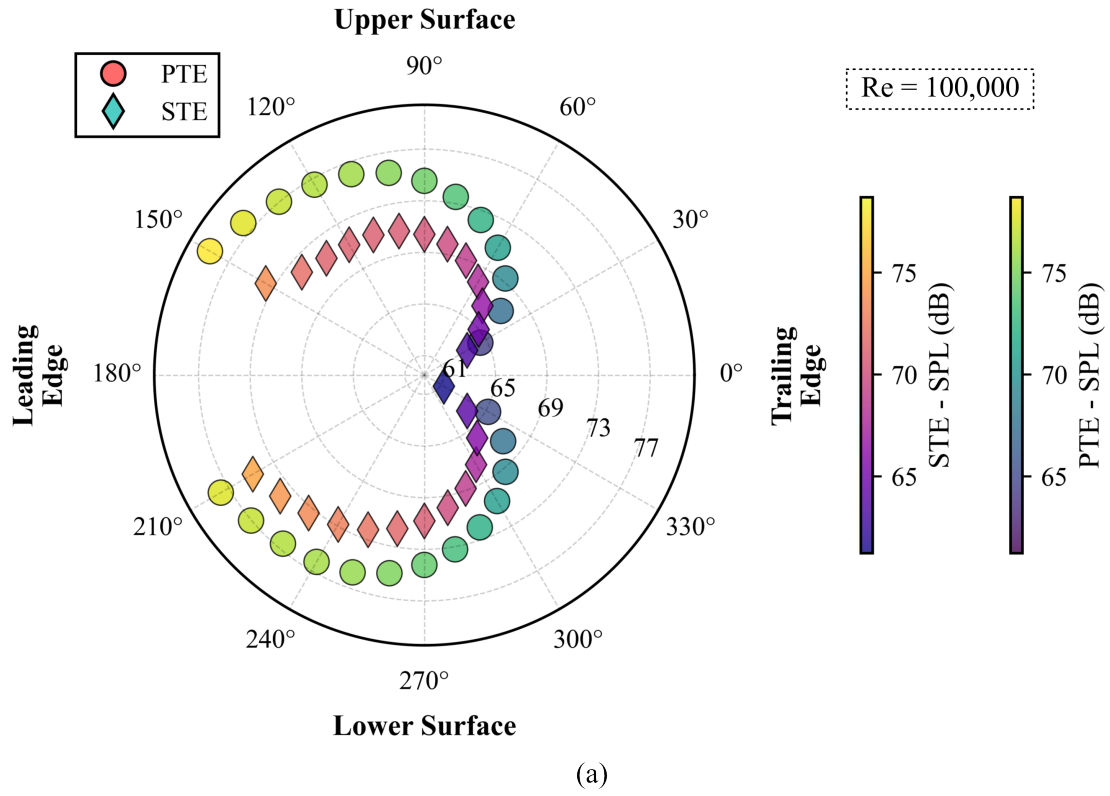


**Figure 3.25:** Polar plot visualization of PTE and STE sound pressure levels around the trailing edge for Reynolds numbers: (a) 100,000 and (b) 250,000. PTE data are shown with circles using the viridis colormap, while STE data use diamond markers with the plasma colormap.

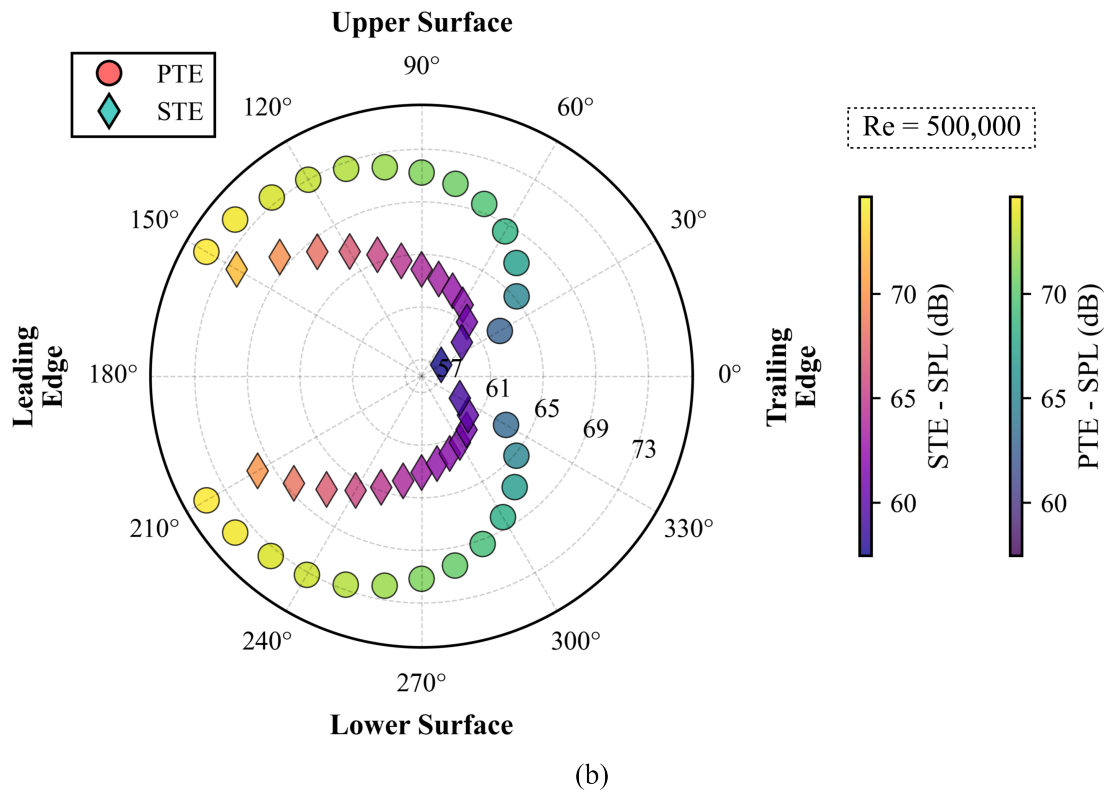
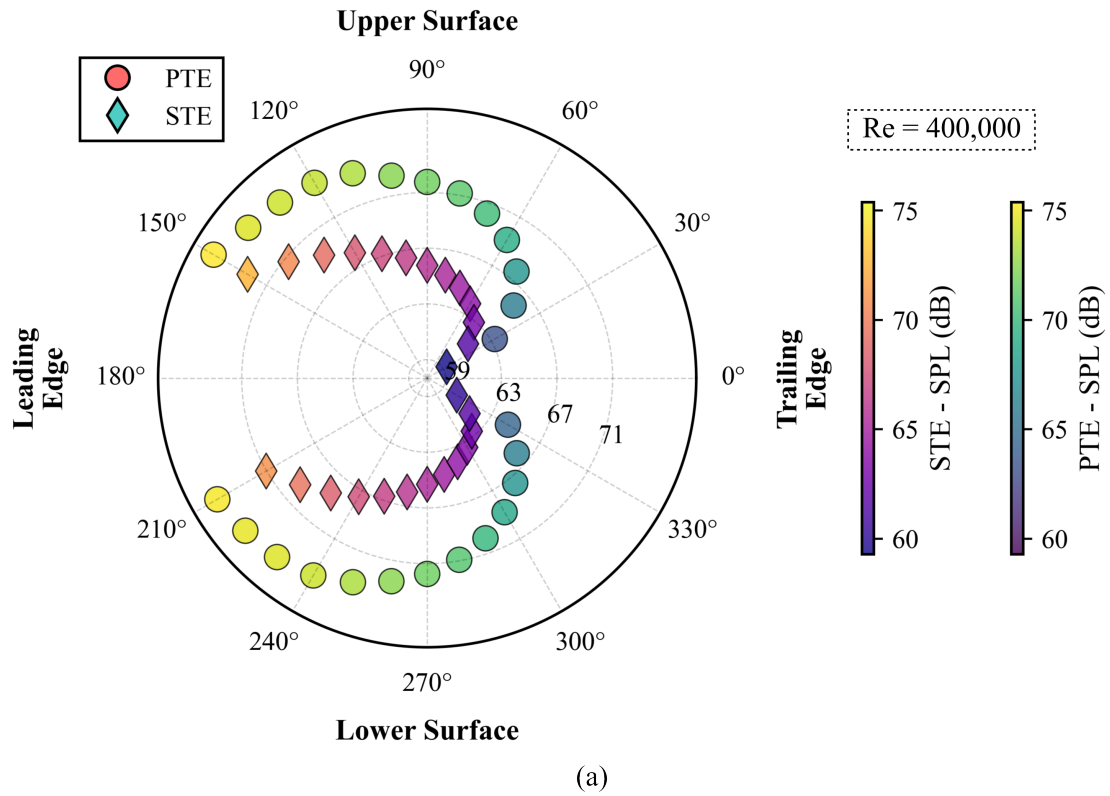


**Figure 3.26:** Polar plot visualization of PTE and STE sound pressure levels around the trailing edge for Reynolds numbers: (a) 400,000 and (b) 500,000. PTE data are shown with circles using the viridis colormap, while STE data use diamond markers with the plasma colormap.



values shift from the lower to the upper surface with increasing Reynolds number, although these differences are minimal.

**Table 3.3:** Statistical analysis of PTE and STE SPL data showing minimum, maximum, and mean values across different Reynolds numbers.

$Re \left[ \cdot 10^5 \right]$	PTE			STE		
	Min [dB]	Max [dB]	Mean [dB]	Min [dB]	Max [dB]	Mean [dB]
1	64.51	78.69	73.24	61.24	74.85	69.57
2.5	64.91	78.59	73.40	58.30	76.28	68.38
4	63.28	75.40	71.00	59.29	72.57	65.71
5	62.62	74.56	70.34	57.47	71.99	64.10

**Table 3.4:** Comprehensive comparison of SPL reduction between PTE and STE airfoils, with separate analysis for upper and lower surfaces across various Reynolds numbers. Values represent noise reduction achieved by the STE configuration.

$Re \left[ \cdot 10^5 \right]$	PTE/STE comparison			Lower surface comp.		Upp surface comp.	
	Min [dB]	Max [dB]	Mean [dB]	Max [dB]	Mean [dB]	Max [dB]	Mean [dB]
1	1.18	5.92	3.67	3.96	3.34	5.92	4.00
2.5	2.30	6.61	5.01	6.61	5.27	5.90	4.75
4	2.82	6.57	5.29	6.15	5.03	6.57	5.55
5	2.66	8.09	6.24	7.36	5.97	8.09	6.51

The choice of optimal serration design depends on the specific noise reduction objectives, and it is shown here that the Reynolds number can have a significant impact on fulfilling those objectives. If the goal is overall noise reduction, higher Reynolds number cases achieve better improvements in regions of interest where oscillations are pronounced due to transition regions in PTE airfoil cases. Conversely, if the purpose of serrations is to reduce maximum sound level regions, greater effectiveness is observed at lower Reynolds numbers. These conclusions apply specifically to the Reynolds number range from 100,000 to 500,000 examined in this study. This design trade-off reflects the fundamental challenge in aeroacoustic optimization, where different noise metrics may favor different configurations depending on the specific application requirements [48].

Overall, this consistency across the Reynolds number range, both aerodynamically and aeroacoustically, validates the effectiveness of serrated trailing edges as passive flow control devices for moderate Reynolds number applications, including small aircraft. The demonstrated

dual benefits of improved aerodynamic stability and significant noise reduction make serrated trailing edges particularly attractive for noise-sensitive applications where environmental impact is a primary concern [53].

## **4 PRIMARY AND SERRATED EDGE WINGS COMPARISON WITH LBM ANALYSIS**

This chapter integrates the methodological frameworks and findings from Chapters 2 and 3 to provide a comprehensive three-dimensional LBM analysis of bio-inspired airfoil configurations. The integration of experimental validation from Chapter 2 with the detailed flow physics understanding from Chapter 3 enables a robust computational framework for evaluating serrated trailing edge performance under realistic three-dimensional conditions. The established LBM approach and methodology from Chapter 2 are employed, along with enhanced UltraFluidX software capabilities, to analyze the bio-inspired wing configurations investigated in Chapter 3.

This chapter addresses a critical gap in the existing literature by providing direct three-dimensional LBM validation of serrated trailing edge designs, bridging the gap between two-dimensional idealized studies and realistic finite-wing applications. The chapter structure comprises three main sections: Section 4.1 presents comprehensive information about the geometric construction methodology for both primary trailing edge (PTE) and serrated trailing edge (STE) wings, including the implementation of sinusoidal serration variants. Section 4.2 details the numerical setup and specialized UltraFluidX wall modeling approaches required for accurate boundary layer representation. Finally, Section 4.3 presents detailed LBM results for both PTE and STE configurations with a comprehensive comparative analysis and performance assessment.

### **4.1 Three-dimensional wing geometry definition**

To configure three-dimensional wing geometries for detailed LBM analysis, a combination of Python scripting with FreeCAD and associated macro functionalities has been employed to generate all wing configurations. This computational approach offers superior geometric control and repeatability compared to manual CAD construction, enabling parametric studies and systematic design optimization. Unlike the approach utilized in Chapter 2, where Airfoil Tools [107] provided coordinate data for subsequent 2D extrusion in SolidWorks, the present

methodology employs mathematical equations for NACA 4-digit airfoils to ensure precise geometric representation.

The thickness distribution for NACA 4-digit airfoils is defined by Equation 4.1:

$$y_t = 5t [0.2969\sqrt{x} - 0.1260x - 0.3516x^2 + 0.2843x^3 - 0.1015x^4] \quad (4.1)$$

where  $x$  represents the normalized chordwise position ranging from zero to unity,  $y_t$  denotes the half-thickness at position  $x$ , and  $t$  represents the maximum thickness as a fraction of chord length. For the symmetric airfoils, such as NACA 0012, the camber line coincides with the chord line, simplifying the coordinate generation process. Consequently, the  $x$ -coordinates for upper and lower surfaces are identical ( $x = x_u = x_l$ ), while the  $y$ -coordinates are calculated as  $y_u = y_t$  and  $y_l = -y_t$ , respectively.

The discretization strategy for airfoil surface representation requires careful consideration of both geometric accuracy and computational efficiency. Insufficient point density can introduce geometric discontinuities that affect boundary layer development, while excessive discretization increases computational overhead without proportional accuracy gains. The number of discretization points directly impacts RAM requirements in UltraFluidX simulations, as the software's preprocessing tool must accurately differentiate between fluid and solid regions.

Based on these considerations, 200 points are specified to describe the airfoil surface, with enhanced point density concentrated near the leading edge where curvature gradients are most pronounced, as illustrated in Figure 4.1. This distribution strategy follows established practices in computational geometry, where higher resolution is applied in regions of maximum curvature to preserve geometric fidelity and ensure accurate flow field prediction [140].

As clearly visible in Figure 4.1, the geometric implementation features carefully designed point clustering strategies. The upper left magnified region demonstrates the concentrated point distribution around the leading edge, where the tight spacing ensures accurate representation of the high curvature region critical for stagnation point formation and pressure recovery. The lower right magnified region illustrates the trailing edge treatment, showing the finite-thickness implementation that distinguishes this configuration from the idealized sharp trailing edge employed in Chapter 3. This finite thickness representation more accurately reflects realistic manufacturing constraints and experimental conditions, though it introduces additional complexity in wake formation and boundary layer development compared to sharp trailing edge configurations [82].

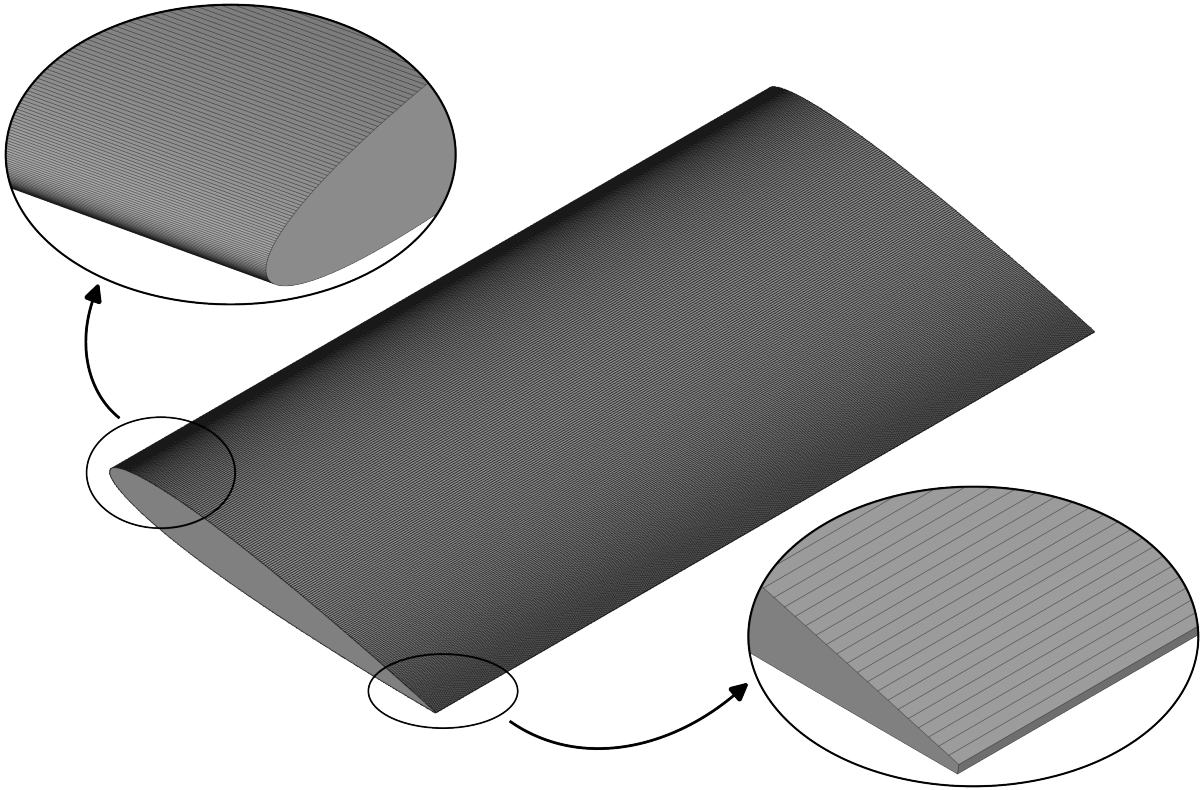


**Figure 4.1:** PTE wing surface discretization showing three-dimensional geometry with detailed mesh point distribution. The main figure displays the full wing planform, while the magnified insets highlight: (upper left) the leading edge region with enhanced point clustering for accurate curvature representation, and (lower right) the trailing edge region demonstrating the finite-thickness implementation with blunt trailing edge geometry.

Regarding the STE case, serrations are added to the consistent PTE wing. To maintain consistency with the analysis presented in Chapter 3, the serration wavelength is specified as  $0.05L_C$ , while the amplitude corresponds to  $0.1L_C$ . These geometric parameters are based on bio-inspired design principles derived from owl feather analysis, where similar wavelength-to-amplitude ratios have demonstrated optimal noise reduction characteristics [52]. To ensure adequate mesh resolution around the serrated geometry, each triangular serration element is discretized using 50 points.

A fundamental difference between the current three-dimensional approach and the Chapter 3 methodology involves the spanwise boundary conditions. The present configuration features a finite span of 0.3 m, corresponding to 200% of the chord length, representing realistic finite-wing conditions. In contrast, the Joukowski airfoil analysis in Chapter 3 employed a span of only 10% chord length with periodic boundary conditions to simulate infinite-span conditions. This dimensional scaling significantly affects the flow physics, as finite-span effects

introduce tip vortices, induced drag, and three-dimensional pressure redistributions that are absent in infinite-span configurations.

In addition to triangular serrations, sinusoidal serration profiles are investigated using identical wavelength and amplitude parameters. The distinct geometric characteristics of both variants are clearly demonstrated in Figure 4.2, which provides a detailed visualization of the trailing edge morphologies and their geometric implementation.

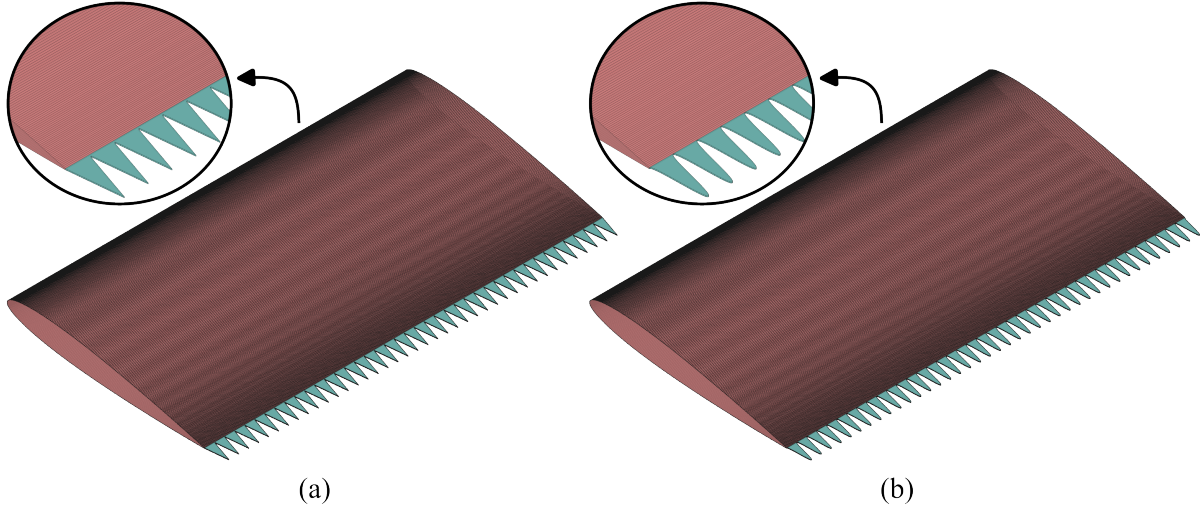


**Figure 4.2:** STE wing configurations: (a) triangular serrations with sharp vertices, and (b) sinusoidal serrations with smooth curvature transitions. Both maintain identical wavelength ( $0.05L_C$ ) and amplitude ( $0.1L_C$ ) parameters.

Based on these three geometric configurations (PTE, triangular STE, and sinusoidal STE) with primary focus on the PTE and triangular STE variants, a comprehensive analysis is conducted in the subsequent sections. The geometric foundation established through this parametric modeling approach ensures reproducible results and enables future design optimization studies.

## 4.2 Numerical setup and wall model changes

The numerical domain configuration follows the same approach as described in Chapter 2, Section 2.3. It comprises six nested refinement zones, with the finest zone encompassing the wing region at a mesh size of  $2.66 \cdot 10^{-6}$  m. Although the simulation setup remains consistent, this chapter employs UltraFluidX version 2025, whereas Chapter 2 utilized version 2021. The use of the latest UltraFluidX version incorporates several algorithmic improvements and enhanced wall modeling capabilities, which are critical for accurately capturing near-wall turbulence and complex flow structures around bio-inspired geometries [141].

The primary differences between simulation cases pertain to the wall modeling approaches. Both software versions implement Wall Modeled Large Eddy Simulation (WMLES) capabilities through various coupling strategies and theoretical wall laws. UltraFluidX employs an advanced geometric modeling technique for solid wall treatment, wherein the volume mesh is intersected with the surface mesh to delineate fluid and solid regions based on voxel center positions relative to the surface geometry. For each fluid node, the solver computes the effective distance to the nearest wall by measuring subgrid distances along each lattice connection to neighboring nodes, combining these measurements with appropriate weighting. This methodology facilitates accurate modeling of turbulent boundary layers using wall functions that integrate seamlessly with the Smagorinsky LES turbulence model, specifically adapted for the LBM [141].

In contrast, the differences between the two versions are as follows. Simulations in Chapter 2 utilized a Generalized Wall Function (GWF) with one-way coupling and a wall model intensity parameter set to 0.5, which controls the coupling strength between the velocity field and the wall model. The one-way coupling approach represents a simplified WMLES strategy where the wall model influences the flow field, but feedback from the near-wall flow to the wall model is limited. In this scheme, the slip velocity at the wall is derived directly from the LES bulk flow information without incorporating wall shear stress feedback mechanisms [142]. This approach, combined with averaging over the last 10% of the simulation duration, provides a robust foundation for comparison with experimental data. However, the one-way coupling approach may inadequately capture transient near-wall dynamics and complex vortical structures, particularly in unsteady flows around serrated trailing edges, necessitating more sophisticated modeling for detailed flow analysis.

Consequently, in this chapter, an adaptive two-way coupling approach employing a Generalized Law of the Wall (GLW) is adopted. The GLW was introduced in UltraFluidX version 2023 and has since become the default choice for enhanced near-wall accuracy [143]. Classical two-way coupling utilizes wall shear stress from the wall model as input for slip velocity computation. The adaptive two-way coupling differs by implementing dynamic adaptation mechanisms that automatically adjust the wall model behavior based on local flow conditions and boundary layer characteristics. This adaptive approach improves the fidelity of near-wall turbulence representation by enabling bidirectional interaction between the wall model and the resolved flow, thereby capturing transient phenomena and complex flow features more accurately [141].

Overall, the adaptive two-way coupling with GLW represents the most computationally sophisticated and physically accurate approach, while the GWF with one-way coupling offers robust performance with broader applicability across varying mesh resolutions and flow conditions.

## **4.3 Aerodynamic Performance Analysis of PTE and STE Wings**

This section presents a comprehensive aerodynamic performance analysis of both primary trailing edge (PTE) and serrated trailing edge (STE) wing configurations using the enhanced UltraFluidX 2025 framework with adaptive two-way coupling and Generalized Law of the Wall (GLW) modeling. The analysis employs finite-span wing conditions (0.3 m span) to capture realistic three-dimensional effects, including tip vortices and induced drag phenomena absent in two-dimensional studies. The investigation proceeds in two stages: first, the enhanced LBM methodology is validated against experimental wind tunnel data for the PTE configuration across multiple angles of attack ( $2^\circ$ ,  $4^\circ$ ,  $6^\circ$ , and  $8^\circ$ ), establishing confidence in the computational framework's ability to capture complex boundary layer phenomena and pressure distributions. Subsequently, a detailed comparative analysis between PTE and STE wings examines aerodynamic efficiency metrics, temporal stability characteristics, and underlying flow physics mechanisms. This dual approach ensures both methodological rigor through experimental validation and a comprehensive understanding of bio-inspired trailing edge modifications on wing performance under realistic operating conditions.

### **4.3.1 PTE Analysis and Validation**

Before conducting a detailed comparative analysis between the PTE and STE wings, the new PTE simulation must be validated against experimental data. As described in Section 4.2, the adaptive two-way coupling with GLW for near-wall region modeling enables more detailed flow observation. However, enhanced fluid flow resolution introduces increased oscillations, and results are expected to exhibit fluctuations around experimental values. Nevertheless, trends and overall magnitudes should remain within reasonable bounds of wind tunnel data. Figure 4.3 shows newly obtained UFX data of averaged  $C_p$  values over the last 10% of simulation duration, positioned within reasonable agreement with experimental data. For lower angle of attack values, the upper surface demonstrates better correlation with experimental and previous UFX



2021 data. Higher angle of attack wings correlate well with lower surface measurements but exhibit discontinuities around the upper surface. As the angle of attack increases, the minimum pressure coefficient values deviate from the experimental data. The enhanced wall modeling approach captures near-wall turbulence with greater fidelity, leading to increased solution sensitivity to boundary layer instabilities and transition phenomena.

Examining the discontinuities across all angles of attack cases reveals abrupt changes in upper surface curve trends. In Figure 4.3(d), the minimum peak near the leading edge is not captured, while around mid-chord, pressure coefficient values rise above experimental results. Moving streamwise toward the trailing edge, these deviations diminish, and data correlation improves. These abrupt mid-chord changes can be attributed to Laminar Separation Bubble (LSB) occurrence, discussed in detail in Chapter 3, Subsection 3.3.2. The same pattern appears at other angles, with the LSB occurrence shifting toward the trailing edge as the angle of attack decreases.

Regarding overall comparison with experimental data and higher deviations compared to UFX 2021 results based on one-way coupling with GWF, the current results exhibit higher oscillation levels. Beyond streamwise volatility, two-way coupling with GLW captures spanwise variations, as shown in Figure 4.4. Colored markers represent values from three different spanwise sections: root ( $z = 0$  m) at the mid-plane to wing tip at  $z = 0.125$ , where the span terminates at 0.15 m. All data points are redistributed using Python post-processing with 250 points for enhanced data visualization. The continued analysis section throughout this dissertation corresponds to  $z = 0$  m. Chapter 2 methodology did not capture significant spanwise variations, so only mid-plane analysis was presented. Chapter 3 provided a detailed fluid flow analysis but focused on streamwise orientation with minimal spanwise direction (10% chord length) and periodic boundary conditions that mimic infinite span.

This analysis reveals higher volatility on the mid-plane as the simulation comes to an end. On the other hand, a lower level of deviations is observed near the tip, with decreased pressure lift values. This is related to the wing tip vortex, and a more detailed explanation can be found a bit further down in the text, which is illustrated in Figure 4.9. Overall, three-dimensional effects become increasingly important in finite-wing configurations, where tip vortices induce spanwise pressure variations and modify the effective angle of attack distribution along the span. These effects are absent in two-dimensional or infinite-span simulations but are critical for realistic aerodynamic assessment [82].

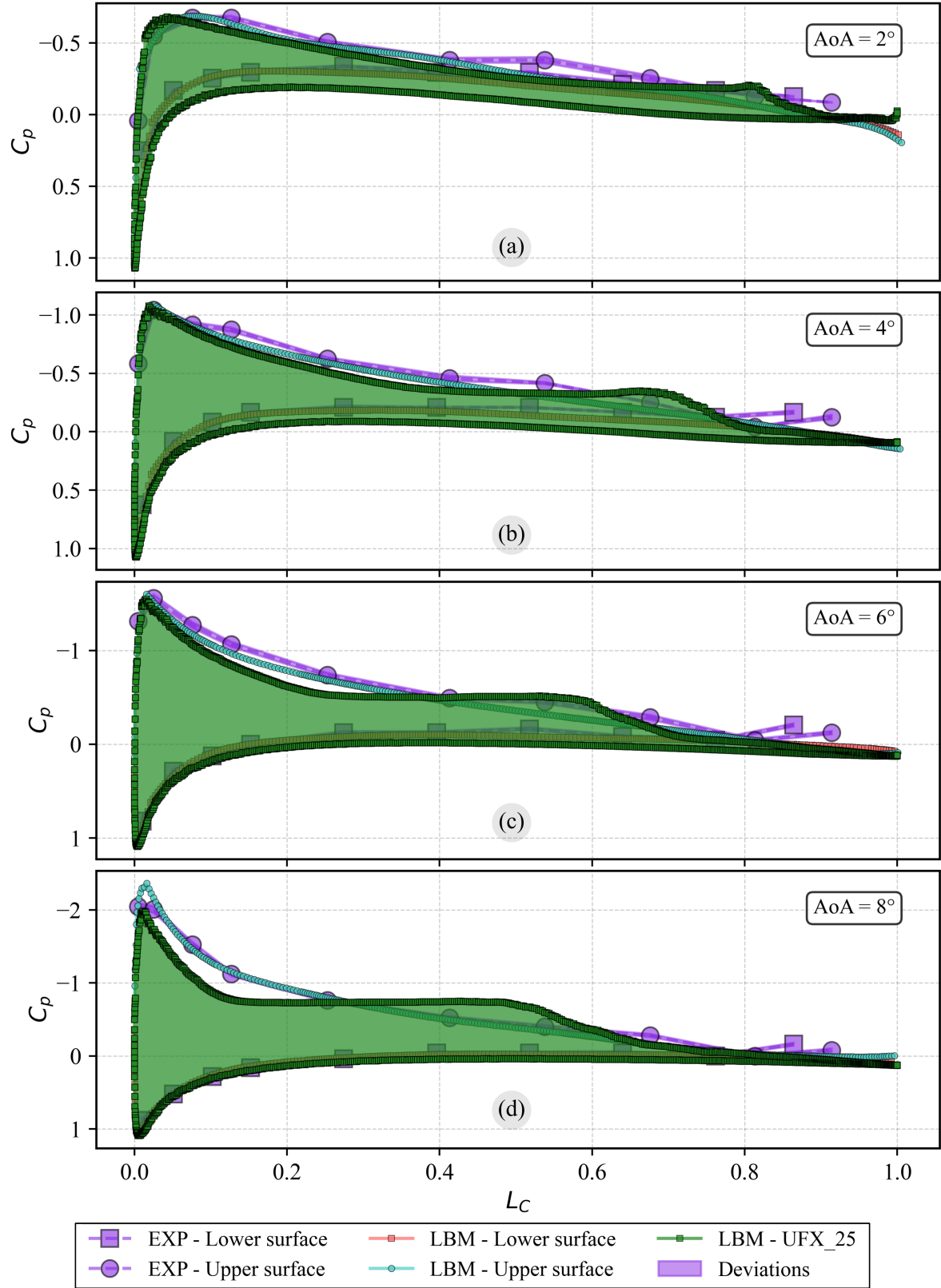


**Figure 4.3:** Pressure coefficient distributions comparing LBM-UFX 2025 results averaged over the last 10% (green rectangles with filled areas representing lift) with experimental data (violet markers and dashed lines with filled regions representing measurement uncertainties) and LBM-UFX 2021 data (red and teal markers).

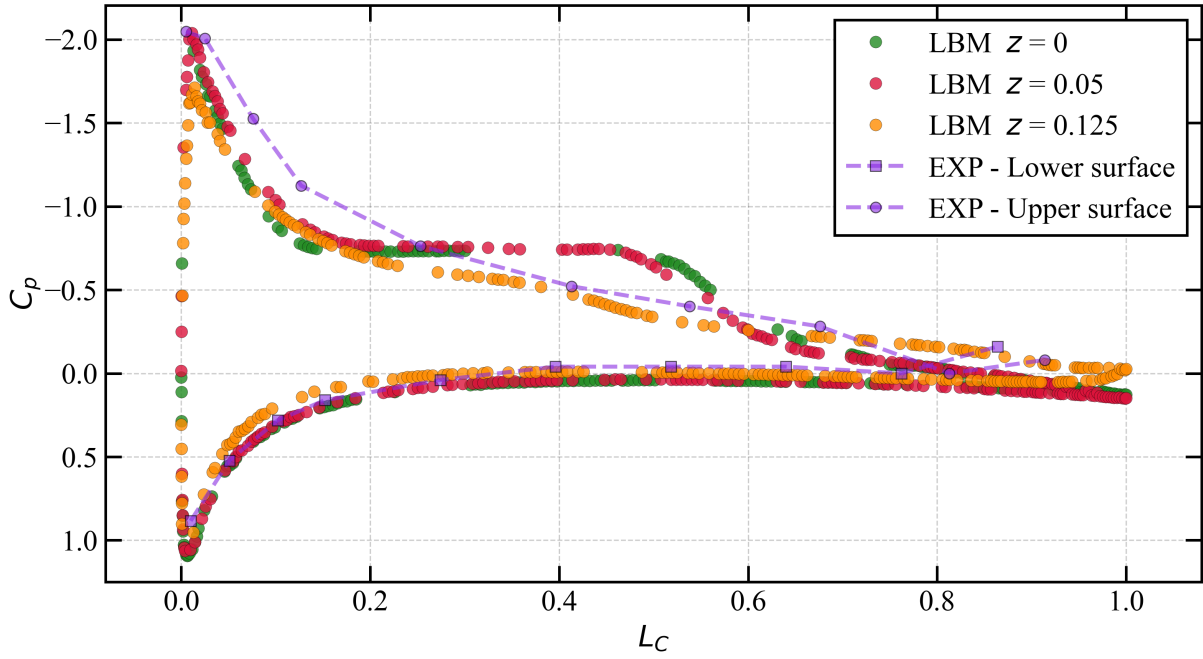


**Figure 4.4:** Pressure coefficient distributions for different spanwise sections compared with experimental data (violet markers). The previously analyzed section is shown in green at  $z = 0$  m, while sections at  $z = 0.05$  m and  $z = 0.125$  m are displayed in red and dark orange, respectively.

Beyond averaged results, Figure 4.5 presents similar data to Figure 4.3 but displays only final time-step pressure coefficient values instead of averaged data over the last 10%. Oscillations are preserved across all four angle of attack cases. Again, oscillations occur closer to the leading edge at higher angles of attack, while at decreased angles, these deviations move downstream toward the trailing edge.

### 4.3.2 Comparative Analysis: PTE vs. STE Wings

Following basic PTE analysis, a comprehensive comparison between PTE and STE configurations focuses primarily on the most complex case at an  $8^\circ$  angle of attack. To validate aerodynamic efficiency, lift and drag coefficients are obtained for both configurations and presented in Figures 4.6 and 4.7, respectively. Data are sampled at frequent intervals with time steps of  $2.826 \cdot 10^{-5}$  s, providing precise temporal resolution for both cases. Values are automatically calculated by UltraFluidX using standard lift and drag coefficient formulations:  $C_D = \frac{2F_D}{\rho v^2 A}$  and  $C_L = \frac{2F_L}{\rho v^2 A}$ , where  $\rho = 1.176$  kg/m<sup>3</sup>,  $v = 20$  m/s, and reference area  $A = c \cdot s = 0.045$  m<sup>2</sup>. Coefficients are computed at each time step, while averaged values over the last 10% of simulation duration are summarized in Table 4.1.

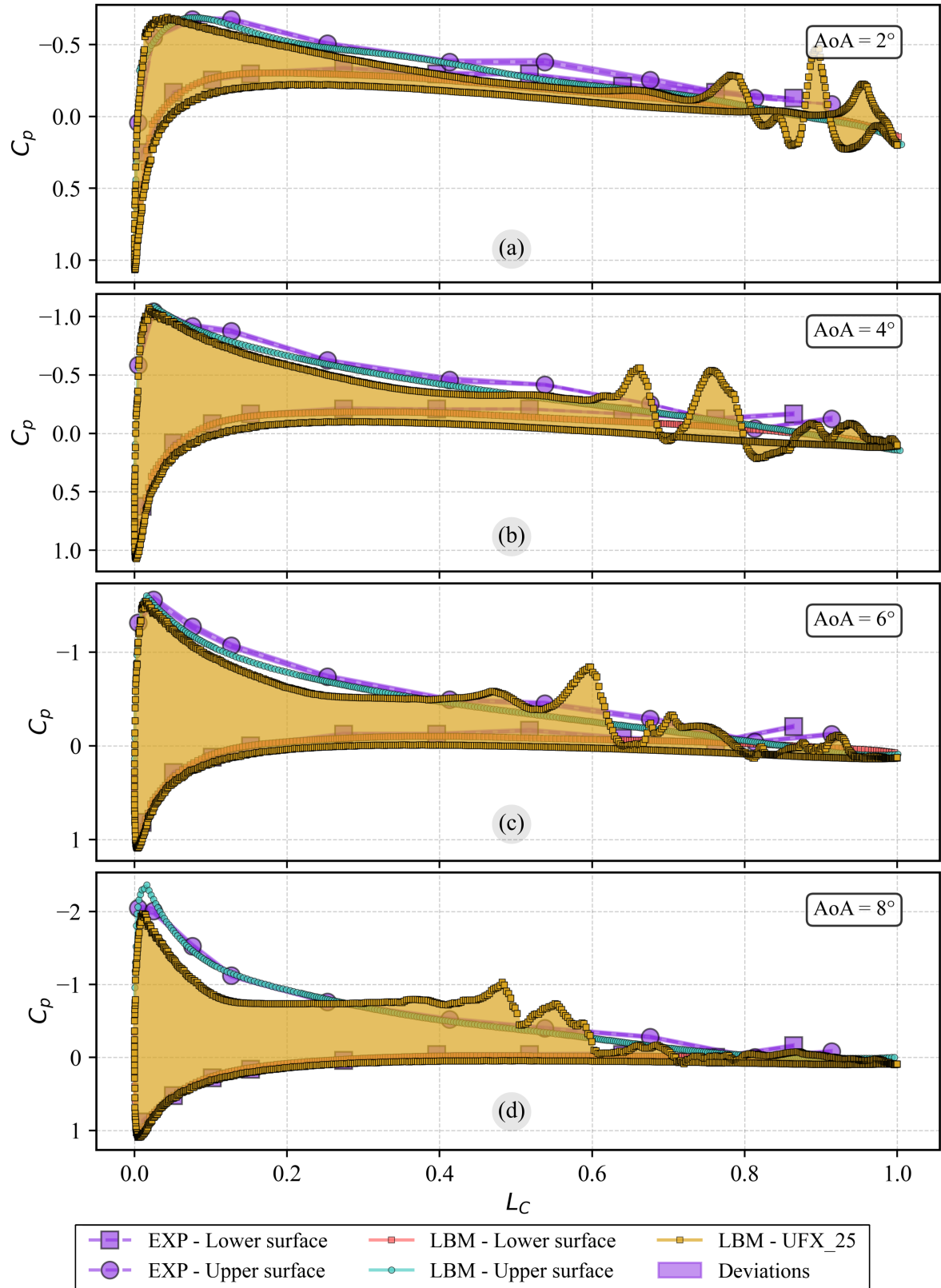


**Figure 4.5:** Pressure coefficient distributions comparing LBM-UFX 2025 results for the final time step (yellow rectangles with filled areas representing lift) with experimental data (violet markers and dashed lines with filled regions representing measurement uncertainties) and LBM-UFX 2021 data (red and teal markers).

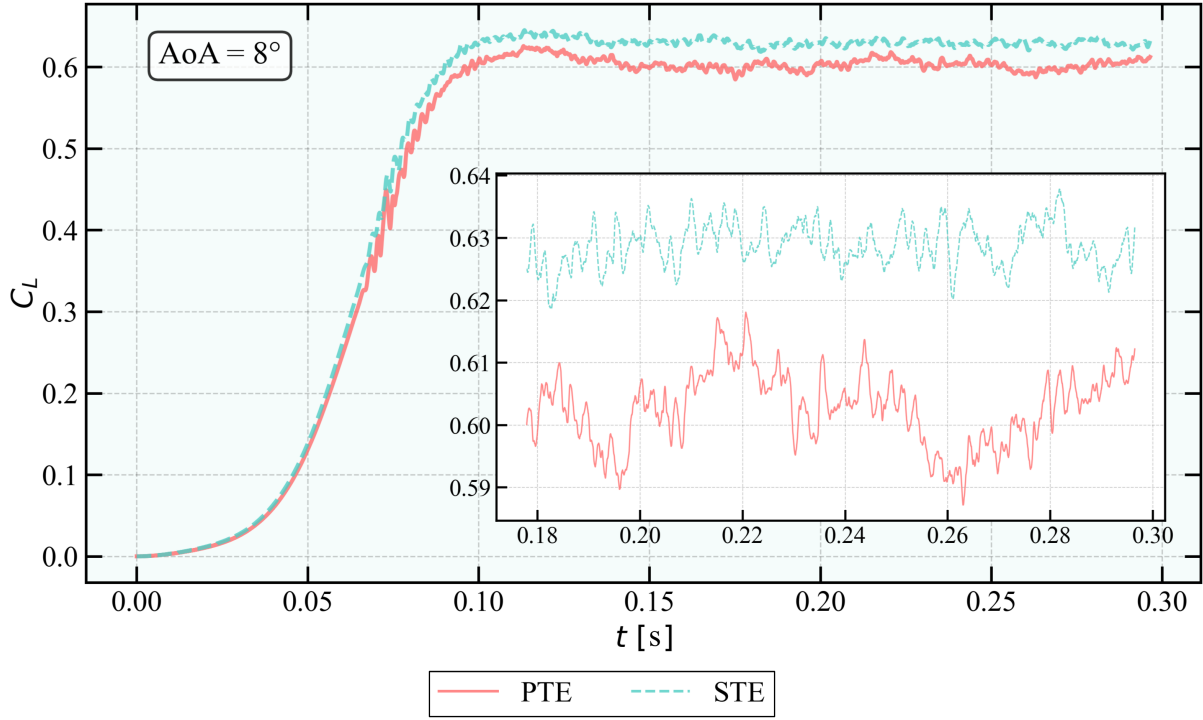


**Figure 4.6:** Temporal lift coefficient comparison for PTE (red line) and STE (teal dashed line) wings at  $8^\circ$  angle of attack with inset showing the final 40% of simulation duration emphasizing oscillations in the converged stage.

Lift results in Figure 4.6 demonstrate higher  $C_L$  values for the STE wing, consistent with analysis from Chapter 3 for similar wing configurations but different flow conditions ( $5^\circ$  angle of attack, Mach 0.25, and  $Re = 250,000$ ). Beyond 4.26% improved lift performance, the STE case provides less fluctuating lift coefficients, benefiting overall control and safety characteristics. Regarding drag coefficient, increased skin friction from serrations contributes to higher drag, with PTE demonstrating a 4.73% advantage. However, the STE wing again provides significantly less varying results compared to PTE, as is particularly evident in the converged simulation portion, highlighted in the inset graph.

Quantified lift and drag coefficient values are presented in Table 4.1. Notably, averaged results do not demonstrate lift coefficient advantages for the two lowest angles of attack cases, while  $6^\circ$  AoA has a small  $C_L$  gain, and a bit higher  $C_D$  drop. Conversely, drag improvements are observed for lower AoA. The AoA dependency of serration effectiveness reflects the changing balance between beneficial boundary layer modification and adverse pressure gradient strength. At lower angles, serrations may introduce premature transition without sufficient adverse gradient to benefit from enhanced mixing. Overall, it necessitates application-specific evaluation to determine the advantage of serration.

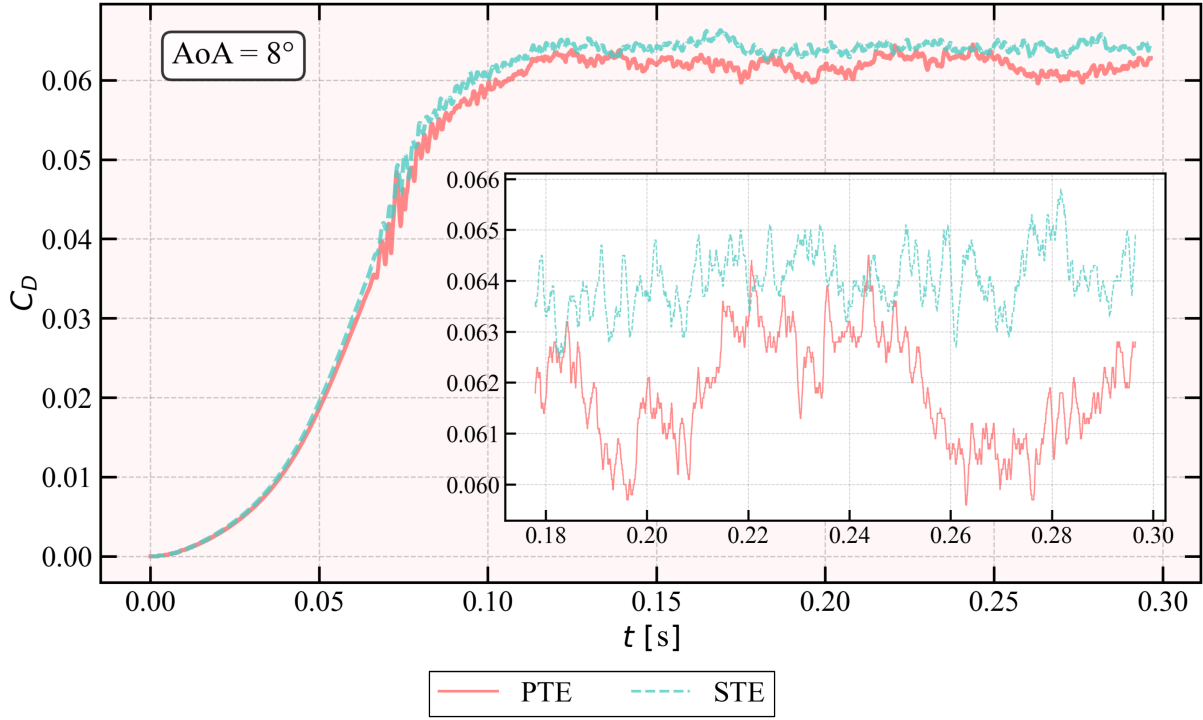


**Figure 4.7:** Temporal drag coefficient comparison for PTE (red line) and STE (teal dashed line) wings at  $8^\circ$  angle of attack with inset showing the final 40% of simulation duration emphasizing oscillations in the converged stage.

Beyond the converged portion, the acceleration phase presents interesting characteristics, highlighted for both  $C_L$  and  $C_D$  in Figure 4.8. Oscillations commence at similar times for both PTE and STE wings; however, deviation intensity remains stronger for the PTE case. During acceleration, both wings exhibit stronger oscillations only within the time range of approximately 0.07 to 0.09 s. This behavior originates from the development of vortex structures, starting with characteristic roll-up formation and progressing to three-dimensional vortical structures that contribute to the turbulent boundary layer transition. Boundary layer evolution and wake region development are visualized using  $Q$ -criterion in Figure 4.9.

By examining Figure 4.9(a), the bound vortex, mentioned in Chapter 3, Subsection 3.3.1, is clearly visualized for both PTE and STE wings. However, the bound vortex is momentarily segmented into multiple bound vortices for the STE wing due to triangular serrations at the trailing edge. The boundary layer remains laminar for both wings, while tip vortex development is observed at the wing tip. Wing tip vortices form due to the pressure differential between the upper and lower surfaces, creating a helical vortex structure that trails downstream from the wing tips. These vortices induce downwash and modify the effective angle of attack distribution, contributing to induced drag [131].

**Table 4.1:** Comparison of lift ( $C_L$ ) and drag coefficient ( $C_D$ ) for PTE and STE configurations across various angles of attack.

AoA	$C_L$		$C_D$	
	PTE	STE	PTE	STE
8°	0.6030	0.6287	0.0613	0.0642
6°	0.4618	0.4695	0.0408	0.0420
4°	0.3409	0.3306	0.0304	0.0298
2°	0.2035	0.1765	0.0237	0.0226

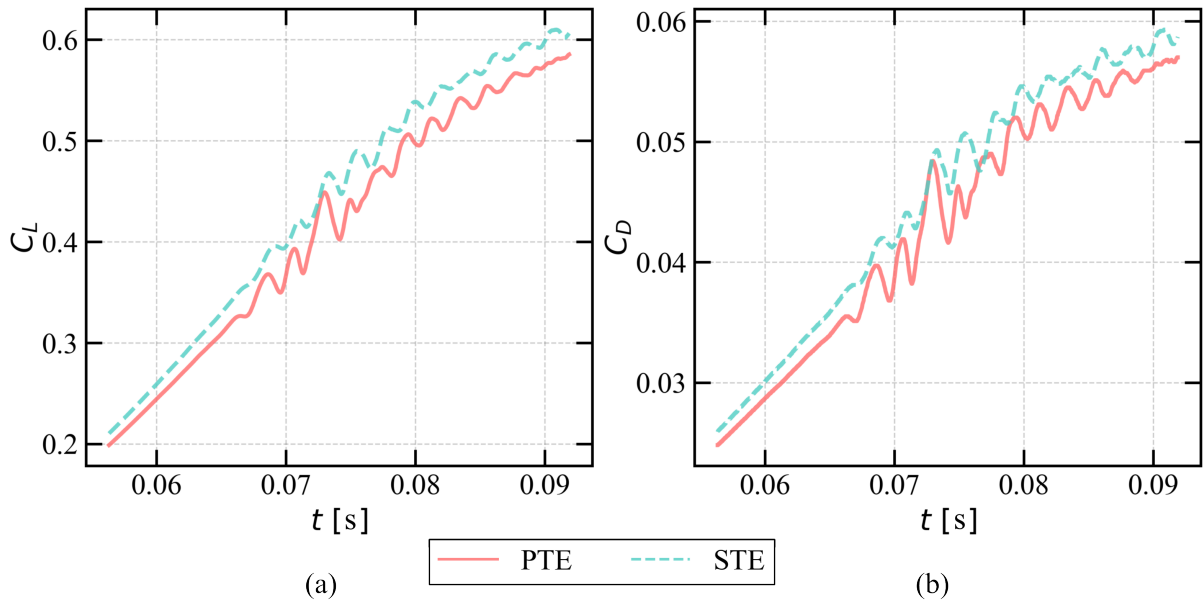


**Figure 4.8:** Lift and drag coefficient comparison between PTE (red line) and STE (teal dashed line) during the final portion of the acceleration phase.

In Figure 4.9(b), approximately 0.023 seconds later, several changes occur. The PTE wake exhibits characteristic roll-up structures, while the boundary layer maintains laminar characteristics despite transition region development near the trailing edge. The STE wing demonstrates similar boundary layer behavior, while regular streamwise structures propagate through the wake region. Wing tip vortices develop further and gain energy in both cases. Approximately 0.01 seconds later (Figure 4.9(c)), initial roll-ups manifest three-dimensional transformation near the wing tip, observable near the trailing edge for both PTE and STE configurations. Those tip region changes are caused by the wing tip vortex that continuously influences the wing without dissipating. Its effects are measurable through a reduction in lift or a decrease in pressure coefficient at the wing tip compared to the root, as shown in Figure 4.4 and consistent with studies by Smith et al. [144].



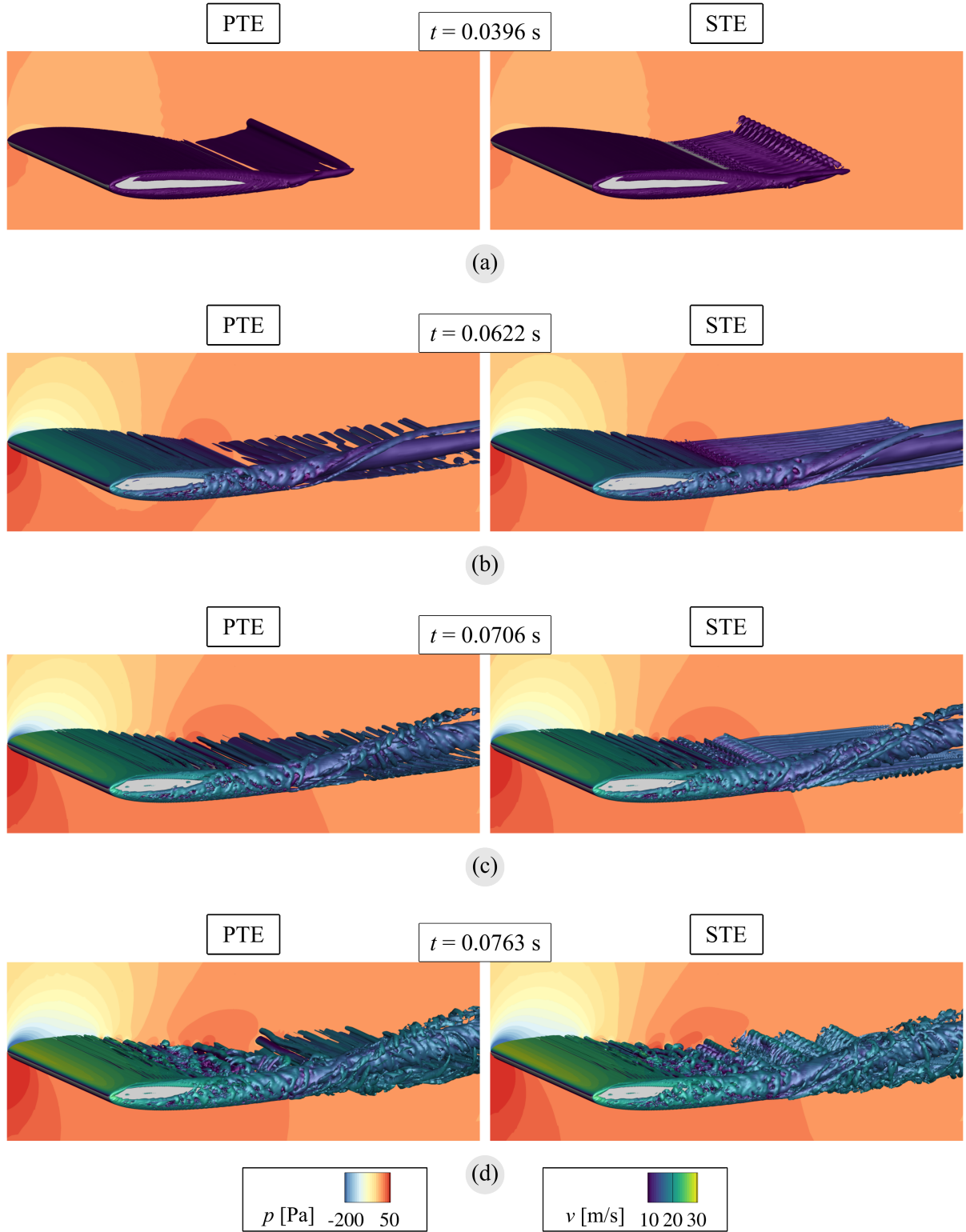


**Figure 4.9:** Representation of boundary layer transition, shear layer instability, wake region, and wing tip vortex development visualization using  $Q$ -criterion ( $Q = 1000$ ) colored by stream-wise velocity at different time steps: (a) 0.0396 s, (b) 0.0622 s, (c) 0.0706 s, and (d) 0.0763 s. Mid-plane cuts show pressure contours, with left subfigures representing PTE wings and right subfigures representing STE wings.



Wake region behavior differs between PTE and STE wings. Similar roll-up deviations occur near the trailing edge for PTE, while serrations fragment roll-ups that begin deviating in the vertical direction. Vortical oscillations continue in the STE wake, while PTE exhibits increased roll-up deviation from the ideal two-dimensional distribution. Along the boundary layer, increased wing chord transitions to turbulent conditions due to disturbances originating at the wing tip and propagating rapidly to the mid-plane.

Beyond  $Q$ -criterion iso-contours, vortical structures are visualized in two dimensions using vorticity contour plots shown in Figure 4.10. Similar patterns emerge as in Figure 4.9 between PTE and STE wings. Figure 4.10(a) reveals the bound vortex, followed by Kelvin-Helmholtz instability region development from the energetic shear layer to vortical structure formation in the wake (Figures 4.10(b), (c), and (d)). Kelvin-Helmholtz instabilities occur when the velocity shear across an interface becomes sufficiently large, resulting in unstable wave growth and vortex formation. These instabilities are fundamental to the development of shear layers and the enhancement of mixing [110].

Analysis thus far has focused on PTE and triangular STE comparison. However, a brief overview compares triangular and sinusoidal approaches for an  $8^\circ$  angle of attack. Overall, minimal, almost negligible differences exist between cases for these flow characteristics (Mach 0.057,  $Re = 191,000$ ). Lift coefficient relative error difference is 0.27% for the sinusoidal model, while the drag coefficient favors conventional triangular serrations by 0.78%. These small variations can be attributed to a slightly earlier boundary layer transition, as shown by the highlighted oscillations in Figure 4.11. The sinusoidal trailing edge provides marginally earlier boundary layer transition and more energetic flow, contributing to boundary layer modification. Nevertheless, for the specified flow characteristics, differences between models are negligible. However, for more confident and broader conclusions about the optimal serration type, various fluid flow setups should be analyzed to gather additional information.

Regarding computational expenses, all simulations were conducted on an Nvidia RTX A6000 GPU and an AMD Epyc 7662 64-Core Processor CPU. The most computationally intensive case ( $8^\circ$  angle of attack PTE wing) required a total runtime of 33h 5m 40s with peak CPU memory consumption of 57.228 GB (nearly double that of one-way GWF analysis with coarser geometry) and peak GPU memory of 14.034 GB (1.5 times higher than initial LBM cases). The STE case increased total runtime by approximately one hour to 33h 57m 52s with peak CPU memory of 59.652 GB and peak GPU memory of 14.764 GB. The least expensive case (PTE at

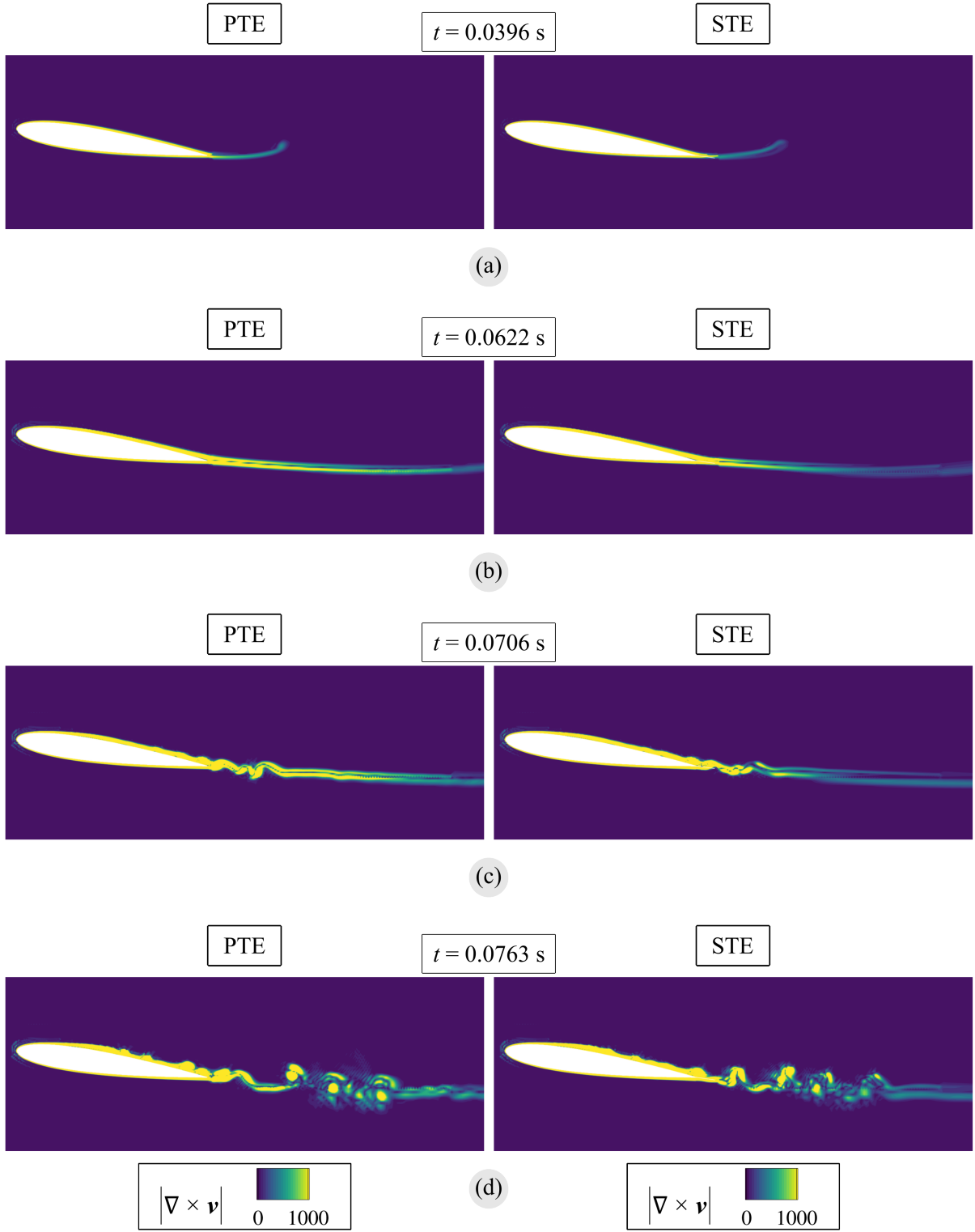


**Figure 4.10:** Physical phenomena representation using vorticity contour plots at different time steps: (a) 0.0396 s, (b) 0.0622 s, (c) 0.0706 s, and (d) 0.0763 s. Left subfigures represent PTE wings, while right subfigures represent STE wings.

a  $2^\circ$  angle of attack) required 24 hours, 10 minutes, and 29 seconds, with peak CPU and GPU memory of 56.305 GB and 13.508 GB, respectively.

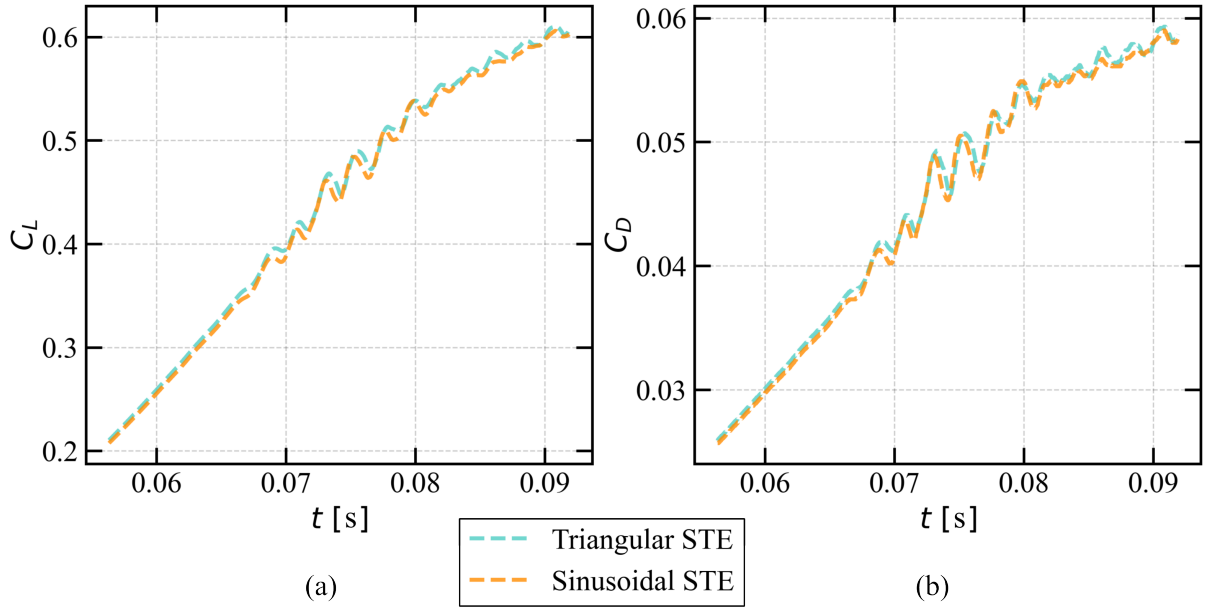


**Figure 4.11:** Comparison of triangular (teal dashed line) and sinusoidal (gold dashed line) STE wing models during acceleration phase for temporal: (a) lift coefficient and (b) drag coefficient analysis.

These computational requirements reflect the enhanced resolution and algorithmic sophistication of the adaptive two-way coupling approach, which provides superior physical fidelity at the cost of increased computational overhead.

## 5 CONCLUSION

This dissertation presents a comprehensive computational investigation of bio-inspired serrated trailing edge airfoils, employing a multi-scale approach that encompasses experimental validation, high-fidelity Large Eddy Simulation, and three-dimensional Lattice Boltzmann Method analysis. The research has systematically addressed the aerodynamic and aeroacoustic characteristics of these passive flow control devices across the moderate Reynolds number regime, providing fundamental insights into their performance mechanisms and practical applicability.

The mesoscopic Lattice Boltzmann Method has been demonstrated as a robust and accurate computational framework for the aerodynamic analysis of classical and bio-inspired airfoil configurations. The methodology adapted for this validation study is based on the LBM-LES model with a D3Q27 velocity set and the high-fidelity Cumulant-based collision operator. Likewise, a one-way coupling scheme with a Generalized Wall Function is implemented, providing a novel methodological approach. The validation study presented in Chapter 2 established excellent agreement between LBM predictions and experimental data conducted in an open-circuit wind tunnel for the NACA 0012 airfoil at a medium Reynolds number of 191,000 and a Mach number of 0.057. Computational force coefficients exhibited deviations of less than 3% compared with the measurement data across four evaluated angles of attack from  $2^\circ$  to  $8^\circ$ .

On the other hand, a robust macroscopic Large Eddy Simulation approach with a structured mesh provided a detailed analysis of the primary and serrated trailing edge Joukowski airfoil for a Reynolds number range of 100,000 to 500,000. Main investigations were carried out for 250,000  $Re$  to determine the importance of sound wave propagation and its influence on stream-wise fluid flow. As expected, TE noise is the predominant one; however, even at a low Mach number of 0.25 and a  $5^\circ$  angle of attack, TE sound waves still affect BL stability, shear layer stability, and the laminar separation bubble. Unsteady simulations are provided with the initial Gaussian acceleration, akin to the aircraft's takeoff. After providing numerical results in terms of grid resolution and wall distance analysis, several fluid flow phenomena were extrapolated.

A non-dimensional force in the  $x$ -direction has a strong high-pressure region during the acceleration phase due to the bound vortex that accelerates the flow. The suction effect becomes

dominant after the starting vortex dissipates, leading to the pressure force component becoming the primary force against the skin friction force. In terms of aerodynamic efficiency, drag is initially compromised at the beginning of the post-acceleration phase but becomes negligible over time. Lift, on the other hand, shows minimal differences initially but becomes stronger for the STE airfoil as time progresses.

Boundary layer instability analysis shows improvements with the introduction of the STE. One reason is the earlier and faster transition from the laminar to the turbulent boundary layer in the STE airfoil compared to the prolonged transition period in the CTE airfoil. Additionally, LSB forms and breaks in the boundary layer of the CTE airfoil, causing significant instability. The introduction of serrations triggers the formation of TBLs earlier and prevents the formation of LSBs. In both cases, TE sound waves influence the boundary layer, with the CTE airfoil experiencing an LSB break due to these waves. Beyond improving boundary layer stability, serrations also reduce the amplitude of sound waves. Overall, STE demonstrates consistent noise reductions of 3-8 dB across the Reynolds number range of 100,000 to 500,000, with minimal aerodynamic penalties. The lift-to-drag ratio degradation remained below 5% in most configurations, validating the effectiveness of passive noise reduction strategies for moderate Reynolds number applications.

Finally, an improved two-way coupling with the Generalized Law of the Wall has been employed for LBM-LES analysis of STE, incorporating the sinusoidal STE approach. The extension to three-dimensional finite wing span analysis has revealed the importance of spanwise variations in serration effectiveness, particularly in the effect of wing tip vortices on boundary layer transition.

This dissertation has successfully addressed and demonstrated the effectiveness of serrated trailing edges as passive flow control devices for moderate Reynolds number applications. The comprehensive computational analysis has provided fundamental insights into the physical mechanisms governing serration performance while establishing robust methodological frameworks for future research.



# BIBLIOGRAPHY

- [1] W. E. Nagel, D. H. Kröner, and M. M. Resch, “High performance computing in science and engineering ’21: Transactions of the high performance computing center, stuttgart (hlrs) 2021,” *High Performance Computing in Science and Engineering ’21: Transactions of the High Performance Computing Center, Stuttgart (HLRS) 2021*, pp. 1–529, 1 2023.
- [2] T. Kruger, H. Kusumaatmaja, A. Kuzmin, O. Shardt, G. Silva, and E. M. Viggien, *The Lattice Boltzmann Method : Principles and Practice*. Springer International Publishing, 2017.
- [3] F. Kuznik, C. Obrecht, G. Rusaouen, and J. J. Roux, “LBM based flow simulation using GPU computing processor,” *Computers & Mathematics with Applications*, vol. 59, pp. 2380–2392, apr 2010.
- [4] C. K. Aidun and J. R. Clausen, “Lattice-boltzmann method for complex flows,” *Annual Review of Fluid Mechanics*, vol. 42, pp. 439–472, jan 2010.
- [5] J. H. Ferziger and M. Perić, *Computational Methods for Fluid Dynamics*. Springer Berlin Heidelberg, 3 ed., 2002.
- [6] O. C. Zienkiewicz, R. L. Taylor, and J. Z. Zhu, *The finite element method: its basis and fundamentals*. Amsterdam ; Boston : Elsevier Butterworth-Heinemann, 2005., 2005.
- [7] L. Wang, Z. Liu, and M. Rajamuni, “Recent progress of lattice boltzmann method and its applications in fluid-structure interaction,” *Proceedings of the Institution of Mechanical Engineers, Part C: Journal of Mechanical Engineering Science*, vol. 237, pp. 2461–2484, 6 2023.
- [8] R. Benzi, S. Succi, and M. Vergassola, “The lattice Boltzmann equation: theory and applications,” *Physics Reports*, vol. 222, no. 3, pp. 145–197, 1992.

- [9] S. Succi, *The lattice Boltzmann equation for fluid dynamics and beyond*. Clarendon Press, 2001.
- [10] G. R. McNamara and G. Zanetti, “Use of the boltzmann equation to simulate lattice-gas automata,” *Physical Review Letters*, vol. 61, no. 20, pp. 2332–2335, 1988.
- [11] F. J. Higuera and J. Jiménez, “Boltzmann approach to lattice gas simulations,” *EPL*, vol. 9, pp. 663–668, aug 1989.
- [12] T. Imamura, K. Suzuki, T. Nakamura, and M. Yoshida, “Flow simulation around an air-foil by lattice Boltzmann method on generalized coordinates,” *AIAA Journal*, vol. 43, no. 9, pp. 1968–1973, 2005.
- [13] Y. Peng, C. Shu, Y. T. Chew, X. D. Niu, and X. Y. Lu, “Application of multi-block approach in the immersed boundary-lattice Boltzmann method for viscous fluid flows,” *Journal of Computational Physics*, vol. 218, pp. 460–478, nov 2006.
- [14] J. Wu and C. Shu, “Implicit velocity correction-based immersed boundary-lattice Boltzmann method and its applications,” *Journal of Computational Physics*, vol. 228, pp. 1963–1979, apr 2009.
- [15] Y. L. Qiu, C. Shu, J. Wu, Y. Sun, L. M. Yang, and T. Q. Guo, “A boundary condition-enforced immersed boundary method for compressible viscous flows,” *Computers and Fluids*, vol. 136, pp. 104–113, sep 2016.
- [16] Z. Wang, Y. Wei, and Y. Qian, “A bounce back-immersed boundary-lattice Boltzmann model for curved boundary,” *Applied Mathematical Modelling*, vol. 81, pp. 428–440, may 2020.
- [17] H. B. Luan, H. Xu, L. Chen, D. L. Sun, Y. L. He, and W. Q. Tao, “Evaluation of the coupling scheme of FVM and LBM for fluid flows around complex geometries,” *International Journal of Heat and Mass Transfer*, vol. 54, pp. 1975–1985, apr 2011.
- [18] N. Pellerin, S. Leclaire, and M. Reggio, “Solving incompressible fluid flows on unstructured meshes with the lattice boltzmann flux solver,” *Engineering Applications of Computational Fluid Mechanics*, vol. 11, no. 1, pp. 310–327, 2017.



- [19] Z. Fang, C. Gong, A. Revell, G. Chen, A. Harwood, and J. O'Connor, "Passive separation control of a NACA0012 airfoil via a flexible flap," *Physics of Fluids*, vol. 31, oct 2019.
- [20] S. Chen and G. D. Doolen, "Lattice boltzmann method for fluid flows," *Annual Review of Fluid Mechanics*, vol. 30, pp. 329–364, 1998.
- [21] K. Li, C. Zhong, C. Zhuo, and J. Cao, "Non-body-fitted Cartesian-mesh simulation of highly turbulent flows using multi-relaxation-time lattice Boltzmann method," *Computers and Mathematics with Applications*, vol. 63, pp. 1481–1496, may 2012.
- [22] M. Geier, M. Schönherr, A. Pasquali, and M. Krafczyk, "The cumulant lattice Boltzmann equation in three dimensions: Theory and validation," *Computers & Mathematics with Applications*, vol. 70, pp. 507–547, aug 2015.
- [23] M. Geier, A. Pasquali, and M. Schönherr, "Parametrization of the cumulant lattice Boltzmann method for fourth order accurate diffusion part I: Derivation and validation," *Journal of Computational Physics*, vol. 348, pp. 862–888, nov 2017.
- [24] N. Pellerin, S. Leclaire, and M. Reggio, "An implementation of the Spalart–Allmaras turbulence model in a multi-domain lattice Boltzmann method for solving turbulent airfoil flows," *Computers and Mathematics with Applications*, vol. 70, pp. 3001–3018, dec 2015.
- [25] G. Di Ilio, D. Chiappini, S. Ubertini, G. Bella, and S. Succi, "Fluid flow around NACA 0012 airfoil at low-Reynolds numbers with hybrid lattice Boltzmann method," *Computers and Fluids*, vol. 166, pp. 200–208, apr 2018.
- [26] O. Malaspinas and P. Sagaut, "Consistent subgrid scale modelling for lattice Boltzmann methods," *Journal of Fluid Mechanics*, vol. 700, pp. 514–542, jun 2012.
- [27] J. Yao, C. Zhong, and K. Tang, "An adaptive-gridding lattice Boltzmann method with linked-list data structure for two-dimensional viscous flows," *Progress in Computational Fluid Dynamics*, vol. 17, no. 5, pp. 267–280, 2017.
- [28] J. A. Reyes Barraza and R. Deiterding, "Towards a generalised lattice Boltzmann method for aerodynamic simulations," *Journal of Computational Science*, vol. 45, sep 2020.

- [29] C. Zhuo, C. Zhong, K. Li, S. Xiong, X. Chen, and J. Cao, “Application of lattice Boltzmann method to simulation of compressible turbulent flow,” *Communications in Computational Physics*, vol. 8, no. 5, pp. 1208–1223, 2010.
- [30] K. Hejranfar and M. H. Saadat, “Preconditioned WENO finite-difference lattice Boltzmann method for simulation of incompressible turbulent flows,” *Computers and Mathematics with Applications*, vol. 76, pp. 1427–1446, sep 2018.
- [31] E. Leveque, H. Touil, S. Malik, D. Ricot, and A. Sengissen, “Wall-modeled large-eddy simulation of the flow past a rod-airfoil tandem by the Lattice Boltzmann method,” *International Journal of Numerical Methods for Heat and Fluid Flow*, vol. 28, pp. 1096–1116, may 2018.
- [32] J. Degryny, S. G. Cai, J. F. Boussuge, and P. Sagaut, “Improved wall model treatment for aerodynamic flows in LBM,” *Computers and Fluids*, vol. 227, sep 2021.
- [33] S. Wilhelm, J. Jacob, and P. Sagaut, “An explicit power-law-based wall model for lattice Boltzmann method-Reynolds-averaged numerical simulations of the flow around airfoils,” *Physics of Fluids*, vol. 30, jun 2018.
- [34] A. T. White and C. K. Chong, “Rotational invariance in the three-dimensional lattice Boltzmann method is dependent on the choice of lattice,” *Journal of Computational Physics*, vol. 230, no. 16, pp. 6367–6378, 2011.
- [35] S. K. Kang and Y. A. Hassan, “The effect of lattice models within the lattice Boltzmann method in the simulation of wall-bounded turbulent flows,” *Journal of Computational Physics*, vol. 232, pp. 100–117, jan 2013.
- [36] K. Suga, Y. Kuwata, K. Takashima, and R. Chikasue, “A D3Q27 multiple-relaxation-time lattice Boltzmann method for turbulent flows,” *Computers and Mathematics with Applications*, vol. 69, pp. 518–529, mar 2015.
- [37] A. Qiu, W. Sang, F. Zhou, and D. Li, “A subgrid model with multiple relaxation time for lattice boltzmann method based on the cartesian grid,” *Engineering Computations (Swansea, Wales)*, vol. 40, pp. 2303–2327, 12 2023.
- [38] Q. Jia, J. Zhang, W. zhi Liang, P. qing Liu, and Q. lin Qu, “A mathematical-boundary-recognition domain-decomposition lattice boltzmann method combined with large eddy

- simulation applied to airfoil aeroacoustics simulation,” *International Journal for Numerical Methods in Fluids*, vol. 96, pp. 1250–1275, 7 2024.
- [39] G. G. Spinelli, T. Horstmann, K. Masilamani, M. M. Soni, H. Klimach, A. Stück, and S. Roller, “Hpc performance study of different collision models using the lattice boltzmann solver musubi,” *Computers and Fluids*, vol. 255, 4 2023.
- [40] J. L. Krenchiglova, L. O. E. dos Santos, D. N. Siebert, and P. C. Philippi, “Lattice-Boltzmann simulation of incompressible fluid flow past immersed bodies: models and boundary conditions,” *International Journal of Numerical Methods for Heat and Fluid Flow*, 2022.
- [41] P. J. Bruce and S. P. Colliss, “Review of research into shock control bumps,” *Shock Waves*, vol. 25, pp. 451–471, 9 2015.
- [42] E. Jinks, P. Bruce, and M. Santer, “Optimisation of adaptive shock control bumps with structural constraints,” *Aerospace Science and Technology*, vol. 77, pp. 332–343, 6 2018.
- [43] M. S. Howe, “Aerodynamic noise of a serrated trailing edge,” *Journal of Fluids and Structures*, vol. 5, pp. 33–45, 1991.
- [44] R. K. Amiet, “Noise due to turbulent flow past a trailing edge,” *Journal of Sound and Vibration*, vol. 47, pp. 387–393, 8 1976.
- [45] X. Huang, “A theoretical study of serrated leading edges in aerofoil and vortical gust interaction noise,” *Advances in Aerodynamics*, vol. 1, pp. 1–13, 12 2019.
- [46] B. Lyu, M. Azarpeyvand, and S. Sinayoko, “Prediction of noise from serrated trailing edges,” *Journal of Fluid Mechanics*, vol. 793, pp. 556–588, 4 2016.
- [47] M. B. Gelot and J. W. Kim, “Broadband noise prediction for aerofoils with a serrated trailing edge based on amiet’s theory,” *Journal of Sound and Vibration*, vol. 512, p. 116352, 11 2021.
- [48] D. Casalino, F. Diozzi, R. Sannino, and A. Paonessa, “Aircraft noise reduction technologies: A bibliographic review,” *Aerospace Science and Technology*, vol. 12, pp. 1–17, 1 2008.
- [49] S. Moreau, “The third golden age of aeroacoustics,” *Physics of Fluids*, vol. 34, 3 2022.

- [50] K. Zhao, P. Okolo, E. Neri, P. Chen, J. Kennedy, and G. J. Bennett, “Noise reduction technologies for aircraft landing gear-a bibliographic review,” *Progress in Aerospace Sciences*, vol. 112, p. 100589, 1 2020.
- [51] N. Gao, Z. Zhang, J. Deng, X. Guo, B. Cheng, H. Hou, N. Gao, Z. Zhang, J. Deng, X. Guo, B. Cheng, and H. Hou, “Acoustic metamaterials for noise reduction: A review,” *Advanced Materials Technologies*, vol. 7, p. 2100698, 6 2022.
- [52] H. Weger, M. Weger, M. Klaas, and W. Schröder, “Features of owl wings that promote silent flight,” *Interface Focus*, vol. 7, 2 2017.
- [53] S. Oerlemans, M. Fisher, T. Maeder, and K. Kögler, “Reduction of wind turbine noise using optimized airfoils and trailing-edge serrations,” *AIAA Journal*, vol. 47, pp. 1470–1481, 6 2009.
- [54] F. Avallone, W. C. van der Velden, and D. Ragni, “Benefits of curved serrations on broadband trailing-edge noise reduction,” *Journal of Sound and Vibration*, vol. 400, pp. 167–177, 7 2017.
- [55] F. Avallone, W. C. V. D. Velden, D. Ragni, and D. Casalino, “Noise reduction mechanisms of sawtooth and combed-sawtooth trailing-edge serrations,” *Journal of Fluid Mechanics*, vol. 848, pp. 560–591, 8 2018.
- [56] L. E. Jones and R. D. Sandberg, “Acoustic and hydrodynamic analysis of the flow around an aerofoil with trailing-edge serrations,” *Journal of Fluid Mechanics*, vol. 706, pp. 295–322, 9 2012.
- [57] T. P. Chong and A. Vathylakis, “On the aeroacoustic and flow structures developed on a flat plate with a serrated sawtooth trailing edge,” *Journal of Sound and Vibration*, vol. 354, pp. 65–90, 10 2015.
- [58] T. P. Chong and P. F. Joseph, “An experimental study of airfoil instability tonal noise with trailing edge serrations,” *Journal of Sound and Vibration*, vol. 332, pp. 6335–6358, 11 2013.
- [59] F. Avallone, S. Pröbsting, and D. Ragni, “Three-dimensional flow field over a trailing-edge serration and implications on broadband noise,” *Physics of Fluids*, vol. 28, 11 2016.

- [60] P. Zhou, Q. Liu, S. Zhong, Y. Fang, and X. Zhang, “A study of the effect of serration shape and flexibility on trailing edge noise,” *Physics of Fluids*, vol. 32, 12 2020.
- [61] M. Zhao, H. Cao, M. Zhang, C. Liao, and T. Zhou, “Optimal design of aeroacoustic airfoils with owl-inspired trailing-edge serrations,” *Bioinspiration and Biomimetics*, vol. 16, 9 2021.
- [62] A. Celik, Y. D. Mayer, and M. Azarpeyvand, “On the aeroacoustic characterization of a robust trailing-edge serration,” *Physics of Fluids*, vol. 33, 7 2021.
- [63] S. M. Hasheminasab, S. M. Karimian, S. Noori, M. Saeedi, and C. Morton, “Experimental investigation of the wake dynamics for a naca0012 airfoil with a cut-in serrated trailing-edge,” *Physics of Fluids*, vol. 33, 5 2021.
- [64] L. T. L. Pereira, F. Avallone, D. Ragni, and F. Scarano, “A physics-based description and modelling of the wall-pressure fluctuations on a serrated trailing edge,” *Journal of Fluid Mechanics*, vol. 938, 5 2022.
- [65] L. T. L. Pereira, F. Avallone, D. Ragni, and F. Scarano, “A parametric study of serration design for trailing-edge broadband noise reduction,” *Applied Acoustics*, vol. 211, 8 2023.
- [66] C. K. Sumesh and T. J. S. Jothi, “Influence of nonflat plate trailing edge serration on airfoil noise reduction,” *Journal of Aerospace Engineering*, vol. 37, 3 2024.
- [67] H. Cao, M. Zhang, C. Cai, and Z. Zhang, “Flow topology and noise modeling of trailing edge serrations,” *Applied Acoustics*, vol. 168, 11 2020.
- [68] M. B. Gelot and J. W. Kim, “Effect of serrated trailing edges on aerofoil tonal noise,” *Journal of Fluid Mechanics*, vol. 904, 2020.
- [69] Y. S. Hu, Z. H. Wan, C. C. Ye, D. J. Sun, and X. Y. Lu, “Noise reduction mechanisms for insert-type serrations of the naca-0012 airfoil,” *Journal of Fluid Mechanics*, vol. 941, 6 2022.
- [70] L. Wang and X. Liu, “Aeroacoustic investigation of asymmetric oblique trailing-edge serrations enlightened by owl wings,” *Physics of Fluids*, vol. 34, 1 2022.

- [71] B. Song, L. Xu, K. Zhang, and J. Cai, “Numerical study of trailing-edge noise reduction mechanism of wind turbine with a novel trailing-edge serration,” *Physica Scripta*, vol. 98, 6 2023.
- [72] C. Lai, Y. Zhu, and M. Tsubokura, “Numerical study on noise reduction of ground-effect wing with serrated trailing edge,” *Aerospace Science and Technology*, vol. 154, 11 2024.
- [73] Y. S. Hu, Z. H. Wan, D. J. Sun, and X. Y. Lu, “Composite control of airfoil broadband noise based on the combination of porous material and serrated trailing edges,” *Physics of Fluids*, vol. 36, 2 2024.
- [74] Z. Wei, S. Wang, S. Farris, N. Chennuri, N. Wang, S. Shinsato, K. Demir, M. Horii, and G. X. Gu, “Towards silent and efficient flight by combining bioinspired owl feather serrations with cicada wing geometry,” *Nature Communications*, vol. 15, 12 2024.
- [75] M. Buszyk, P. Cyril, L. G. Thomas, B. Raphaël, S. Edouard, and M. Jacky, “Turbofan aeroacoustics with a serrated stator: Design, predictions, and comparisons with measurements,” *AIAA Journal*, pp. 1–17, 6 2025.
- [76] W. Kim, M. Ryu, J. Kim, S. Ho, L. Cho, and J. Cho, “Aeroacoustics analysis and noise reduction of dual type combined fan using lattice-boltzmann method,” *Journal of the Korean Society for Aeronautical & Space Sciences*, vol. 44, pp. 381–390, 5 2016.
- [77] W. van der Velden, D. Casalino, and G. Romani, “Full-scale serrated wind turbine trailing edge noise certification analysis based on the lattice-boltzmann method,” *AIAA SciTech Forum and Exposition*, 2023.
- [78] M. Buszyk, C. Polacsek, T. L. Garrec, R. Barrier, V. Clair, E. Salze, and C. Bailly, “Aeroacoustic assessment of a rectilinear cascade with leading edge serrations: predictions and measurements,” *Computers and Fluids*, vol. 271, 3 2024.
- [79] A. Halimi, B. G. Marinus, and S. Larbi, “Analytical prediction of broadband noise from mini-rpa propellers with serrated edges,” *International Journal of Aeroacoustics*, vol. 18, pp. 517–535, 7 2019.
- [80] M. Sanjosé, S. Moreau, B. Lyu, and L. Ayton, “Analytical, numerical and experimental investigation of trailing-edge noise reduction on a controlled diffusion airfoil with serrations,” *25th AIAA/CEAS Aeroacoustics Conference, 2019*, 2019.

- [81] A. Rak, L. Grbčić, A. Sikirica, and L. Kranjčević, “Experimental and lbm analysis of medium-reynolds number fluid flow around naca0012 airfoil,” *International Journal of Numerical Methods for Heat and Fluid Flow*, vol. 33, pp. 1955–1980, 4 2023.
- [82] J. Anderson, *Fundamentals of Aerodynamics*. McGraw-Hill, 2017.
- [83] B. Chanetz, J. Détery, P. Gilliéron, P. Gnemmi, E. R. Gowree, and P. Perrier, *Experimental Aerodynamics*. Springer International Publishing, 2020.
- [84] J. B. Barlow, W. H. Rae, and A. Pope, *Low-speed Wind Tunnel Design*. Wiley & Sons Ltd., 1999.
- [85] S. Discetti and A. Ianiro, *Experimental Aerodynamics*. CRC Press, 1st ed., 2017.
- [86] C. Coreixas, G. Wissocq, B. Chopard, and J. Latt, “Impact of collision models on the physical properties and the stability of lattice Boltzmann methods: Impact of collision models,” *Philosophical Transactions of the Royal Society A: Mathematical, Physical and Engineering Sciences*, vol. 378, jul 2020.
- [87] K. Kutscher, M. Geier, and M. Krafczyk, “Multiscale simulation of turbulent flow interacting with porous media based on a massively parallel implementation of the cumulant lattice Boltzmann method,” *Computers & Fluids*, vol. 193, p. 103733, oct 2019.
- [88] M. Geier, A. Pasquali, and M. Schönherr, “Parametrization of the cumulant lattice Boltzmann method for fourth order accurate diffusion part II: Application to flow around a sphere at drag crisis,” *Journal of Computational Physics*, vol. 348, pp. 889–898, nov 2017.
- [89] A. Pasquali, M. Geier, and M. Krafczyk, “Near-wall treatment for the simulation of turbulent flow by the cumulant lattice Boltzmann method,” *Computers and Mathematics with Applications*, vol. 79, pp. 195–212, jan 2020.
- [90] P. L. Bhatnagar, E. P. Gross, and M. Krook, “A model for collision processes in gases. I. Small amplitude processes in charged and neutral one-component systems,” *Physical Review*, vol. 94, no. 3, pp. 511–525, 1954.
- [91] O. Filippova and D. Hänel, “Grid Refinement for Lattice-BGK Models,” *Journal of Computational Physics*, vol. 147, pp. 219–228, nov 1998.

- [92] A. Tamura, K. Okuyama, S. Takahashi, and M. Ohtsuka, “Three-dimensional discrete-velocity BGK model for the incompressible Navier-Stokes equations,” *Computers and Fluids*, vol. 40, pp. 149–155, jan 2011.
- [93] S. S. Mendu and P. K. Das, “Flow of power-law fluids in a cavity driven by the motion of two facing lids - A simulation by lattice Boltzmann method,” *Journal of Non-Newtonian Fluid Mechanics*, vol. 175-176, pp. 10–24, may 2012.
- [94] P. Nathen, D. Gaudlitz, M. J. Krause, and N. A. Adams, “On the stability and accuracy of the BGK, MRT and RLB Boltzmann schemes for the simulation of turbulent flows,” *Communications in Computational Physics*, vol. 23, no. 3, pp. 846–876, 2018.
- [95] J. Jacob, O. Malaspinas, and P. Sagaut, “A new hybrid recursive regularised bhatnagar–gross–krook collision model for lattice boltzmann method-based large eddy simulation,” *Journal of Turbulence*, vol. 19, no. 11, pp. 1051–1076, 2019.
- [96] S. Hejri, D. Kamali, and E. H. Malekshah, “An experimental/numerical hydrothermal-second law analysis of a finned/tubular heat exchanger using bhatnagar–gross–krook lattice boltzmann (bgklbm) and rheological-thermal behavior of fe<sub>2</sub>o<sub>3</sub>-water,” *International Journal of Numerical Methods for Heat and Fluid Flow*, vol. 31, pp. 2308–2329, 2020.
- [97] P. Sagaut, *Large Eddy Simulation for Incompressible Flows*. Springer, Berlin, Heidelberg, 3 ed., 2006.
- [98] R. D. Moser, S. W. Haering, and G. R. Yalla, “Statistical Properties of Subgrid-Scale Turbulence Models,” *Annual Review of Fluid Mechanics*, vol. 53, pp. 255–286, jan 2021.
- [99] S. T. Bose and G. I. Park, “Wall-Modeled Large-Eddy Simulation for Complex Turbulent Flows,” *Annual Review of Fluid Mechanics*, vol. 50, pp. 535–561, jan 2018.
- [100] H. Asmuth, C. F. Janßen, H. Olivares-Espinosa, and S. Ivanell, “Wall-modeled lattice Boltzmann large-eddy simulation of neutral atmospheric boundary layers,” *Physics of Fluids*, vol. 33, oct 2021.
- [101] Y. H. Dong, P. Sagaut, and S. Marie, “Inertial consistent subgrid model for large-eddy simulation based on the lattice Boltzmann method,” *Physics of Fluids*, vol. 20, no. 3, 2008.



- [102] H. Sajjadi, M. Salmanzadeh, G. Ahmadi, and S. Jafari, “Turbulent indoor airflow simulation using hybrid LES/RANS model utilizing Lattice Boltzmann method,” *Computers and Fluids*, vol. 150, pp. 66–73, jun 2017.
- [103] M. Haussmann, A. C. Barreto, G. L. Kouyi, N. Rivière, H. Nirschl, and M. J. Krause, “Large-eddy simulation coupled with wall models for turbulent channel flows at high Reynolds numbers with a lattice Boltzmann method — Application to Coriolis mass flowmeter,” *Computers and Mathematics with Applications*, vol. 78, pp. 3285–3302, nov 2019.
- [104] Z. L. Chen, S. Hickel, A. Devesa, J. Berland, and N. A. Adams, “Wall modeling for implicit large-eddy simulation and immersed-interface methods,” *Theoretical and Computational Fluid Dynamics*, vol. 28, pp. 1–21, feb 2014.
- [105] M. Bouzidi, M. Firdaouss, and P. Lallemand, “Momentum transfer of a Boltzmann-lattice fluid with boundaries,” *Physics of Fluids*, vol. 13, no. 11, pp. 3452–3459, 2001.
- [106] P. Over and J. Christian, *Learn Aerodynamic Analysis of Automobiles with Altair ultra-FluidX*. Michigan, USA: Altair Engineering, Inc., 2021.
- [107] Airfoil Tools, “NACA 4 digit airfoil generator.” Accessed: 2022-05-02.
- [108] T.-H. Shih, L. A. Povinelli, and N.-S. Liu, “Application of generalized wall function for complex turbulent flows,” *Journal of Turbulence*, vol. 4, p. 15, 2003.
- [109] H. W. Coleman and W. G. Steele, *Experimentation, Validation, and Uncertainty Analysis for Engineers: Third Edition*. John Wiley and Sons, 7 2009.
- [110] J. Katz and A. Plotkin, “Low-speed aerodynamics,” *Low-Speed Aerodynamics*, 2 2001.
- [111] M. Drela, “XFOIL: An Analysis and Design System for Low Reynolds Number Airfoils,” in *Low Reynolds Number Aerodynamics* (T. J. Mueller, ed.), (Berlin, Heidelberg), pp. 1–12, Springer Berlin Heidelberg, 1989.
- [112] I. P. Castro, J. W. Kim, A. Stroh, H. C. Lim, and I. P. Castro, “Channel flow with large longitudinal ribs,” *J. Fluid Mech*, vol. 915, p. 92, 2021.
- [113] Y. W. Ho and J. W. Kim, “A wall-resolved large-eddy simulation of deep cavity flow in acoustic resonance,” *J. Fluid Mech*, vol. 917, p. 17, 2021.

- [114] J. M. Turner and J. W. Kim, “Quadrupole noise generated from a low-speed aerofoil in near-and full-stall conditions,” *J. Fluid Mech*, vol. 936, p. 34, 2022.
- [115] S. Palleja-Cabre, P. Chaitanya, P. Joseph, J. W. Kim, M. J. Priddin, L. J. Ayton, T. F. Geyer, and T. P. Chong, “Downstream porosity for the reduction of turbulence–aerofoil interaction noise,” *Journal of Sound and Vibration*, vol. 541, 12 2022.
- [116] I. P. Castro and J. W. Kim, “Secondary motions in turbulent ribbed channel flows,” *Journal of Fluid Mechanics*, vol. 988, p. A2, 5 2024.
- [117] L. J. Tope, J. W. Kim, and P. Spence, “Direct numerical simulations of long-range infrasound propagation: Implications for source spectra estimation,” *The Journal of the Acoustical Society of America*, vol. 155, pp. 465–478, 1 2024.
- [118] J. W. Kim, A. S. Lau, and N. D. Sandham, “Caa boundary conditions for airfoil noise due to high-frequency gusts,” *Procedia Engineering*, vol. 6, pp. 244–253, 1 2010.
- [119] J. Turner, J. W. Kim, P. Chaitanya, and P. Joseph, “Towards understanding aerofoils with dual-frequency wavy leading edges interacting with vortical disturbances,” *22nd AIAA/CEAS Aeroacoustics Conference*, 2016.
- [120] D. J. Garmann, M. R. Visbal, and P. D. Orkwis, “Comparative study of implicit and subgrid-scale model large-eddy simulation techniques for low-reynolds number airfoil applications,” *International Journal for Numerical Methods in Fluids*, vol. 71, pp. 1546–1565, 4 2013.
- [121] J. W. Kim, “Optimised boundary compact finite difference schemes for computational aeroacoustics,” *Journal of Computational Physics*, vol. 225, pp. 995–1019, 7 2007.
- [122] J. W. Kim, “High-order compact filters with variable cut-off wavenumber and stable boundary treatment,” *Computers & Fluids*, vol. 39, pp. 1168–1182, 8 2010.
- [123] J. W. Kim and D. J. Lee, “Generalized characteristic boundary conditions for computational aeroacoustics,” *AIAA journal*, vol. 38, pp. 2040–2049, 2000.
- [124] J. W. Kim and D. J. Lee, “Generalized characteristic boundary conditions for computational aeroacoustics, part 2,” *AIAA Journal*, vol. 42, pp. 47–55, 2004.

- [125] J. W. Kim, “Quasi-disjoint pentadiagonal matrix systems for the parallelization of compact finite-difference schemes and filters,” *Journal of Computational Physics*, vol. 241, pp. 168–194, 5 2013.
- [126] U. Piomelli and E. Balaras, “Wall-layer models for large-eddy simulations,” *Annual Review of Fluid Mechanics*, vol. 34, pp. 349–374, 1 2002.
- [127] N. J. Georgiadis, D. P. Rizzetta, and C. Fureby, “Large-eddy simulation: Current capabilities, recommended practices, and future research,” *AIAA Journal*, vol. 48, pp. 1772–1784, 8 2010.
- [128] G. Ramanujam and H. Özdemir, “Improving airfoil lift prediction,” *35th Wind Energy Symposium*, 2017.
- [129] J. Y. Zhu, T. S. Liu, L. Q. Liu, S. F. Zou, and J. Z. Wu, “Causal mechanisms in airfoil-circulation formation,” *Physics of Fluids*, vol. 27, 12 2015.
- [130] T. Liu, “Evolutionary understanding of airfoil lift,” *Advances in Aerodynamics*, vol. 3, pp. 1–24, 12 2021.
- [131] J. Katz, *Automotive Aerodynamics*. Automotive Series, Wiley, 2016.
- [132] T. F. Brooks, D. Stuart, and M. A. Marcolini, “Airfoil self-noise and prediction: Technical report nasa-rp-1218,” *National Aeronautics and Space Administration (NASA)*, 1989.
- [133] H. M. Lee, Z. Lu, K. M. Lim, J. Xie, and H. P. Lee, “Quieter propeller with serrated trailing edge,” *Applied Acoustics*, vol. 146, pp. 227–236, 3 2019.
- [134] Y. Yang, Y. Wang, Y. Liu, H. Hu, and Z. Li, “Noise reduction and aerodynamics of isolated multi-copter rotors with serrated trailing edges during forward flight,” *Journal of Sound and Vibration*, vol. 489, p. 115688, 12 2020.
- [135] T. J. Mueller and A. Pelletier, “Low reynolds number aerodynamics of fixed wings,” *Encyclopedia of Aerospace Engineering*, 12 2010.
- [136] M. Gad-el Hak, *Flow Control: Passive, Active, and Reactive Flow Management*. Cambridge University Press, 2000.

- [137] W. K. Blake, “Mechanics of flow-induced sound and vibration: Complex flow-structure interactions,” *Mechanics of Flow-Induced Sound and Vibration: Complex Flow-Structure Interactions*, vol. 2, pp. 1–670, 8 2017.
- [138] V. Bhargava and R. Samala, “Acoustic emissions from wind turbine blades,” *Journal of Aerospace Technology and Management*, vol. 11, 2019.
- [139] V. Bhargava and R. Samala, “Effect of boundary layer and rotor speed on broadband noise from wind turbines,” *Journal of Aerospace Technology and Management*, vol. 11, 2019.
- [140] G. Farin, *Curves and Surfaces for Computer Aided Design, A Practical Guide*. Morgan Kaufmann, 2002.
- [141] Altair Engineering Inc., *Altair AcuSolve User Guide*. Altair Engineering, Troy, MI, 2025. Available to licensed users only.
- [142] Altair Engineering Inc., *Altair AcuSolve User Guide*. Altair Engineering, Troy, MI, 2021. Available to licensed users only.
- [143] Altair Engineering Inc., *Altair AcuSolve User Guide*. Altair Engineering, Troy, MI, 2023. Available to licensed users only.
- [144] T. A. Smith and Y. Ventikos, “Wing-tip vortex dynamics at moderate reynolds numbers,” *Physics of Fluids*, vol. 33, p. 35111, 3 2021.

# LIST OF FIGURES

1.1	Classification of CFD methods across different scales, highlighting the mesoscopic position of the Lattice Boltzmann Method and the role of high-performance computing in enabling higher-fidelity turbulence modeling approaches. . . . .	2
1.2	3D model representation of the owl wing serrations. . . . .	7
1.3	Visualized and simplified main scientific contributions that also correlate with the dissertation structure. . . . .	12
2.1	Subsonic open-circuit wind tunnel with four main flow path components highlighted in orange, while sensors, control panel, software, and airfoil are displayed in blue. . . . .	18
2.2	Scale hierarchy in CFD: microscale molecular dynamics (left) captures individual particle motion, mesoscale LBM (center) tracks particle distribution functions on a regular lattice, and macroscale continuum methods (right) solve macroscopic field variables. . . . .	21
2.3	Three-dimensional D3Q27 velocity set comprising one zero velocity at the center (rest particles) and 26 non-zero discrete velocities. The velocity vectors connect the central lattice node to its nearest neighbors (six vectors, purple arrows), next-nearest neighbors (twelve vectors, red arrows), and diagonal neighbors (eight vectors, green arrows), providing enhanced isotropy and rotational invariance compared to lower-order velocity sets. . . . .	23
2.4	Collision-streaming algorithm in the LBM showing initial particle populations (left), post-collision redistribution (middle), and streaming to neighboring nodes (right). . . . .	24
2.5	Computational domain configuration showing nested refinement zones (orange boxes with arrows) and body offset region (purple box with arrow). . . . .	27

2.6	Computational mesh distribution around the NACA 0012 airfoil showing the hierarchical refinement strategy: (a) complete three-dimensional domain, (b) sectioned three-dimensional view, (c) two-dimensional mid-plane cross-section, and (d) detailed view of near-airfoil refinement zones. . . . .	29
2.7	Exponential voxel growth with decreasing coarsest mesh size, shown by the yellow-green trend line. Purple circles represent mesh configurations (Coarse, Medium, Fine, Finest), with marker size proportional to the coarsest mesh dimension. . . . .	31
2.8	Pressure coefficient distribution along the normalized chord length for four mesh configurations: (a) upper surface showing excellent convergence except near the leading edge, where the finest mesh captures enhanced suction peaks, and (b) lower surface demonstrating consistent behavior across mesh refinements with trailing edge variations for the coarsest mesh. . . . .	32
2.9	Velocity magnitude profiles extracted at $yz$ -plane cross-sections for $8^\circ$ angle of attack across different mesh configurations. Cross-sections $Dx_1$ through $Dx_4$ are located at $x = 0.182$ m, $0.185$ m, $0.348$ m, and $0.351$ m, respectively. Profiles represent time-averaged velocity magnitude over the final 10% of simulation duration, demonstrating mesh independence in upstream regions and convergence behavior in the complex wake region. . . . .	35
2.10	Wind tunnel measured pressure coefficient distributions at discrete tapping points over normalized chord length for four angles of attack: $2^\circ$ (yellow), $4^\circ$ (light green), $6^\circ$ (forest green), and $8^\circ$ (light sea green) for the airfoil's (a) upper surface and (b) lower surface. . . . .	37
2.11	Pressure coefficient distribution visualization for the NACA 0012 airfoil at varying angles of attack: (a) $2^\circ$ , (b) $4^\circ$ , (c) $6^\circ$ , and (d) $8^\circ$ . High-pressure regions (red shading) indicate positive $C_p$ values, while low-pressure regions (blue shading) represent negative $C_p$ values. Purple circles denote tapping positions, with red and blue stars marking maximum and minimum $C_p$ locations, respectively. . .	38

2.12	Experimental pressure coefficient distributions with measurement uncertainties (error bars) for lower surface (red) and upper surface (teal) at four angles of attack: (a) 2°, (b) 4°, (c) 6°, and (d) 8°. The error bars represent one standard deviation from the mean, providing confidence intervals for the experimental measurements. . . . .	40
2.13	Time-averaged pressure (a-d) and velocity magnitude (e-h) contours at the mid-plane XY cross-section for angles of attack: (a,e) 2°, (b,f) 4°, (c,g) 6°, and (d,h) 8°. Averaging is performed over the final 10% of simulation time. The red dashed line is a demarcation of the boundary layer growth region. . . . .	42
2.14	Stagnation point distribution for different angle of attack cases, with the magnified leading edge region highlighted by the purple rectangle. The lower surface is depicted in black, while the upper surface is shown in gray. Stagnation points circle markers are color-coded for different AoA: 2° (yellow), 4° (light green), 6° (forest green), and 8° (light sea green). . . . .	43
2.15	Pressure coefficient distributions comparing LBM results (red rectangles for lower surface, teal circles for upper surface) with experimental data (violet markers and dashed lines) around the NACA 0012 midplane surface. Semi-transparent violet bands around the dashed lines represent experimental measurement uncertainties. . . . .	44
2.16	Comparison between experimental results (violet markers) and LBM predictions (red rectangles for lower surface, teal circles for upper surface). Semi-transparent red and teal regions represent the magnitude of differences between computational and experimental data. . . . .	46
3.1	Acceleration phase at the start of the simulation, comparing Gaussian and linear velocity profiles, followed by a constant phase for $t^* > 8$ . . . . .	51
3.2	Block distribution for the airfoil multi-block grid system: (a) 2D XY-plane view showing the number of CPUs assigned to each block, and (b) 3D view of the same multi-block structure with block nomenclature. . . . .	52
3.3	(a) Geometry of the primary airfoil with added serrations (marked red) that shows serration length and wavelength. (b) Mesh distribution on the 2D zoomed-in part of the domain around the airfoil's surface. . . . .	53

3.4	Wall-unit grid spacing for the G2 PTE airfoil where $s^+$ , $n^+$ , and $z^+$ represent streamwise (blue), normal (orange), and spanwise (green) spacing, respectively. Hatched parts represent the proposed LES and DNS range, while the red dash-dotted line represents the LES border. . . . .	54
3.5	Grid validation for the PTE airfoil. The first two graphs compare the non-dimensional forces in the $x$ - and $y$ -directions. The remaining four graphs provide a detailed view of the pressure and skin friction components of the forces for the three different meshes: coarse (blue), medium (orange), and fine (green). . . . .	55
3.6	Comparison of the primary trailing edge airfoil for: (a) the last time unit $t^* = 20$ , and (b) for the time-averaged values from 15 to 20 time units. . . . .	56
3.7	Temporal evolution of non-dimensional force components for the PTE airfoil at $Re = 250,000$ : (a) $x$ -direction forces showing pressure component (violet) and skin friction component (yellow); (b) $y$ -direction forces showing pressure component (blue) and skin friction component (green). . . . .	59
3.8	Starting vortex formation and circulation balance: (a) computational vorticity contour showing the starting vortex development (yellow regions indicate higher vorticity magnitude); (b) schematic illustration of the circulation balance between bound vortex ( $\Gamma_B$ ) and starting vortex ( $\Gamma_S$ ) according to Kelvin's circulation theorem. . . . .	60
3.9	Pressure field evolution and stagnation point migration: (left) pressure fluctuation contours at $t^* = 2.4$ (top) and $t^* = 9.6$ (bottom), with low-pressure regions highlighted by red ellipses; (right) corresponding pressure coefficient distributions showing the downstream migration of maximum $C_p$ location (stagnation point). The green circles emphasize the stagnation point displacement between the two time instances. . . . .	61



3.10	Temporal evolution of pressure coefficient distribution on the airfoil mid-plane surface showing boundary layer instability development: (a) initial oscillation detection at $t^* = 10.8$ , (b) amplitude growth and downstream propagation at $t^* = 11.8$ , and (c) fully developed oscillatory behavior at $t^* = 17.5$ . Teal circles and red rectangles represent upper and lower surface $C_p$ values, respectively. Red and green diamonds indicate the instantaneous minimum and maximum $C_p$ values, respectively, while dotted lines represent the global extrema throughout the simulation. . . . .	63
3.11	Boundary layer transition visualization using $Q$ -criterion iso-surfaces ( $Q = 0.01$ ) colored by streamwise velocity magnitude: (a) initial instability detection at $t^* = 10.2$ , (b) downstream propagation and amplification at $t^* = 13.2$ , (c) characteristic roll-up formation at $t^* = 16.7$ , and (d) wake turbulence development at $t^* = 19.0$ . The spanwise dimension is exaggerated for visualization clarity. . . . .	64
3.12	Mid-plane streamline evolution showing boundary layer transition progression: (a) attached laminar boundary layer at $t^* = 10.0$ , (b) initial boundary layer disturbances at $t^* = 11.3$ , and (c) fully developed laminar separation bubble with recirculation zone (highlighted by green dotted ellipse) at $t^* = 14.0$ . . . . .	66
3.13	Representation of shear layer and boundary layer instability using $Q$ -criterion ( $Q = 0.01$ ) at different time instances: (a) $t^* = 11.5$ , (b) $t^* = 13.6$ , and (c) $t^* = 19.0$ . A mid-plane cut along the spanwise axis visualizes sound waves at the same time instances as the 3D vortices. Legends apply to all subfigures, except for the extracted circle in the upper-right corner, which represents a reduced legend range to visualize shear layer-generated sound waves. . . . .	67
3.14	Formation and breakdown of the laminar separation bubble visualized using $Q$ -criterion ( $Q = 0.01$ ), with sound wave propagation (a-d) and streamlines in a mid-plane cut (e-f) at different time instances. The transparent dashed violet line emphasizes the region of laminar separation bubble bursting. . . . .	69
3.15	Temporal comparison of non-dimensional $x$ -direction forces between PTE and STE airfoils: (a) total force magnitude, (b) pressure force component, and (c) skin friction force component. The divergence in performance becomes apparent after the acceleration phase concludes at $t^* \approx 8$ . . . . .	72

3.16	Comparative visualization of vortical structures and acoustic wave propagation for primary trailing edge (a,c) and serrated trailing edge (b,d) airfoils, demonstrating laminar separation bubble suppression through serration implementation. $Q$ -criterion iso-surfaces ( $Q = 0.01$ ) are colored by streamwise velocity magnitude, while acoustic waves are visualized through divergence of density and velocity vector contours in the mid-plane. . . . .	73
3.17	Temporal comparison of non-dimensional $y$ -direction forces between PTE and STE airfoils: (a) total force magnitude, (b) pressure force component, and (c) skin friction force component. . . . .	75
3.18	Detailed analysis of post-acceleration aerodynamic behavior: (a) temporal evolution of non-dimensional $y$ -direction force during constant velocity operation, highlighting stability differences between configurations; (b,c) comparative visualization of trailing edge noise onset through acoustic wave contour plots, demonstrating earlier noise generation in the STE configuration at $t^* = 11.5$ versus $t^* = 13.4$ for the PTE airfoil. . . . .	76
3.19	Pressure coefficient comparison between PTE (red dots) and STE (teal dots) configurations: (a) time-averaged $C_p$ distribution over the interval $t^* = 14$ to $t^* = 16$ , demonstrating the absence of characteristic laminar separation bubble features in the STE case; (b,c) instantaneous pressure distributions at $t^* = 14$ and $t^* = 16$ , respectively, highlighting the reduced oscillatory behavior in the STE configuration. . . . .	77
3.20	PTE airfoil trailing edge sound wave occurrence visualization for various Reynolds numbers: (a) $f_y^*$ versus $t^*$ graph with emphasized oscillations and trailing edge noise onset phases highlighted by transparent circles colored with blue palette; (b-e) sound wave contour plots and iso-surfaces at emphasized time steps, where each subfigure corresponds to the circle colors for respective Reynolds number cases. . . . .	79
3.21	Comparison of non-dimensional $y$ -direction forces for PTE (red) and STE (teal) airfoils across four Reynolds numbers: (a) $Re = 100,000$ , (b) $Re = 250,000$ , (c) $Re = 400,000$ , and (d) $Re = 500,000$ . Red (PTE) and teal (STE) circles highlight the onset of trailing edge sound wave propagation. . . . .	81

3.22	Comparison of non-dimensional $x$ -direction forces for PTE (red) and STE (teal) airfoils with corresponding flow visualizations. Teal arrows highlight the turbulent boundary layer initiation phase for the STE airfoil. Four Reynolds number cases are presented: (a) $Re = 100,000$ , (b) $Re = 250,000$ , (c) $Re = 400,000$ , and (d) $Re = 500,000$ . The left legends apply to force plots, while the right legends correspond to flow visualization contours. . . . .	82
3.23	Measurement point locations around the Joukowski airfoil (green circles) with fluid flow direction indicated by the brown arrow. The red circle highlights the measurement point at $150^\circ$ that receives detailed analysis in subsequent figures.	85
3.24	Non-dimensional pressure fluctuations for the measurement point at the $150^\circ$ angle from the trailing edge for Reynolds numbers: (a) 100,000, (b) 250,000, (c) 400,000, and (d) 500,000. PTE curves are shown in red, while STE curves are shown in teal. Upper panels represent the complete simulation duration, while the gray rectangles indicate the zoomed regions displayed in the lower panels. The transparent purple region highlights the time period analyzed in subsequent figures. . . . .	86
3.25	Polar plot visualization of PTE and STE sound pressure levels around the trailing edge for Reynolds numbers: (a) 100,000 and (b) 250,000. PTE data are shown with circles using the viridis colormap, while STE data use diamond markers with the plasma colormap. . . . .	89
3.26	Polar plot visualization of PTE and STE sound pressure levels around the trailing edge for Reynolds numbers: (a) 400,000 and (b) 500,000. PTE data are shown with circles using the viridis colormap, while STE data use diamond markers with the plasma colormap. . . . .	90
4.1	PTE wing surface discretization showing three-dimensional geometry with detailed mesh point distribution. The main figure displays the full wing planform, while the magnified insets highlight: (upper left) the leading edge region with enhanced point clustering for accurate curvature representation, and (lower right) the trailing edge region demonstrating the finite-thickness implementation with blunt trailing edge geometry. . . . .	95

4.2	STE wing configurations: (a) triangular serrations with sharp vertices, and (b) sinusoidal serrations with smooth curvature transitions. Both maintain identical wavelength ( $0.05L_C$ ) and amplitude ( $0.1L_C$ ) parameters. . . . .	96
4.3	Pressure coefficient distributions comparing LBM-UFx 2025 results averaged over the last 10% (green rectangles with filled areas representing lift) with experimental data (violet markers and dashed lines with filled regions representing measurement uncertainties) and LBM-UFx 2021 data (red and teal markers). .	100
4.4	Pressure coefficient distributions for different spanwise sections compared with experimental data (violet markers). The previously analyzed section is shown in green at $z = 0$ m, while sections at $z = 0.05$ m and $z = 0.125$ m are displayed in red and dark orange, respectively. . . . .	101
4.5	Pressure coefficient distributions comparing LBM-UFx 2025 results for the final time step (yellow rectangles with filled areas representing lift) with experimental data (violet markers and dashed lines with filled regions representing measurement uncertainties) and LBM-UFx 2021 data (red and teal markers). .	102
4.6	Temporal lift coefficient comparison for PTE (red line) and STE (teal dashed line) wings at $8^\circ$ angle of attack with inset showing the final 40% of simulation duration emphasizing oscillations in the converged stage. . . . .	103
4.7	Temporal drag coefficient comparison for PTE (red line) and STE (teal dashed line) wings at $8^\circ$ angle of attack with inset showing the final 40% of simulation duration emphasizing oscillations in the converged stage. . . . .	104
4.8	Lift and drag coefficient comparison between PTE (red line) and STE (teal dashed line) during the final portion of the acceleration phase. . . . .	105
4.9	Representation of boundary layer transition, shear layer instability, wake region, and wing tip vortex development visualization using $Q$ -criterion ( $Q = 1000$ ) colored by streamwise velocity at different time steps: (a) 0.0396 s, (b) 0.0622 s, (c) 0.0706 s, and (d) 0.0763 s. Mid-plane cuts show pressure contours, with left subfigures representing PTE wings and right subfigures representing STE wings. . . . .	106
4.10	Physical phenomena representation using vorticity contour plots at different time steps: (a) 0.0396 s, (b) 0.0622 s, (c) 0.0706 s, and (d) 0.0763 s. Left subfigures represent PTE wings, while right subfigures represent STE wings. .	108

4.11 Comparison of triangular (teal dashed line) and sinusoidal (gold dashed line)	
STE wing models during acceleration phase for temporal: (a) lift coefficient	
and (b) drag coefficient analysis. . . . .	109

# LIST OF TABLES

2.1	Pressure tapping positions for surface pressure measurement on the NACA 0012 airfoil. . . . .	19
2.2	Refinement zone specifications including mesh sizes, spatial dimensions, and positioning coordinates, along with body offset parameters for near-wall resolution. . . . .	27
2.3	Mesh configuration summary showing total fluid voxels and pressure coefficient extrema for mesh assessment. . . . .	33
2.4	RMSE analysis of pressure coefficient distributions between different meshes for both airfoil surfaces. . . . .	33
2.5	Maximum pressure coefficient standard deviations for upper and lower surfaces with corresponding tapping position numbers for each angle of attack configuration. . . . .	39
2.6	Statistical validation metrics including Root Mean Square Error (RMSE) and coefficient of determination ( $R^2$ ) for different angles of attack, with separate RMSE values for upper and lower surfaces. . . . .	46
3.1	Grid distribution for PTE airfoil simulation validation employs three different mesh configurations. . . . .	53
3.2	Relative difference in mean non-dimensional forces in the $x$ - and $y$ -directions between the PTE and STE airfoils for four Reynolds numbers. . . . .	83
3.3	Statistical analysis of PTE and STE SPL data showing minimum, maximum, and mean values across different Reynolds numbers. . . . .	91
3.4	Comprehensive comparison of SPL reduction between PTE and STE airfoils, with separate analysis for upper and lower surfaces across various Reynolds numbers. Values represent noise reduction achieved by the STE configuration. .	91
4.1	Comparison of lift ( $C_L$ ) and drag coefficient ( $C_D$ ) for PTE and STE configurations across various angles of attack. . . . .	105

# LIST OF ABBREVIATIONS

<b>AoA</b>	Angle of Attack
<b>BGK</b>	Bhatnagar–Gross–Krook
<b>CFD</b>	Computational Fluid Dynamics
<b>CFL</b>	Courant-Friedrichs-Lewy
<b>CPU</b>	Central Processing Unit
<b>DMD</b>	Dynamic Mode Decomposition
<b>DNS</b>	Direct Numerical Simulation
<b>EDR</b>	Enhanced Data Rate
<b>FDM</b>	Finite Difference Method
<b>FEM</b>	Finite Element Method
<b>FVM</b>	Finite Volume Method
<b>GLW</b>	Generalized Law of the Wall
<b>GPGPU</b>	General Purpose Graphics Processing Unit
<b>GPU</b>	Graphics Processing Unit
<b>GWF</b>	Generalized Wall Function
<b>HCA</b>	Host Channel Adapter
<b>HDD</b>	Hard Disk Drive
<b>HPC</b>	High Performance Computing
<b>IB</b>	InfiniBand
<b>IB-LBM</b>	Immersed Boundary Lattice Boltzmann Method
<b>IOPS</b>	Input/Output Operations Per Second
<b>ISP</b>	Insert-type Porous-Serrated
<b>LBM</b>	Lattice Boltzmann Method
<b>LES</b>	Large Eddy Simulation
<b>LSB</b>	Laminar Separation Bubble
<b>MFS-Iron</b>	Multi-Flapped-Serration with Iron-Shaped Edges
<b>MPI</b>	Message Passing Interface

<b>MRT</b>	Multiple Relaxation Time
<b>PIV</b>	Particle Image Velocimetry
<b>POD</b>	Proper Orthogonal Decomposition
<b>PTE</b>	Primary Trailing Edge
<b>RANS</b>	Reynolds-Averaged Navier–Stokes
<b>RDIMM</b>	Registered Dual Inline Memory Module
<b>RMS</b>	Root Mean Square
<b>RMSE</b>	Root Mean Square Error
<b>SAS</b>	Serial Attached SCSI
<b>SATA</b>	Serial Advanced Technology Attachment
<b>SCSI</b>	Small Computer System Interface
<b>SPH</b>	Smoothed Particle Hydrodynamics
<b>SPL</b>	Sound Pressure Level
<b>SSD</b>	Solid State Drive
<b>STE</b>	Serrated Trailing Edge
<b>TE</b>	Trailing Edge
<b>UAV</b>	Unmanned Aerial Vehicle
<b>UFX</b>	UltraFluidX
<b>VDAS</b>	Versatile Data Acquisition System
<b>VPI</b>	Virtual Protocol Interconnect
<b>WMLES</b>	Wall Modeled Large Eddy Simulation



# CURRICULUM VITAE

Andro Rak was born on November 1, 1996, in Rijeka, Croatia. He completed his Master's degree in Mechanical Engineering in 2021 at the Faculty of Engineering, University of Rijeka, where he was employed as an assistant in the same year. During that year, he also enrolled in doctoral studies under the supervision of Prof. Dr. Sc. Lado Kranjčević. His research interests are focused on aerodynamics and the application of computational fluid dynamics and high-performance computing in solving applicable engineering problems. During his doctoral studies, he spent six months at the University of Southampton as a member of the Aerodynamics and Flight Mechanics research group, where he worked on the analysis of bio-inspired wings. His scientific contributions include authorship of two scientific papers published in Q1 category journals, according to WoS, as well as participation in four national and four international projects. Additionally, he has given numerous public presentations aimed at science popularization. His expertise has been recognized at the international level - he is the recipient of the award for the best solved aerodynamics test at the prestigious Motorsport Industry Association competition in Silverstone (2023).

# LIST OF PUBLICATIONS

## Published scientific papers in peer-reviewed journals:

1. Rak, A., Grbčić, L., Sikirica, A., & Kranjčević, L. (2023). Experimental and LBM analysis of medium-Reynolds number fluid flow around NACA0012 airfoil. *International Journal of Numerical Methods for Heat and Fluid Flow*, 33(5), 1955–1980.  
<https://doi.org/10.1108/HFF-06-2022-0389/FULL/XML>
2. Rak, A., Mrakovčić, T., Mauša, G., & Kranjčević, L. (2025). Computational Fluid Dynamics Analysis of Ballast Water Treatment System Design. *Journal of Marine Science and Engineering* 2025, Vol. 13, Page 743, 13(4), 743.  
<https://doi.org/10.3390/JMSE13040743>

## Accepted scientific papers in peer-reviewed journals:

1. Rak, A., Kranjčević, L., & Kim, JW. (2025). Aerodynamic and aeroacoustic analysis of airfoils with a serrated trailing edge during flow acceleration. *Advances in Aerodynamics*, Vol. 7 (in press).  
<https://doi.org/10.1186/s42774-025-00220-9>